THE 2D PHASE DIAGRAM ASSOCIATED WITH A PDE MODEL FOR SELF-ASSEMBLY OF DIBLOCK COPOLYMERS

by

Mirjana Maraš

B.Sc., Simon Fraser University, 2007

A Thesis submitted in partial fulfillment
of the requirements for the degree of
Master of Science
in the Department
of
Mathematics

SIMON FRASER UNIVERSITY
Summer 2009

APPROVAL

Name: Mirjana Maraš

Degree: Master of Science

Title of Thesis: The 2D Phase Diagram Associated with a PDE Model for Self-assembly of Diblock Copolymers

Examining Committee: Dr. Ralf Wittenberg
Chair

Dr. Rustum Choksi
Senior Supervisor

Dr. JF Williams
Co-Supervisor

Dr. Paul Tupper
External Examiner

Date Approved: June 4, 2009

Declaration of
Partial Copyright Licence

Abstract

Diblock copolymers are macromolecules formed by grafting together two polymer chains of types A and B respectively. Melts of these macromolecules exhibit an amazing ability for self-assembly into A- and B-rich domains, which resemble well-studied periodic structures, such as lamellae, spheres, cylindrical tubes, and gyroids. Understanding the process by which these structures are created may ultimately enable the synthesis of materials with tailored properties.

The goal of this thesis is the computation of a two-dimensional phase diagram for self-assembly of diblock copolymers. The self-assembly process is modeled by a modified Cahn-Hilliard equation, which is derived as a gradient flow of the nonlocal Cahn-Hilliard energy. We choose a pseudospectral exponential time differencing scheme to numerically simulate solutions of the PDE. Furthermore, we apply center manifold theory to obtain specific characterizations of the phase boundaries. These results are used as guidance for a numerical extension of the phase diagram.

Keywords: diblock copolymers; phase diagram; gradient flow; modified Cahn-Hilliard; center manifold theory; exponential time differencing

Subject Terms: Polymers - Mathematical Models; Partial Differential Equations; Evolution Equations - Numerical Solutions; Asymptotic Theory

To my Sister Ivana, Mother Vojislavka, and Father Aleksandar,
my beautiful sunflower family in Montenegro.

"Don't blow it. Good planets are hard to find."

— Time Magazine cover

Acknowledgments

I thoroughly enjoyed the graduate student life over the last two years, and am happy that my curiosity continued to be nourished in the formal education setting. For this I would like to thank my two wonderful supervisors, Dr. Rustum Choksi and Dr. J.F. Williams, who were always very supportive of my efforts and enabled me to fully experience the exciting life of a researcher. I am also very grateful to the community of Applied Mathematics professors, especially Dr. Kropinski, who provided a window into what it means to be a researcher during my undergraduate career; Dr. Wittenberg and Dr. Muraki, for generously helping me with matters of both mathematics and life; and Dr. Russell for his stories. I loved sharing chocolate, math, and great conversations with fellow graduate students, and I thank you for being so much fun! It was a privilege to take part in the life of the Applied Mathematics community at SFU, and I will remember you all when I go somewhere new in pursuit of my dreams.

Contents

List of Tables

List of Figures

Chapter 1

Introduction

Block copolymers are macromolecules, which are formed by joining two or more chemically dissimilar monomer sequences. These macromolecules are used as building blocks for the creation of soft materials, which exhibit fluid-like disorder at molecular length scales, and highly ordered structures at longer nano length scales. The ability of block copolymers to self-assemble into these highly ordered nano-structures is of great technological importance as it facilitates the creation of materials with tailored mechanical, electrical, optical, and other physical properties. Their use in the industry is abundant. In Europe, block copolymers are mixed with asphalt to reduce the cracking of pavement during cold or hot weather conditions. Our everyday box tape uses viscoplastic block copolymers to achieve pressure-sensitive adhesion, while addition of copolymers to plastics used in the manufacture of microelectronic components leads to their greater toughness and desired surface properties [2]. Block copolymer research is currently almost exclusively dedicated to block copolymers synthesized from petrochemical sources (non-biodegradable plastics). However, the increased availability of inexpensive biologically engineered monomers derived from renewable resources will hopefully lead to the development of renewable block copolymers.

A diblock copolymer is the simplest and most studied block copolymer. It is a linear chain molecule consisting of two chemically distinct sub-chains, which are covalently bonded to each other. One of the sub-chains is made up of monomers of type A, and the other of monomers of type B. A system of many such molecules can form a diblock copolymer melt, solid, solution, or blend. In this thesis we only consider diblock copolymer melts, which are formed above the melting temperature of the blocks, and are characterized by random coiling of the chains at the mesoscopic level. Above a critical temperature, diblock

copolymers mix to form a homogeneous melt. However, below the critical temperature, repulsion between the unlike monomers A and B induces strong segregation of the sub-chains. Separation cannot occur on the macroscopic scale, like in the case of oil and water, as the sub-chains are chemically bonded to each other. Instead, repulsion between them drives the system to minimize the contact between the sub-chains, and thus localize the covalent bond linkage to the interface between A- and B-rich domains. This tendency is counterbalanced by the entropy cost associated with chain stretching, thus leading to phase separation on a mesoscopic scale (1-100 nm), with A- and B-rich domains emerging. The resulting mesoscopic domains are found to resemble well-studied periodic structures with triply periodic constant mean curvature surfaces as their interfaces, e.g. lamellae, spheres, cylindrical tubes, single- and double-gyroids. Lamellar and spherical phases are sketched in Figure 1.1. Different mesoscopic geometries lead to different macroscopic properties of the diblock copolymer melt, such as its elasticity, strength, etc., and this is why understanding of the self-assembly process may enable the creation of materials with tailored material properties.

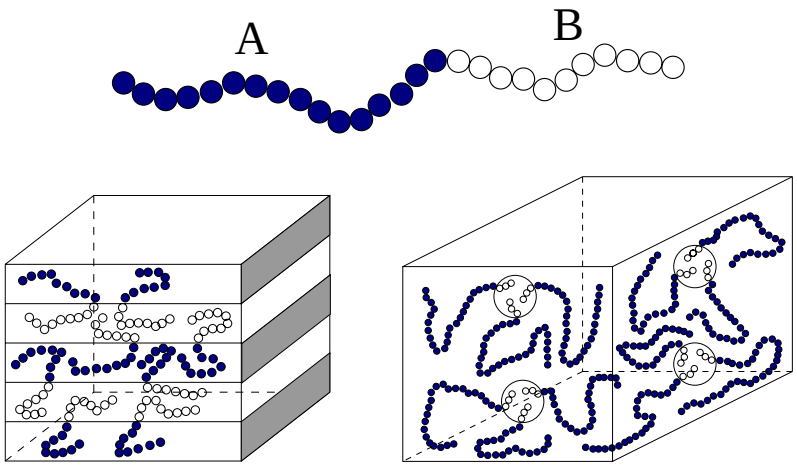

Figure 1.1: Top: a diblock copolymer macromolecule. Bottom: self-assembly of diblock copolymers into the lamellar (left) and spherical (right) phases [4].

One of the main theoretical challenges is to determine the phase diagram for the self-assembly of diblock copolymers; that is, given a set of material parameters, predict the morphology (size, shape, orientation) of the ordered structure. The vast physics literature indicates three relevant material parameters: χ, the Flory-Huggins interaction parameter, measuring the incompatibility of the two monomer species (positive values of χ indicate

net repulsion between the species, while negative values indicate free energy drive towards mixing); N, the copolymer degree of polymerization, measuring the number of monomers per macromolecule; and the molecular weight f, measuring the relative volume of the A monomer chain compared with the volume of the whole macromolecule. These three material parameters are nondimensional. One can also consider a dimensional parameter called the Kuhn statistical length l, which measures the average monomer space size. The value of this parameter is assumed to be the same for both A and B monomers everywhere in this thesis, with the exception of the following experimental phase diagram section. All diblock copolymer melts are also assumed to be incompressible.

1.1 Experimental Phase Diagram

Experimental phase diagrams have been derived for particular diblock copolymers, and one of the most cited ones is the phase diagram for polyisoprene-polystyrene (PI-PS) diblock copolymers near the order-disorder transition, presented by Khandpur et al. in [18]. Polyisoprene is a synthetic polymer designed to mimic natural rubber, and polystyrene is one of the most common kinds of plastic derived from fossil fuels. In this study, ten PI-PS diblock copolymer melts were synthesized with the polyisoprene volume fraction, f_{PI}, ranging from 0.24 to 0.82. The synthesis was achieved by anionic polymerization, as this ensured a narrow distribution of the molecular weight, f_{PI}. The process by which the polymer was grown was carried out at 40°C and consisted of repetitive additions of monomers to the 'living' anionic (very reactive) chain. The compositions of diblock copolymers were estimated from the masses of the added monomers, and the values of f_{PI} were then calculated using the known densities of polyisoprene and polystyrene.

The next step of the experiment was the preparation of diblock copolymer specimens for the study of their phase behaviour. To this end, diblock copolymers were deformed into 0.3-2 mm thick films by being placed between two Teflon-covered glass plates with the appropriate spacing. After 15 hours of heating to 120°C under a vacuum, the weight of the plates led to the deformation of copolymers into transparent films, which were then cooled to room temperature.

Dynamic mechanical experiments were used to determine the order-order and order-disorder transition temperatures. Varying-amplitude shear stress was exerted on the specimens as the temperature was increased at a rate of 1 or 2 °C/min, and the dynamic elastic

modulus, measuring the stress to strain ratio in vibratory conditions, was recorded. Gradual heating of the specimens induced changing underlying morphologies, which consequently led to different responses to shear stress. Thus, abrupt changes in the dynamic elastic modulus were used to identify phase transition temperatures. These varied between about 100°C, the melting point of crystallizable polystyrene, and 300°C, where all specimens exhibited the disordered phase. The fact that polystyrene forms glass at or below 100°C enabled the capturing of ordered phases. This was accomplished by quickly cooling the heated specimen with a formed morphology down to the glass-transition temperature, thus essentially freezing its self-assembling structure.

Once the phase transition temperatures were identified, the morphologies attained at nearby temperatures were examined via transmission electron microscopy. This kind of microscopy enabled finer detail in images than the more common optical microscopy. PI-PS diblock copolymers were cut into 50-70 nm thin slices with a diamond knife at -100°C. These were then placed on a copper grid, and the PI blocks were preferentially stained by osmium tetraoxide, so that they appeared dark when hit by a beam of electrons. Images obtained in this way were used to identify the three classical phases: lamellae, hexagonally packed cylinders, and body centered cubic spheres (BCC), as well as the non-classical phase consisting of hexagonally perforated lamellae, that is hexagonally packed PI cylinders perforating the PS lamellae, where PI is the minor component. Figure 1.2 shows representative micrographs used to identify these four phases.

However, micrographs could not be used to make accurate assessments of all underlying structures, so two techniques: small-angle X-ray scattering and small-angle neutron scattering, were further employed. They confirmed the symmetry of the BCC spheres and identified the non-classical bicontinuous cubic phase, commonly referred to as the gyroid phase.

Having identified the phase transition temperatures and the morphologies of the self-assembling structures, the phase diagram for PI-PS diblock copolymers could be determined. The material parameters, χN and f, were found to describe most phase behaviour, with N and f being easily measured experimentally. The parameter χ was estimated from the following approximate order-disorder transition (ODT) relationship

$$(\chi N)_{ODT} = 10.495 + 41.022 N^{-1/3} a^{-2} v^{2/3}, \tag{1.1.1}$$

which was theoretically predicted to hold for symmetric diblock copolymers ($f = 0.5$) by

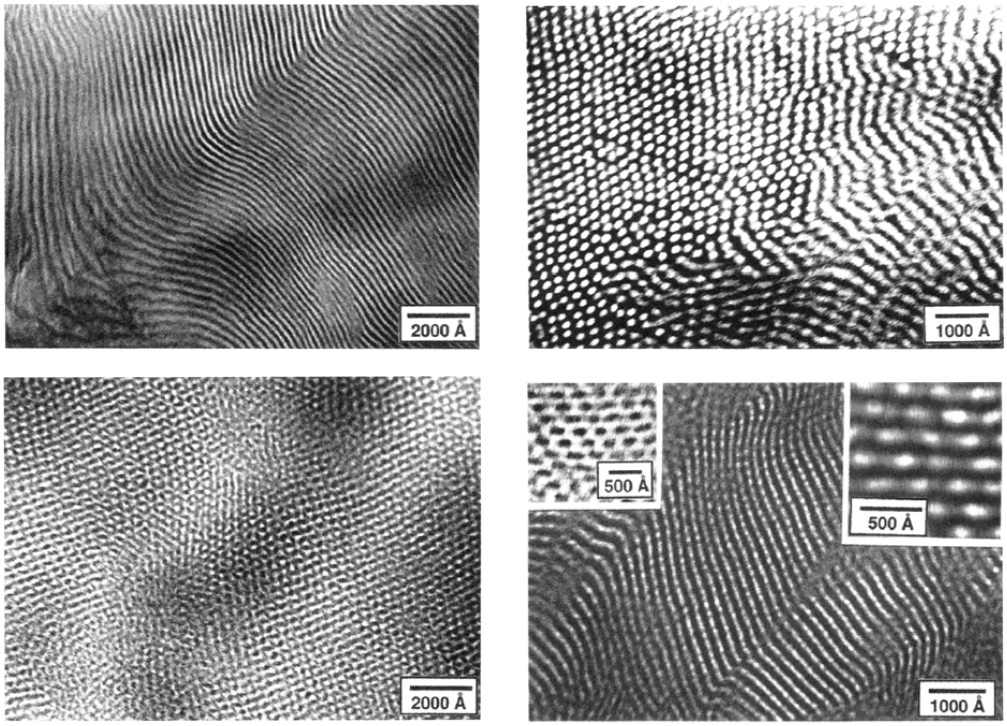

Figure 1.2: Micrographs of four PI-PS phases [18]. Top: lamellar and hexagonally packed cylinder phases. Bottom: body-centered cubic spheres, and hexagonally perforated lamellae shown from three different projections.

Fredrickson and Helfand [11]. Parameters a and v represented the length and volume of monomers in each macromolecule, respectively, and were experimentally measurable. A linear fit to the ODT temperatures of symmetric diblock copolymer melts of varying degrees of polymerization then led to

$$\chi(T) = \frac{71.4}{T} - 0.0857,$$

as an estimate for the temperature-dependent value of the Flory-Huggins parameter.

The experimental phase diagram obtained in [18] for PI-PS diblock copolymers near the order-disorder transition is presented in Figure 1.3. An important fact which is not captured by the phase diagram is that the non-classical phases were found to depend both on χ and N. In spite of this, the joint parameter χN was chosen along with f to describe the experimental phase behaviour of diblock copolymers. This choice was motivated by the self-consistent mean field theory (described in the following section), which identifies these two bifurcation parameters as the only significant ones. The key mean field approximation

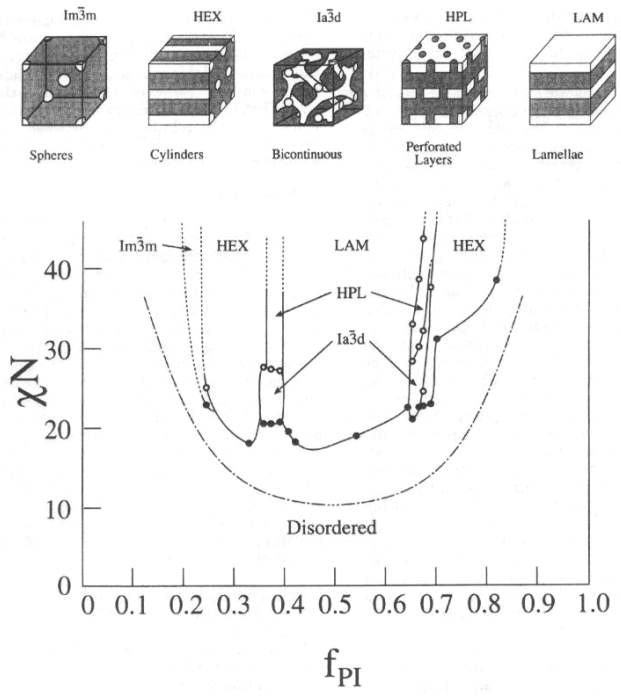

Figure 1.3: The experimental phase diagram for the self-assembly of polyisoprene-polystyrene diblock copolymers [18].

is exact in the limit $N \to \infty$, and thus away from the order-disorder transition. In this limit, equation (1.1.1) simplifies to $(\chi N)_{ODT} = 10.495$, a result predicted by Leibler in [19].

1.2 Self-Consistent Mean Field Theory

Exhaustive experimental studies of the phase behaviour of diblock copolymers are limited by the large parameter space and the cost and difficulty of conducting combinatorial materials discovery. The process of material design may thus be accelerated through the employment of mathematical models, which capture some of the essential underlying physical principles. Direct application of particle theory (molecular dynamics) to the modeling of diblock copolymer melts is not a viable option, as it requires a highly computationally costly consideration of the position and momentum of each monomer in the system. Instead, the physics community chooses the self-consistent mean field theory (SCFT) as the state of the art approach for modeling the equilibrium state of diblock copolymers [21, 2, 12].

The SCFT theory presents an extension from a particle based model to one which

generalizes particle interactions in terms of an interaction between coupled statistical fields: the average macroscopic density and the chemical potential, which generates it. Motivated by the particle theory, each diblock copolymer is modeled as a continuous Gaussian chain, so that the interaction between two neighboring monomers is expressed through a linearly elastic potential (the so-called harmonic stretching potential), and the distribution of the bond vectors between them is assumed to be Gaussian. The configuration of a diblock copolymer is specified by the space curve $\mathbf{r}(s)$, where the sub-chain described by $0 < s < fN$ is occupied by monomers of type A, and the subchain described by $fN < s < N$ is occupied by monomers of type B. Here, N is the index of polymerization, and f is the volume fraction of the A monomer sub-chain compared to the whole chain. In a system of many such copolymers, the effect that a monomer experiences due to the presence of other polymer chains is expressed through a spatially varying continuous chemical potential field $w(\mathbf{r})$, which is self-consistent as it is generated internally by the monomers in those chains.

The total potential energy $U[\mathbf{r}(s)]$ of a particular configuration $\mathbf{r}(s)$ is found as the sum of the harmonic stretching energy and the spatially varying chemical potential field. The probability density of observing a particular equilibrium configuration with potential energy $U[\mathbf{r}(s)]$ is described by the Boltzmann distribution, and the partition function is then defined as the functional integral of these probabilities over all possible space curves $\mathbf{r}(s)$. The particle to field transformations are then employed to approximately represent the partition function as a functional integral over the fluctuating density and fluctuating inhomogeneous chemical potential fields, which are coupled to each other through nonlinear modified diffusion equations. The free energy of the system is derived from the partition function and can be written in a closed form by introducing the key SCFT assumption, namely the *mean-field approximation*, by which the partition function is assumed to be dominated by a single potential field $w^*(\mathbf{r})$. This "mean field" is found as a stationary point of the complex-valued effective Hamiltonian, and once calculated it also determines the stationary values of the free energy.

The mean field approximation is exact only in the limit $N \to \infty$. This can be explained through the notion of the effective coordination number, which can be interpreted as the average number of polymer chains occupying the volume spanned by one chain of interest. When the coordination number is small, positional changes in neighboring particles significantly affect the potential field exerted on the monomers in the chain of interest. However, when the coordination number is large, the particle induced fluctuations of the field average

out due to their large number, and their joint effect can thus be reasonably approximated by a mean chemical potential field. The effective coordination number grows like $\sqrt{N}$, hence the mean field approximation is exact only for infinitely long polymer chains. In this mean field approximation, parameters χN and f fully describe the phase behaviour of diblock copolymers.

Analytical determination of stationary points is difficult, and standard approach is to numerically minimize the spectral coefficients of the effective Hamiltonian. The basis for the spectral decomposition is typically chosen so that it shares the symmetry of potential minimizing structures, guided by the experimentally observed phases. The main reason for this ansatz based choice is that simulations initiated from non-biased random initial configurations almost always result in steady states with defects breaking up the periodicity of the expected pure phase. These states look like metastable states, which are abundant in experiments, and are used as clues as to what the minimizing structure may be. Simulations are then initiated with configurations exhibiting these structures, and energies of the resulting steady states are computed with the goal of finding the minimizing phase.

Figure 1.4 shows the SCFT phase diagram in comparison with the experimental observations for polyisoprene-polystyrene diblock copolymers due to Khandpur et al. [18]. The two phase diagrams are qualitatively similar, with a few exceptions. Notably, the hexagonally perforated lamellar phase (PL) is not present in the SCFT diagram, as theoretical calculations predict that this phase is just a long lasting metastable state. This induced further experimental examinations of the PL phase, which led to the agreement between experimental and theoretical results [13]. Another notable difference between the two diagrams pertains to the symmetry of the SCFT diagram around $f_A = 0.5$, resulting from the consideration of conformationally symmetric diblock melts whereby the average lengths of the two constituent monomer species are assumed to be the same. On the other hand, the experimental diagram is asymmetric about $f_A = 0.5$ as the Kuhn statistical length l is different for the PI and PS monomers, and χ does not fully describe the PI-PS interactions. Lastly, we note that all order-order transition curves in the SCFT diagram converge to the critical point $(f, \chi N) = (0.5, 10.495)$, as predicted by Leibler in [19], while disorder is stable well beyond $\chi = 10.495$ in the experimental phase diagram, and direct order-disorder transitions are possible for all phases but the PL one. This discrepancy is a consequence of the mean field approximation.

A great text examining the SCFT theory in detail is available in [12].

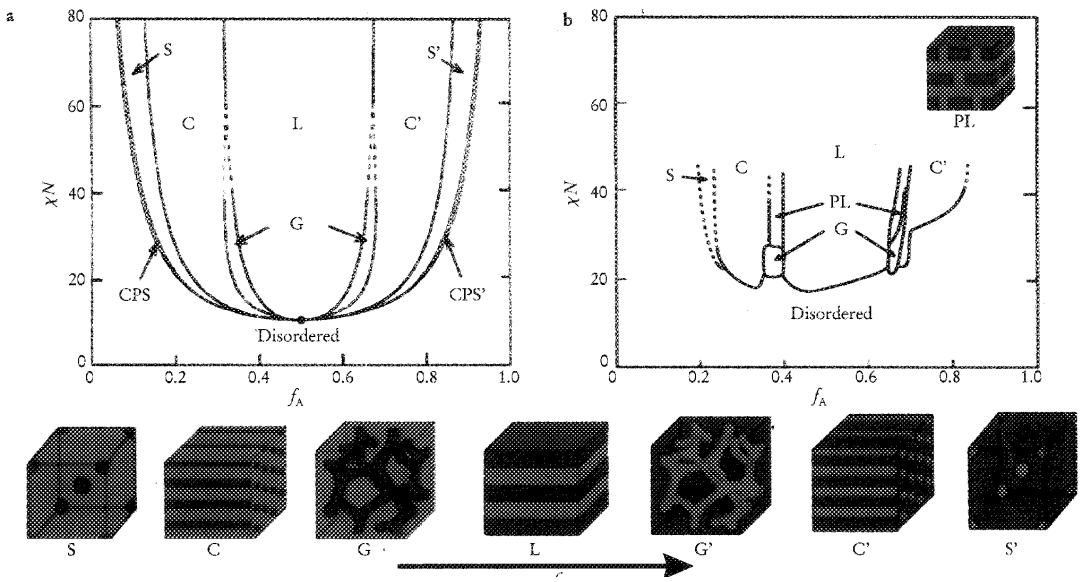

Figure 1.4: Taken from Bates and Fredrickson [2]: a) SCFT phase diagram of Matsen and Schick [21] for the self-assembly of diblock copolymers: The molecular weight f is denoted by f_A and the phases are labeled L for lamellar, G for gyroid, C for hexagonally packed cylinders, S for body centered cubic spheres, and CPS for close packed spheres. b) Experimental phase diagram for polyisoprene-polystyrene by Khandpur et al. [18]. The hexagonally perforated lamellar phase (PL) was later shown to be a long lasting metastable phase [13], in agreement with the SCFT results. In both diagrams, dotted lines represent extrapolations of phase transition curves.

1.3 Ohta-Kawasaki Density Functional Theory

A simpler theory for phase diagram prediction is derived from the SCFT approach by linearizing the dependence of the monomer density on the chemical potential field, as was shown in [5]. The resulting theory is called a density functional theory (DFT), and was first proposed by Ohta and Kawasaki [23]. It entails minimization of a nonlocal Cahn-Hilliard-like free energy defined in terms of the relative monomer density difference. This free energy differs from the standard Cahn-Hilliard free energy in the presence of the extra nonlocal term, which reflects the fact that the monomer chains are chemically bonded. Consequently, the energy is referred to as the nonlocal Cahn-Hilliard functional, and is written as

$$\int_\Omega \frac{\varepsilon^2}{2}|\nabla u|^2 + \frac{(1-u^2)^2}{4}\,dx + \frac{\sigma}{2}\int_\Omega\int_\Omega G(x,y)\,(u(x)-m)\,(u(y)-m)\,dx\,dy, \quad (1.3.2)$$

where u represents the difference between the local densities of monomers A and B, ε is the interfacial thickness at the A and B monomer intersections, σ is inversely proportional to the square of the index of polymerization N, m is the average density, i.e. $m = \fint_\Omega u$, and G denotes the Green's function of $-\triangle$ on $\Omega \subset \mathbb{R}^n$ with periodic boundary conditions. Minimizers of (1.3.2), computed over all u with mass average set to m, represent the self-assembling morphologies of diblock copolymers, as predicted by the Ohta-Kawasaki density functional theory.

This theory is consistent with the self-consistent mean field theory in the selection of material parameters which drive the phase behaviour. The two significant parameters in the density functional theory, $\gamma = \frac{1}{\varepsilon\sqrt{\sigma}}$ and m, correspond to the SCFT physically significant quantities χN and f. The exact relationships are presented in Chapter 2.

1.4 Phase Diagram via the Gradient Flow Approach to the Ohta-Kawasaki Theory

In this thesis we perform a thorough phase diagram calculation via the Ohta-Kawasaki density functional approach. That is, given parameter values γ and m, we minimize the nonlocal Cahn-Hilliard functional over all u constrained to have a constant average m, and geometrically characterize the minimizers. In particular, we adopt the gradient flow approach to the density functional theory, which leads us to the modified Cahn-Hilliard equation:

$$\frac{\partial u}{\partial t} = \triangle\left(-\varepsilon^2\triangle u - u + u^3\right) - \sigma(u - m) \tag{1.4.3}$$

as the evolution equation of the system, as shown by Choksi et al. in [4]. The solutions of this equation are considered both analytically and numerically on the cube $\Omega = \left[-\frac{L}{2}, \frac{L}{2}\right]^n$ with periodic boundary conditions. We choose this approach because of the ansatz-free nature of the density functional theory, which allows for direct analytic and numerical study of the free energy through the above evolution equation.

A major drawback of the common implementations of the self-consistent mean field theory are their dependence on a priori assumptions for the basic symmetry of the minimizing structures. Most analytical and numerical studies within the framework of this theory are

limited to considering symmetries derived from experimental observations of block interfaces, which resemble constant mean curvature surfaces, that is surfaces with minimal area subject to a volume constraint [2, 21]. This hinders the numerical discovery of new minimizing structures which are yet to be observed experimentally and also disregards the fact that due to the connectivity of the chains the actual minimizers do not have to be characterized by constant mean curvature interfaces.

On the other hand, the linearizing approximation introduced in the SCFT raises the question whether the subsequently derived density functional theory preserves the essential physics of the self-assembling process. An encouraging fact is that all of the phases which have been numerically predicted by the SCFT have also been predicted through the numerical ansatz-free minimization of the nonlocal Cahn-Hilliard functional ([30]). This leads us to believe that the prediction of qualitative morphologies may necessitate only the application of the simplified physics captured by this density functional theory.

In order to determine whether density functional theory can be used to describe the qualitative phase behaviour of diblock copolymers, we would need to derive the three-dimensional phase diagram and compare it to the SCFT and experimental diagrams. Global analytical results are difficult to obtain, so this would necessitate exhaustive three dimensional numerical simulations of (1.4.3). However, this is not a simple task, partly due to the high computational complexity of the numerical implementation. Consequently, we choose to focus on a simpler problem and define the goal of this thesis to be the derivation of a two-dimensional phase diagram for the self-assembly of diblock copolymers. This problem is interesting in its own right, and can be used as a test case for the future derivation of the full three-dimensional phase diagram.

To our knowledge, no phase diagrams have been computed via the gradient flow approach to the Ohta-Kawasaki theory, and in particular no phase diagrams derived via this theory have been expressed in terms of the experimental and SCFT parameters, χN and f. Our two-dimensional phase diagram will be computed in terms of material parameters equivalent to χN and f, and this will enable its direct qualitative comparison with the experimental and SCFT diagrams. This comparison will of course be truly relevant only once the diagram is extended to three dimensions.

1.5 Thesis Layout

The general layout of the thesis is as follows. In Chapter 2 we present the mathematical model derived from the Ohta-Kawasaki density functional theory. The modified Cahn-Hilliard equation is derived as the model PDE via the gradient theory approach to the original variational problem. The PDE is rescaled to reflect the dependence on m and γ, as the only two parameters which drive the phase behaviour of diblock copolymers. In Chapter 3, we present an asymptotic study of the ordered PDE solutions near the order-disorder transition. Minimizing structures and phase transition curves are characterized via the center manifold theory and energy arguments, and the phase diagram near the order-disorder transition is derived. In Chapter 4, we present three numerical schemes as good candidates for PDE simulations, which are necessary for the extension of the asymptotically derived phase diagram. Their accuracy, stability properties, and computational times are compared in order to find the most suitable discretization scheme. In Chapter 5, we present numerical simulations of the PDE for a large set of (m, γ) values, categorize the computed steady states, and derive the numerical phase diagram. Lastly, in Chapter 6, we summarize our findings and compare the asymptotic and numerical results. We also draw a qualitative comparison between our phase diagram and the SCFT and experimental ones, and conclude by recommending directions for future research of this topic.

Chapter 2

Mathematical Model

We model the self-assembly of diblock copolymers via the gradient flow approach to the Ohta-Kawasaki density functional theory. The model PDE is derived as the H^{-1} gradient flow of the nonlocal Cahn-Hilliard energy, and rescaled to show dependence on two parameters, m and γ, which are equivalent to the SCFT physically significant quantities, f and χN.

2.1 The Variational Problem

We begin the derivation of the mathematical model for the two-dimensional phase separation of diblock copolymers, by considering the following reformulation of the Ohta-Kawasaki density functional theory, introduced in section 1.3.

We let $\Omega \subset \mathbb{R}^2$ denote a flat torus of diameter L, i.e. $\Omega = \left[-\frac{L}{2}, \frac{L}{2}\right]^2$, with the implied periodic boundary conditions. The Ohta-Kawasaki theory entails minimization of the nonlocal Cahn-Hilliard functional

$$E_{\varepsilon,\sigma}(u) := \frac{\varepsilon^2}{2} \int_\Omega |\nabla u|^2 \, dx \; + \; \int_\Omega \frac{1}{4}(1-u^2)^2 \, dx \; + \; \frac{\sigma}{2} \int_\Omega |\nabla v|^2 \; dx, \tag{2.1.1}$$

over all $u \in \left\{ u \in H^1(\Omega, [-1,1]) \;\middle|\; \fint_\Omega u \, = \, m \right\}$.

Here, u represents the relative monomer density, namely: $u = \rho_A - \rho_B$, $m \in (-1,1)$ is the fixed average of u over Ω, ε represents the rescaled interfacial thickness at the A and B monomer intersections, σ is inversely proportional to the square of the index of

polymerization N, and v is related to u via the boundary value problem

$$-\triangle v \,=\, u \,-\, m, \tag{2.1.2}$$

with periodic boundary conditions for v on $\partial\Omega$.

This variational problem is a reformulation of the original Ohta-Kawasaki model, as the last term of the energy functional (2.1.1) differs from the last term of (1.3.2), which reads $\frac{\sigma}{2}\int_\Omega\int_\Omega G(x,y)\,(u(x)-m)\,(u(y)-m)\,dx\,dy$. To see how this transformation is introduced, we recall that the representation formula for the solution of the Poisson problem (2.1.2) is

$$v(x) = \int_\Omega G(x,y)\,(u(y)-m)\,dy,$$

where G denotes the Green's function of $-\triangle$ on the torus Ω. Then,

$$\begin{aligned}\int_\Omega |\nabla v|^2\,dx &= -\int_\Omega v(x)\triangle v(x)\,dx = \int_\Omega v(x)\,(u(x)-m)\,dx\\ &= \int_\Omega\int_\Omega G(x,y)\,(u(y)\,-\,m)\,(u(x)\,-\,m)\,dx\,dy.\end{aligned}$$

Here we used integration by parts, invoked periodic boundary conditions, and showed the equivalence of the two terms on a torus. We note that the last term in (2.1.1) is a version of the H^{-1} norm squared of the function $u(x)-m$, that is, $\int_\Omega |\nabla v|^2 = \|u-m\|^2_{H^{-1}(\Omega)}$.

Minimizers u of the nonlocal Cahn-Hilliard energy fully determine the equilibrium morphology of the diblock copolymer due to the incompressibility constraint, $\rho_A + \rho_B = 1$. Furthermore, the physically meaningful local values of u are bound to the $[-1,1]$ interval, with regions where $u = 1$ (respectively -1) representing pure A (respectively pure B) phases.

In order to gain some intuition about what the minimizers of the nonlocal Cahn-Hilliard functional (2.1.1) should look like, we describe the competing effect of the three constituent energies.

The interfacial energy, $\frac{\varepsilon^2}{2}\int_\Omega |\nabla u|^2\,dx$, penalizes rapid changes in monomer density u and thus concentrates along the interface between the A and B-rich domains. Its minimization forces the configurations u to have as few transition regions as possible with the transition interface itself being a constant mean curvature surface.

The bulk energy (or double-well energy), $\int_\Omega \frac{1}{4}(1-u^2)^2\,dx$, has equal minima at $u=-1$ and $u=1$ and thus prefers a state in which the system is segregated into pure A and pure B domains.

Lastly, the nonlocal interaction energy, $\frac{\sigma}{2}\int_\Omega |\nabla v|^2\,dx$, penalizes densities u whose local averages are not equal to m. In this sense, this energy term is a long-range (or nonlocal) one, while-as the first two energy terms are short-range (or local).

The level-sets of the minimizers of (2.1.1) are thus expected to be approximate constant mean curvature surfaces with the length scale of the A-rich and B-rich domains depending on the length of the monomer chains through the parameter σ. The first two energy terms drive the minimizers to form A and B-rich domains separated by minimal area interfaces, as in the standard Cahn-Hilliard case. However, the connectivity of the chains, which is accounted for in the nonlocal energy term, counterbalances this drive and may lead to only approximate constant mean curvature interfaces.

2.2 PDE Formulation

The constrained minimization of the nonlocal Cahn-Hilliard functional can be formulated in terms of a PDE problem, whose steady states are stationary values of the functional. We adopt the gradient flow approach, according to which:

$$u_t = -\text{grad}\, E_{\varepsilon,\sigma}(u), \tag{2.2.3}$$

that is, the evolution of the density field u is given by the gradient flow of the nonlocal Cahn-Hilliard energy (2.1.1). This theory has been applied to the standard Cahn-Hilliard case and is described in detail in [9].

The symbol grad denotes a constrained gradient, that is a gradient on the manifold, in some Hilbert space, defined by $\frac{d}{dt}\int_\Omega u(x,t)\,dx = 0$. Letting $\delta > 0$, we define $\text{grad}_H E_{\varepsilon,\sigma}(u)$ to be an element of H, such that for all

$$W(t) : [0,\delta) \to H$$

with $W(0) = u$, the following relation holds

$$\left.\frac{d}{dt}E_{\varepsilon,\sigma}(W(t))\right|_{t=0} = \left\langle \text{grad}_H E_{\varepsilon,\sigma}(u)\,,\, \left.\frac{\partial W}{\partial t}\right|_{t=0}\right\rangle_H .$$

For any $w \in H$, the above definition takes on the following form

$$\left.\frac{d}{dt}E_{\varepsilon,\sigma}(u+tw)\right|_{t=0} = \langle \text{grad}_H E_{\varepsilon,\sigma}(u)\,,\, w\rangle_H . \tag{2.2.4}$$

This definition agrees with our usual notion of the gradient when H is a finite dimensional space. To see this, let's consider $H = \mathbb{R}^2 = \{(u_1, u_2) | \, u_1, u_2 \in \mathbb{R}\}$ and define $F : H \to \mathbb{R}$ by

$$F(\mathbf{u}) = u_1 u_2,$$

where $\mathbf{u} = (u_1, u_2) \in H$. We can employ the usual notion of the gradient to find

$$\text{grad} F(\mathbf{u}) = \left(\frac{\partial}{\partial u_1}, \frac{\partial}{\partial u_2} \right) u_1 u_2 = (u_2, u_1). \tag{2.2.5}$$

We now turn to the definition of the gradient (2.2.4), and recover $\text{grad} F(\mathbf{u})$ as follows. For any $\mathbf{w} = (w_1, w_2) \in H$ and $t \in \mathbb{R}$, we consider

$$\begin{aligned} \frac{d}{dt} F(\mathbf{u} + t\mathbf{w}) \Big|_{t=0} &= \frac{d}{dt} F(u_1 + t w_1, u_2 + t w_2) \Big|_{t=0} \\ &= u_1 w_2 + u_2 w_1 \\ &= (u_2, u_1) \cdot (w_1, w_2) \\ &= \langle \text{grad}_H F(\mathbf{u}), \mathbf{w} \rangle_H . \end{aligned}$$

But this is precisely the definition of a directional derivative, with the direction being given by $\mathbf{w}$. Thus we find that (2.2.4), applied in a finite dimensional space, is equivalent to the definition of a directional derivative. Unlike the usual definition of the gradient given in (2.2.5), it defines the gradient implicitly through the notion of directional derivatives. We generalize this idea in an infinite dimensional function space, by extending the dot product of vectors into an inner product of functions. Unlike in the finite dimensional case, there are many possible choices for the inner product in an infinite dimensional function space, and each one depends on the particular choice of the Hilbert space.

The gradient flow approach does not necessarily describe the true dynamics of the dissipative system that we wish to model, but rather chooses an evolution that follows the steepest path down the energy well until a minimum is achieved. Time is an artificial variable, which is used to parameterize the motion throughout the energy landscape. This particular choice of artificial dynamics is made since it ensures that the free energy will decrease in time:

$$\frac{d}{dt} E_{\varepsilon,\sigma}(u) = \left\langle \text{grad}\, E_{\varepsilon,\sigma}(u), \frac{\partial u}{\partial t} \right\rangle_H = - \, || \text{grad}\, E_{\varepsilon,\sigma}(u) | \, |^2 \leq 0.$$

Thus, the configuration u will evolve towards a steady state of the evolution law (2.2.3), and the reached steady state will precisely be a local minimizer of the free energy. Since

our interest is in the steady states, rather than the dynamics of the process, the choice of the gradient flow approach is an appropriate one. Alternatively, we could find the steady states through a direct minimization of the energy functional, or Monte Carlo simulations. However, both of these approaches are computationally intensive and the former is highly dependent on the initial guess due to the non-convex nature of the functional.

Having chosen the gradient flow approach, we still need to pick a particular Hilbert space in which to evaluate the gradient, since each one leads to a different evolution equation. We will show in what follows that the standard L^2 space may not be the most convenient choice, and instead we will choose the nonstandard H^{-1} space. Evaluation of the gradient in this space will lead us to the modified Cahn-Hilliard equation as the mathematical model for the self-assembly of diblock copolymers.

2.2.1 L^2 Equation

We wish to derive an evolution equation for the density u as a gradient flow of (2.1.1) with respect to the L^2 inner product. To this end, we begin by considering the Hilbert space

$$H := \left\{ f \in L^2(\Omega) \,\middle|\, \int_\Omega f\,dx = 0 \right\},$$

associated with the L^2 inner product

$$\left\langle f, \tilde{f} \right\rangle_H := \int_\Omega f\,\tilde{f}\,dx,$$

where $f, \tilde{f} \in H$. We proceed to compute $\operatorname{grad}_H E_{\varepsilon,\sigma}(u)$ with respect to the parallel space $u + H$, where u satisfies $⨍ u = m$. We consider $u + tw$, for any $w \in H$ and $t \in [0, \delta)$, and let $v, \tilde{v} \in H$ solve

$$-\triangle v = u - m \quad \text{and} \quad -\triangle \tilde{v} = w, \qquad \text{in } \Omega.$$

We find

$$\begin{aligned}
\left.\frac{d}{dt} E_{\varepsilon,\sigma}(u+tw)\right|_{t=0} &= \frac{d}{dt}\left[\int_\Omega \frac{\varepsilon^2}{2}|\nabla(u+tw)|^2 + \frac{(1-(u+tw)^2)^2}{4} + \frac{\sigma}{2}|\nabla v + t\nabla\tilde{v}|^2\,dx\right]_{t=0} \\
&= \int_\Omega \varepsilon^2\,\nabla u\cdot\nabla w + (u^3-u)\,w + \sigma\,\nabla v\cdot\nabla\tilde{v}\,dx \\
&= \int_\Omega \left(-\varepsilon^2\triangle u - u + u^3\right)\,w - \sigma\,v\,\triangle\tilde{v}\,dx \\
&= \int_\Omega \left(-\varepsilon^2\triangle u - u + u^3 + \sigma\,v\right)\,w\,dx \\
&= \left\langle \left(-\varepsilon^2\triangle u - u + u^3 + \sigma\,v\right)\,,\, w \right\rangle_H .
\end{aligned}$$

In the above calculation we use integration by parts and invoke the periodic boundary conditions. Recalling the definition of the constrained gradient (2.2.4), we consequently find

$$\mathrm{grad}_H E_{\varepsilon,\sigma}(u) = -\varepsilon^2 \triangle u - u + u^3 + \sigma\, v,$$

and the L^2 evolution equation system, as prescribed by (2.2.3), is thus given by

$$\begin{aligned} \frac{\partial u}{\partial t} &= \varepsilon^2 \triangle u + u - u^3 - \sigma\, v, && (2.2.6)\\ -\triangle v &= u - m. && (2.2.7) \end{aligned}$$

This system is discarded as a good model since it does not conserve mass in general.

$$\begin{aligned} \frac{d}{dt}\int_\Omega u\, dx &= \int_\Omega \varepsilon^2 \triangle u + u - u^3 - \sigma\, v\, dx \\ &= \int_{\partial\Omega} \varepsilon^2\, \partial_\nu u\; dx + \int_\Omega u - u^3 - \sigma\, v\, dx \\ &= \int_\Omega u - u^3 + \sigma\, v\, dx, \end{aligned}$$

and this integral is in general nonzero. We conclude that the L^2 evolution system (2.2.6)-(2.2.7) leads to a physically sound model only if it is solved under the constraint $\fint_\Omega u = m$.

2.2.2 H^{-1} Equation

We now consider the Hilbert space H,

$$H := \left\{ f \in L^2(\Omega) \;\middle|\; \int_\Omega f\, dx = 0 \right\},$$

associated with the H^{-1} inner product

$$\left\langle f, \tilde{f} \right\rangle_H := \int_\Omega \nabla v \cdot \nabla \tilde{v}\; dx,$$

where $f, \tilde{f} \in H$, and $v, \tilde{v}$ denote the functions in H satisfying

$$-\triangle v = f \quad \text{and} \quad -\triangle \tilde{v} = \tilde{f} \quad \text{in} \quad \Omega.$$

The norm in this non-standard Hilbert space is

$$\|f\|_H^2 = \int_\Omega |\nabla v|^2, \qquad (2.2.8)$$

or equivalently, in Fourier space,

$$\|f\|_H^2 \;=\; \sum_{|\mathbf{k}|\neq 0} \frac{|\widehat{f}(\mathbf{k})|^2}{|2\pi\mathbf{k}|^2},$$

where $\widehat{f}(\mathbf{k})$ represents the $\mathbf{k}$-th Fourier coefficient of f. This version of the H^{-1} norm has a natural interpretation as the norm associated with the dual space of H_0^1 (functions in H^1 with zero average) with respect to the inner product. That is,

$$\|f\|_H^2 \;=\; \sup_{\psi\in C_0^\infty(\Omega)} \frac{\left(\int_\Omega f\,\psi\right)^2}{\|\nabla\psi\|^2_{L^2(\Omega)}}, \tag{2.2.9}$$

where $C_0^\infty(\Omega)$ denotes the space of C^∞ functions on the torus Ω with zero mass average. We easily see that (2.2.8) follows directly from (2.2.9):

$$\begin{aligned}
\|f\|_H^2 &= \sup_{\psi\in C_0^\infty(\Omega)} \frac{\left(\int_\Omega f\,\psi\right)^2}{\|\nabla\psi\|^2_{L^2(\Omega)}} = \sup_{\psi\in C_0^\infty(\Omega)} \frac{\left(\int_\Omega -\triangle v\,\psi\right)^2}{\int_\Omega |\nabla\psi|^2} \\
&= \sup_{\psi\in C_0^\infty(\Omega)} \frac{\left(\int_\Omega \nabla v\cdot\nabla\psi\right)^2}{\int_\Omega |\nabla\psi|^2} = \frac{\left(\int_\Omega \nabla v\cdot\nabla v\right)^2}{\int_\Omega |\nabla v|^2} \\
&= \int_\Omega |\nabla v|^2.
\end{aligned}$$

The supremum is achieved for $\psi = v$, since the dot product of two vectors attains its maximum value when the two vectors are parallel.

We now recall the definition of a constrained gradient (2.2.4) and let u be such that $\fint u = m$. We proceed to compute $\mathrm{grad}_H E_{\varepsilon,\sigma}(u)$ with respect to the parallel space $u + H$. As before, for $w \in H$ and $t \in [0,\delta)$, we consider $u + tw$, and let $v, \tilde{v} \in H$ solve

$$-\triangle v \;=\; u - m \quad \text{and} \quad -\triangle\tilde{v} \;=\; w, \qquad \text{in } \Omega.$$

We find

$$\begin{aligned}
\left.\frac{d}{dt}E_{\varepsilon,\sigma}(u+tw)\right|_{t=0} &= \int_\Omega \varepsilon^2\,\nabla u\cdot\nabla w + (u^3-u)\,w + \sigma\,\nabla v\cdot\nabla\tilde{v}\,dx \\
&= \int_\Omega \left(u^3 - u \,-\, \varepsilon^2\triangle u\right)\, w \;+\; \sigma\,\nabla v\cdot\nabla\tilde{v}\,dx \\
&= \int_\Omega \left(u^3 - u \,-\, \varepsilon^2\triangle u\right)\,(-\triangle\tilde{v}) \;+\; \sigma\,\nabla v\cdot\nabla\tilde{v}\,dx \\
&= \int_\Omega \nabla\left(-\varepsilon^2\triangle u \,-\, u + u^3 \;+\; \sigma\, v\right)\cdot\nabla\tilde{v} \\
&= \left\langle -\triangle\left(-\varepsilon^2\triangle u \,-\, u + u^3 \;+\sigma\, v\right),\, w\right\rangle_H .
\end{aligned}$$

Thus

$$\begin{aligned} \mathrm{grad}_H E_{\varepsilon,\sigma}(u) &= -\triangle\left(-\varepsilon^2\triangle u - u + u^3 + \sigma\, v\right) \\ &= -\triangle\left(-\varepsilon^2\triangle u - u + u^3\right) + \sigma(u-m), \end{aligned}$$

and (2.2.3) gives

$$\frac{\partial u}{\partial t} = \triangle\left(-\varepsilon^2\triangle u - u + u^3\right) - \sigma(u-m). \tag{2.2.10}$$

We have thus derived the H^{-1} gradient flow equation, known in the mathematics community as the modified Cahn-Hilliard equation. This equation without the last nonlocal term is precisely the equation that was derived by Cahn and Hilliard in the 1950's as a model for phase separation of binary alloys. This evolution equation, unlike the L^2 one, does preserve mass. To see this, we set

$$w(t) := \int_\Omega u(x,t)\, dx,$$

and integrate (2.2.10) over Ω, as follows

$$\begin{aligned} \frac{dw}{dt} &= \int_\Omega \triangle\left(-\varepsilon^2\triangle u - u + u^3\right) - \sigma(u-m)\, dx \\ &= \int_{\partial\Omega} \partial_\nu\left(-\varepsilon^2\triangle u - u + u^3\right)\, dS(x) - \int_\Omega \sigma(u-m)\, dx \\ &= \int_{\partial\Omega} -\varepsilon^2\, \partial_\nu\triangle u + (3u^2-1)\, \partial_\nu u\; dS(x) - \int_\Omega \sigma(u-m)\, dx \\ &= -\int_\Omega \sigma(u-m)\, dx \\ &= -\sigma\left(w(t) \,-\, m|\Omega|\right) \\ &= 0. \end{aligned}$$

Here we invoked the periodic boundary conditions and the initial time condition $\fint u = m$, i.e. $w(0) = m|\Omega|$. If this initial condition was not satisfied, the mass average would adjust to m exponentially fast, since we derived in the above calculation that

$$\frac{dw}{dt} \,=\, -\sigma\left(w(t) \,-\, m|\Omega|\right).$$

2.3 Rescaled Energy Functional and Model PDE

We now present a rescaling of the model energy functional (2.1.1) and PDE (2.2.10), which shows a fundamental dependence on the parameters $\varepsilon\sqrt{\sigma}$ and m.

Introducing the variables

$$\tilde{x} = \sqrt{\sigma}\, x, \qquad \tilde{\Omega} = \sqrt{\sigma}\, \Omega, \qquad\qquad \tilde{\varepsilon} = \varepsilon \sqrt{\sigma}.$$

we find the rescaled free energy to be

$$\tilde{\varepsilon}^2 \int_{\tilde{\Omega}} |\tilde{\nabla} u|^2 \, d\tilde{x} \;+\; \int_{\tilde{\Omega}} \frac{1}{4}(1-u^2)^2 \, d\tilde{x} \;+\; \int_{\tilde{\Omega}} |\tilde{\nabla} v|^2 \, d\tilde{x}, \tag{2.3.11}$$

where

$$-\tilde{\triangle} v \;=\; u - m \qquad \text{in } \tilde{\Omega}.$$

Similarly, introducing

$$\tilde{u} = u - m, \qquad \tilde{x} = \sqrt{\sigma}\, x, \qquad \tilde{L} = \sqrt{\sigma}\, L, \qquad \tilde{t} = \sigma\, t, \qquad \tilde{\varepsilon} = \varepsilon \sqrt{\sigma},$$

we find the rescaled modified Cahn-Hilliard equation to be

$$\frac{\partial \tilde{u}}{\partial \tilde{t}} \;=\; -\tilde{\varepsilon}^2 \, \tilde{\triangle}^2 \tilde{u} \;+\; \tilde{\triangle} \left(\tilde{u}^3 + 3m\tilde{u}^2 \right) \;-\; (1 - 3m^2) \tilde{\triangle} \tilde{u} \;-\; \tilde{u} \qquad \text{in } \tilde{\Omega}. \tag{2.3.12}$$

Thus, the rescaled energy functional and model equation depend solely on parameters $\tilde{\varepsilon} = \varepsilon\sqrt{\sigma}$ and m. The domain length, $\tilde{L} = \sqrt{\sigma}\, L$, is not a relevant bifurcation parameter as long as it is sufficiently large, i.e. larger than the largest scale appearing in the phase geometry. This is given by the phase domain length of the minimizing structures, which scales like $\left(\frac{\varepsilon}{\sigma}\right)^{1/3}$, as noted in [3].

The dependence on the combined parameter $\tilde{\varepsilon} = \varepsilon\sqrt{\sigma}$ can also be seen through its effect on the degree of segregation of the two monomer species. To see this, we note that in addition to the inherent periodicity scale of the minimizing structures, mentioned above, another important scale for the minimizers is determined by the interfacial thickness ε. The degree of phase separation is controlled by the ratio of these length scales

$$\left(\frac{\varepsilon}{\sigma}\right)^{1/3} \; \varepsilon^{-1} \;=\; \frac{1}{\left(\varepsilon \sqrt{\sigma}\right)^{2/3}}, \tag{2.3.13}$$

where we observe the emergence of $\varepsilon\sqrt{\sigma}$.

Most importantly, $\varepsilon\sqrt{\sigma}$ is found to be related to the physically significant quantity χN. The leading order relationships between the dimensionless parameters ε, σ, m, and L from the Ohta-Kawasaki density functional theory and the SCFT parameters χ, N, l, and f, are derived in [5], and assume the following form:

$$\varepsilon^2 \sim \frac{l^2}{f\,(1-f)\,\chi\,L^2} \qquad \sigma \sim \frac{L^2}{f^2(1-f)^2\,l^2\,\chi\,N^2} \qquad m = 2f-1. \tag{2.3.14}$$

The SCFT significant quantity, χN, is therefore related to ε and σ via:

$$\chi\,N \sim \frac{1}{f^{3/2}\,(1-f)^{3/2}\,\varepsilon\,\sqrt{\sigma}}. \tag{2.3.15}$$

Given that we would like to identify a parameter in the DFT theory which corresponds to χN from the SCFT theory, we introduce the parameter

$$\gamma := \frac{1}{\tilde{\varepsilon}} = \frac{1}{\varepsilon\,\sqrt{\sigma}}.$$

According to (2.3.14) and (2.3.15), $m \sim f$ and $\gamma \sim \chi\,N$. Thus, our model approach contains two bifurcation parameters, γ and m, analogous to χN and f from the SCFT theory.

The rescaled nonlocal Cahn-Hilliard energy functional is then given by:

$$E_\gamma(u) = \frac{1}{\gamma^2}\int_\Omega |\nabla u|^2\,dx + \int_\Omega \frac{1}{4}(1-u^2)^2\,dx + \int_\Omega |\nabla v|^2\,dx, \tag{2.3.16}$$

and rescaled model PDE by:

$$\frac{\partial u}{\partial t} = -\frac{1}{\gamma^2}\triangle^2 u + \triangle\left(u^3 + 3mu^2\right) - (1-3m^2)\triangle u - u. \tag{2.3.17}$$

Note that we omit tildes from variable names for easier presentation. Furthermore, recall that the rescaled variable u satisfies $\fint_\Omega u = 0$, since the average m was subtracted out.

We now proceed to determine the exact relationship between γ and χN, so that we could compare the SCFT diagram to ours, once we compute it. To this end, we rewrite (2.3.15) as follows,

$$\gamma = c f^{3/2}\,(1-f)^{3/2}\chi N, \tag{2.3.18}$$

and depict the factor $f^{3/2}(1-f)^{3/2}$ for $0.05 < f < 0.95$ in Figure 2.1.

We now recall that the SCFT theory predicts the order-disorder transition for symmetric diblocks ($f = 0.5$) to occur at the critical value $\chi N = 10.495$. Similarly, Choksi et al. [4] identify $\gamma = 2$ as the corresponding critical value in the (m, γ) phase plane. Substituting $\chi N = 10.495$, $f = 0.5$, and $\gamma = 2$ into (2.3.18), we find $c = 1.5246$, and so

$$\gamma = 1.5246\,f^{3/2}\,(1-f)^{3/2}\chi N \tag{2.3.19}$$

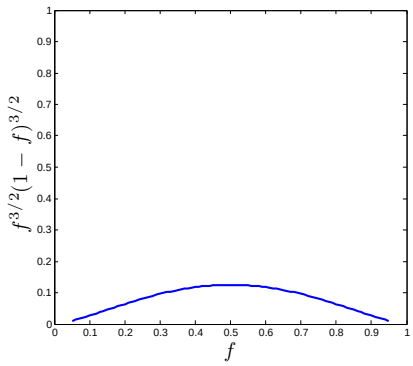

Figure 2.1: Plot of the factor $f^{3/2}(1-f)^{3/2}$ present in (2.3.18).

gives the exact f-dependent relationship between γ and χN. Combined with the exact relationship between m and f in (2.3.14), this fully determines the correspondence between the SCFT and our DFT parameters.

In particular, we can write $\gamma \approx 0.1905\,\chi N$, by approximating $f^{3/2}\,(1-f)^{3/2}$ with its maximum value attained at $f = 0.5$, and determine the range of γ values that correspond to the χN values considered in the SCFT phase diagram. Figure 1.4 indicates that $0 < \chi N < 80$ in the SCFT diagram, and so the corresponding γ values are $0 < \gamma < 15.2$.

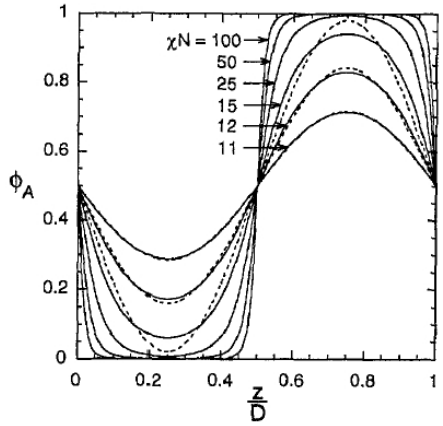

Figure 2.2: Taken from Matsen & Bates [20]: Lamellar profile of a symmetric diblock copolymer melt ($f = 0.5$) presented for various values of χN. ϕ_A is the relative density of monomers A, D is the size of the cubic cell containing one period of the phase, and $Z = \frac{2\pi z}{D}$ is the dimensionless length. Dashed lines represent first Fourier component approximations of the profiles at $\chi N = 10, 12$, and 15.

We can also determine the values of γ, which correspond to the weak, intermediate, and strong segregation regimes. The weak regime corresponds to small values of χN and is characterized by interfacial regions being of the same order as the domain lengths of the A and B pure blocks. The profiles are approximately sinusoidal and can be approximated by the first term of the Fourier decomposition of the density field u. On the other hand, the strong segregation regime corresponds to large values of χN and is characterized by the interfacial width being much smaller than the domain length of the A and B pure blocks. Matsen and Bates make the definition of a pure block more precise in [20] by defining it as a domain characterized by $\phi_A > 0.9999$, where ϕ_A represents the relative density of monomers of type A. They consider a lamellar profile, presented in Figure 2.2, and define the weak segregation regime by $10.495 < \chi N < 12$, the intermediate by $12 < \chi N < 50$, and the strong by $\chi N > 50$. Thus, correspondingly, the weak segregation regime is defined by $2 < \gamma < 2.3$, the intermediate by $2.3 < \gamma < 9.5$, and the strong by $\gamma > 9.5$.

Chapter 3

Analytic Results

We start our search for minimizing structures and phase transition curves by analytically investigating the model free energy and PDE. Rigorous results are difficult to obtain, so we take an asymptotic analysis approach to determine minimizers and their regions of validity close to the order-disorder transition. Asymptotic results provide a good setting for numerical investigation, which is necessary for a full description of the phase diagram for the self-assembly of diblock copolymers.

3.1 Rigorous Results

Rigorous results describing unique global minimizers of the nonlocal Cahn Hilliard functional are difficult to obtain. The only available rigorous result is given by the following theorem, which was presented by Choksi et al. in [4].

Theorem 3.1.1. *For any $m \in (-1, 1)$, the constant state $u \equiv m$ is the unique global minimizer to* (2.1.1) *if*

$$1 - m^2 \leq 2\,\varepsilon\,\sqrt{\sigma} \qquad \text{or} \qquad \gamma \leq \frac{2}{1-m^2}. \tag{3.1.1}$$

This result holds in any space dimension and for any L. The rigorous result (3.1.1) is optimal only for $m = 0$, so the true phase transition between disordered and ordered states is not analytically known. A numerical approximation of this true transition curve will be presented in Chapter 5.

However, there are many rigorous results pertaining to the linear stability of certain minimizers, and some of the results due to Ren and Wei are available in [25, 26, 27]. Furthermore, a weak result on the periodicity of minimizers addressing their energy distribution is presented by Alberti et al. in [1].

3.2 Linear Stability of the Constant State

We now examine the linear stability of the constant state as a function of γ and m. Linearizing the rescaled model PDE (2.3.17) about the homogeneous solution $u = 0$ gives

$$\frac{\partial w}{\partial t} = \mathcal{L}w := -\frac{1}{\gamma^2}\triangle^2 w - (1 - 3m^2)\triangle w - w.$$

Putting in the ansatz

$$w = e^{\lambda t + ik\cdot x},$$

one finds

$$\lambda = -\frac{1}{\gamma^2}|k|^4 + (1 - 3m^2)|k|^2 - 1.$$

The constant state is linearly unstable when $\lambda > 0$, that is when

$$(1 - 3m^2)^2 > \frac{4}{\gamma^2} \qquad \text{or} \qquad (1 - 3m^2) > \frac{2}{\gamma}, \tag{3.2.2}$$

since the discriminant of the quadratic equation $\lambda = 0$ is given by $(1 - 3m^2)^2 - \frac{4}{\gamma^2}$. Thus, the boundary of the region where the constant state is linearly stable is given by

$$\gamma = \frac{2}{1 - 3m^2}. \tag{3.2.3}$$

We refer to this curve as the order-disorder transition curve, or the ODT curve.

3.3 Asymptotic Results for Ordered States

Having presented results pertaining to the disordered phase, we now wish to characterize the ordered steady states of the modified Cahn-Hilliard equation. In particular, we want to determine their structure and stability near the order-disorder transition. To this end, we will use asymptotic approximations to find the non-trivial steady states, and energy arguments to determine their stability. All of the calculations in this sections will be performed in terms of the rescaled versions of the model PDE and energy, given by (2.3.17) and (2.3.16).

To determine the steady states, we need to solve the following problem

$$-\frac{1}{\gamma^2}\triangle^2 u + \triangle\left(u^3 + 3mu^2\right) - (1-3m^2)\triangle u - u = 0 \tag{3.3.4}$$

on the torus $\Omega = \left[-\frac{L}{2}, \frac{L}{2}\right]^2$. In particular, our goal is to determine the nontrivial solutions that bifurcate from the steady state $u_s = 0$, which is known to be linearly unstable above the ODT curve, given exactly by $\gamma = \frac{2}{1-3m^2}$. The implicit function theorem fails along this curve, since $\lambda = 0$, according to the previous section. Thus, we consider the mass to be given by Bm, for $|m| \ll 1$, $B \in \mathbb{R}$, and fix $\gamma = \frac{2}{1-3m^2} \sim 2 + 6m^2 + \cdots$.

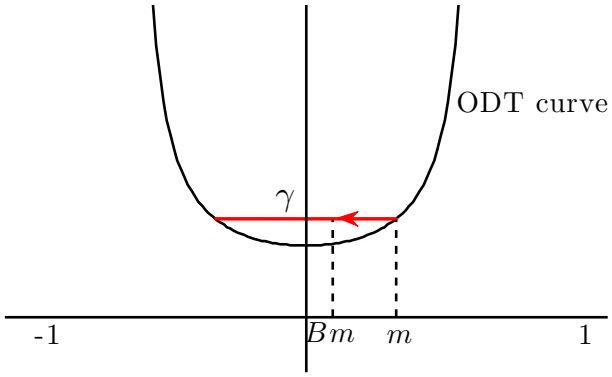

Figure 3.1: We fix γ to the value it attains on the ODT curve for some $|m| \ll 1$, and then consider the form of the solution for all mass values between $-m$ and m.

For simplicity, we will consider the 1D case first, and introduce an appropriate asymptotic expansion for u

$$u \sim m^\alpha u_1(x) + m^\beta u_2(x) + \ldots, \tag{3.3.5}$$

where $u_1 \neq 0$, since we are interested in nonzero solutions of 3.3.4, and $0 < \alpha < \beta$. Substituting this expansion into (3.3.4), leads to the following leading order equation:

$$\mathcal{O}\left(m^\alpha\right) : \mathcal{L}(u_1) = -\frac{1}{4}\triangle^2 u_1 - \triangle u_1 - u_1 = 0 \tag{3.3.6}$$

We now assume $u_1 = Ae^{ikx} + A^* e^{-ikx}$, where A^* is the complex conjugate of A, and $k \in \mathbb{R}$. Substituting this into the above expression leads to the following quadratic equation in k:

$$-\frac{1}{4}k^4 + k^2 - 1 = 0,$$

and thus $k = \sqrt{2}$. Imposing the periodic boundary conditions on u_1, we obtain

$$u_1\left(-\frac{L}{2}\right) = Ae^{-ikL/2} + A^*e^{ikL/2} = Ae^{ikL/2} + A^*e^{-ikL/2} = u_1\left(\frac{L}{2}\right),$$

and thus $A = A^*$ implying that $A \in \mathbb{R}$ and

$$u_1 = A\cos kx,$$

where we have merged a factor of 2 into A.

The constant A is still unknown, so we need to consider higher order terms in order to fully determine u_1. Substituting the expansion for u into (2.3.17) and keeping only the terms whose order is greater than $\mathcal{O}(m^\alpha)$, we obtain

$$m^\beta \mathcal{L}(u_2) + \triangle\left(\frac{3}{2}m^{\alpha+2}\triangle u_1 + m^{3\alpha}u_1^3 + 3Bm^{2\alpha+1}u_1^2 + 3B^2m^{\alpha+2}u_1\right) + h.o.t. = 0.$$

Balancing all terms: $\beta = 3\alpha = 2\alpha + 1 = \alpha + 2$, we obtain that $\alpha = 1$ and $\beta = 3$. Hence, the next order equation is

$$\mathcal{O}(m^3) : \mathcal{L}(u_2) = -\triangle\left(\frac{3}{2}\triangle u_1 + u_1^3 + 3Bu_1^2 + 3B^2u_1\right). \tag{3.3.7}$$

We would like to write the above equation in terms of u_1 only, and we can do so by invoking a solvability condition derived from the Fredholm alternative. In order to state this result, we consider the following equations:

$$Su = f, \tag{3.3.8}$$

$$Su_0 = 0, \tag{3.3.9}$$

$$S^*v = g, \tag{3.3.10}$$

$$S^*v_0 = 0, \tag{3.3.11}$$

where S^* is the adjoint of a Fredholm operator S. Then, the following Fredholm alternative holds:

1. either (3.3.9) has only the trivial solution $u_0 = 0$, and then (3.3.11) has only the trivial solution and equations (3.3.8) and (3.3.10) are uniquely solvable for any right-hand sides f and g, or

2. (3.3.9) has a nontrivial solution $u_0 \neq 0$ and then (3.3.11) has a nontrivial solution, and equations (3.3.8) and (3.3.10) are solvable if and only if $(f, v_0) = 0$ and $(g, u_0) = 0$. If they are solvable, their solutions are not unique.

The $\mathcal{O}(m^1)$ equation, $\mathcal{L}(u_1) = 0$, is in the general form of the equation (3.3.9), and the $\mathcal{O}(m^3)$ equation, $\mathcal{L}(u_2) = f$, is in the form of (3.3.8), with $\mathcal{L} = -\frac{1}{4}\triangle^2 - \triangle - 1$, and $f = -\triangle\left(\frac{3}{2}\triangle u_1 + u_1^3 + 3Bu_1^2 + 3B^2u_1\right)$. Furthermore, the linear operator $\mathcal{L}$ is self-adjoint, so the Fredholm alternative assures us that the $\mathcal{O}(m^3)$ equation is solvable when $(f, u_1) = 0$, since we are interested in nontrivial solutions u_1. This leads to the following solvability condition

$$\int_\Omega \left(\frac{3}{2}\triangle u_1 + u_1^3 + 3Bu_1^2 + 3B^2u_1\right)\triangle u_1\, dx = 0.$$

Note, since $\mathcal{L}$ is self-adjoint, we could have alternatively derived the above expression by multiplying the $\mathcal{O}(m^3)$ equation by u_1, integrating over Ω, and then integrating by parts twice. Substituting in the form of u_1 leads to

$$\int_\Omega \left(-\frac{3}{2}k^2A\cos kx + A^3\cos^3 kx + 3BA^2\cos^2 kx + 3B^2A\cos kx\right)Ak^2\cos kx\, dx = 0,$$

which leads to

$$\int_\Omega 3\left(B^2 - \frac{k^2}{2}\right)\cos^2 kx + A^2\cos^4 kx + 3BA\cos^3 kx\, dx = 0. \tag{3.3.12}$$

Choosing $L = \sqrt{2}n\pi$ for $n \in \mathbb{Z}$, yields

$$3(B^2 - 1)\frac{\pi}{\sqrt{2}} + A^2\frac{3\pi}{4\sqrt{2}} = 0,$$

and so we find the amplitude A to be

$$A = 2\sqrt{1 - B^2}.$$

Thus, the ordered steady state in 1D is given by

$$u(x) \sim 2m\sqrt{1 - B^2}\cos\left(\sqrt{2}x\right), \tag{3.3.13}$$

for $|m| \ll 1$ and $B \in \mathbb{R}$.

We now wish to determine the stability of the ordered solution by applying center manifold analysis. This standard technique was applied to the Swift-Hohenberg equation by

Peletier and Williams in [24], and is easily extended to our problem. We begin by introducing a dependence on time by setting

$$u(x,t) \sim ma(t)\phi(x) + ..., \qquad \phi(x) = \sqrt{2}\cos(\sqrt{2}x), \tag{3.3.14}$$

so that one asymptotic solution of the full time-dependent PDE (2.3.17) is obtained when $a(t) = \sqrt{2(1-B^2)}$. Here, the eigenfunction $\phi(x)$ has been normalized so that

$$(\phi,\phi) := \frac{1}{L}\int_{-\frac{L}{2}}^{\frac{L}{2}} \phi(x)\phi(x)\,dx = 1.$$

We can now determine the amplitude dynamics on the center manifold $X^c = \text{span}\{\phi\}$ by projecting the full PDE evaluated at (3.3.14) onto X^c. Thus, we consider

$$\left(u_t + \frac{1}{\gamma^2}\triangle^2 u - \triangle\left(u^3 + 3Bmu^2\right) + (1-3B^2m^2)\triangle u + u, \phi\right) = 0,$$

which leads to the following ODE

$$\dot{a} = 6(1-B^2)a - 3a^3, \tag{3.3.15}$$

at the $\mathcal{O}(m^2)$ order. Hence, the amplitude $a(t)$ undergoes a supercritical pitchfork bifurcation, depicted in Figure 3.2, with the trivial fixed point being unstable, and the ordered ones $a = \pm\sqrt{2(1-B^2)}$ being stable for admissible B. Thus, the ordered state is stable for $|B| < 1$, with the trivial state being stable otherwise. This agrees with the ODT result from the previous section.

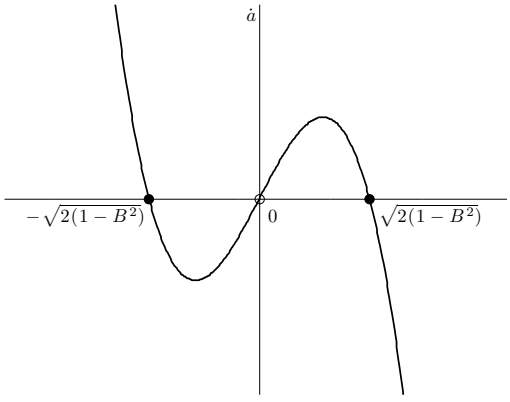

Figure 3.2: Supercritical pitchfork bifurcation diagram for $a(t)$. Stable steady states are represented by full circles, while the unstable trivial state is represented by a hollow circle.

This calculation is easily extended to the 2D case. Introducing a two-dimensional space variable (x, y), and corresponding wavenumbers (k, l), we follow the same steps to find $k^2 + l^2 = 2$ as a consequence of the leading order equation. We also find $u_1 = A_{k,l} \cos(kx + ly)$, due to periodic boundary conditions, and thus the 2D leading order solution is given by

$$u(x, y) \sim \sum_{k^2+l^2=2} mA_{k,l} \cos(kx + ly), \tag{3.3.16}$$

where $|m| \ll 1$, $B \in \mathbb{R}$, and the amplitude $A_{k,l}$ satisfies the two-dimensional version of (3.3.12),

$$\int_\Omega 3(B^2 - 1)u^2 + 3Bu^3 + u^4 \, dx \, dy = 0. \tag{3.3.17}$$

Here, $\Omega = \left[-\frac{L_x}{2}, \frac{L_x}{2}\right] \times \left[-\frac{L_y}{2}, \frac{L_y}{2}\right]$, where L_x and L_y are chosen so that Ω contains integer multiples of periods of $\cos(kx + ly)$ for all possible values of k and l. This ensures that the solution u satisfies periodic boundary conditions. In fact, it suffices to consider a finite number of k and l values in (3.3.16) due to the rotational symmetry of the solution u and periodic boundary conditions. We can thus consider the leading order behaviour of u to be defined by a sum of n terms, where $n \in \mathbb{Z}$. The condition imposed on L_x and L_y is then equivalent to requiring $kL_x = 2m\pi$ and $lL_y = 2p\pi$, for all k and l, where $m, p \in \mathbb{Z}$. Thus, the following condition

$$\frac{k_i}{k_j} \in \mathbb{Q} \qquad \text{and} \qquad \frac{l_i}{l_j} \in \mathbb{Q}, \tag{3.3.18}$$

must be satisfied for all $i, j = 1, 2, ..., n$ to ensure that u satisfies periodic boundary conditions.

A systematic way of defining the n wavenumbers is via the n^{th} roots of unity, scaled by a factor of $\sqrt{2}$. That is, $(k_j, l_j) = \sqrt{2}\, e^{i2\pi j/n}$, for $j = 1, 2, ..., n$. We recall Euler's formula

$$e^{i2\pi j/n} = \cos(2\pi j/n) + i \sin(2\pi j/n),$$

and thus write

$$k_j = \sqrt{2} \cos(2\pi j/n) \qquad \text{and} \qquad l_j = \sqrt{2} \sin(2\pi j/n). \tag{3.3.19}$$

Applying the condition (3.3.18) to the wavenumbers assuming the above defined form, we find that we only need to consider five values of n, namely $n = 1, 2, 3, 4$, and 6. Figure 3.3 shows the vectors (k_j, l_j) in these five cases.

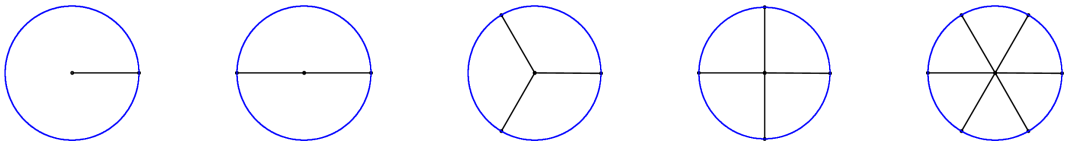

Figure 3.3: Wavenumber vectors as scaled n^{th} roots of unity for $n = 1, 2, 3, 4, 6$, from left to right. The radius of the circle is $\sqrt{2}$.

We now introduce normalized eigenfunctions

$$\phi_j(x, y) = \sqrt{2}\cos(k_j x + l_j y),$$

and note that they form an orthogonal set for any particular choice of n and $j = 1, ..., n$. Furthermore, they are even functions, so it follows that the $n = 2$ and $n = 1$ cases lead to the same one-term sum for the leading order behaviour of u. Note that $\cos(k_1 x) = \cos(k_2 x)$, where $k_1 = \sqrt{2}$ and $k_2 = -\sqrt{2}$ for $n = 2$. Similarly, the $n = 3$ and $n = 6$ cases lead to the same three-term sum for the leading order behaviour of u. Thus, the only values of n that are of interest to us are $n = 1, 4, 3$, and these lead to one-, two-, and three-term sums in (3.3.16), respectively.

We now wish to fully determine the leading order behaviour of the solution u by computing the amplitudes $A_{k,l}$ in the three above-mentioned cases, and furthermore determine the stability of the particular solutions. We could find the fixed points by solving (3.3.17), as in the 1D case. However we can determine both the steady states and their stability by immediately introducing time dependent amplitudes and considering a three term solution given by

$$u(x, y, t) \sim m\, a(t)\phi_1(x, y) + m\, b(t)\phi_2(x, y) + m\, c(t)\phi_3(x, y),$$

where

$$\begin{aligned}
\phi_1(x, y) &= \sqrt{2}\cos(\sqrt{2}x), \\
\phi_2(x, y) &= \sqrt{2}\cos(-\frac{1}{\sqrt{2}}x + \sqrt{\frac{3}{2}}y), \\
\phi_3(x, y) &= \sqrt{2}\cos(-\frac{1}{\sqrt{2}}x - \sqrt{\frac{3}{2}}y).
\end{aligned}$$

We now determine the amplitude dynamics on the center manifold $X^c = \text{span}\{\phi_1, \phi_2, \phi_3\}$ by projecting the full PDE onto X^c. Thus, we consider

$$\left(u_t + \frac{1}{\gamma^2}\triangle^2 u - \triangle\left(u^3 + 3Bmu^2\right) + (1 - 3B^2m^2)\triangle u + u, \phi_i\right) = 0,$$

for $i = 1, 2, 3$ on the domain $\left[-\frac{L_x}{2}, \frac{L_x}{2}\right] \times \left[-\frac{L_y}{2}, \frac{L_y}{2}\right]$. Here, $L_x = \frac{n\pi}{\sqrt{2}}$, and $L_y = \frac{2}{\sqrt{3}} L_x$, so that the domain contains an integer number of periods of all three terms in u. Computing the inner products and expanding in powers of m with the aid of Maple, we find the following amplitude ODE system

$$\begin{aligned} \dot{a} &= 6(1-B^2)a - 6\sqrt{2}Bbc - 6(b^2+c^2)a - 3a^3 \\ \dot{b} &= 6(1-B^2)b - 6\sqrt{2}Bac - 6(a^2+c^2)b - 3b^3 \\ \dot{c} &= 6(1-B^2)c - 6\sqrt{2}Bab - 6(a^2+b^2)c - 3c^3 \end{aligned} \tag{3.3.20}$$

where $\dot{a}$, $\dot{b}$, and $\dot{c}$ are $\mathcal{O}(m^2)$ quantities.

The original equation is a gradient system, and thus the reduced system is one as well. The corresponding Lyapunov functional is given by

$$V(a,b,c) = -3(1-B^2)(a^2+b^2+c^2) + 6\sqrt{2}Babc + 3(a^2b^2+b^2c^2+a^2c^2) + \frac{3}{4}(a^4+b^4+c^4) \tag{3.3.21}$$

The Lyapunov functional is constructed so that the following relations hold,

$$\dot{a} = -V_a(a,b,c),\ \dot{b} = -V_b(a,b,c),\ \text{and } \dot{c} = -V_c(a,b,c), \tag{3.3.22}$$

where subscripts denote partial differentiation. We thus find that $V(a,b,c)$ decreases along orbits,

$$\frac{dV}{dt} = V_a\,\dot{a} + V_b\,\dot{b} + V_c\,\dot{c} = -(V_a^2 + V_b^2 + V_c^2) \leq 0,$$

as expected. This function is in fact the projection of the nonlocal Cahn-Hilliard functional onto the center manifold X^c.

We will consider the structure and stability of the stationary solutions of the amplitude ODE system by analyzing its Lyapunov functional. The stationary states, (a_s, b_s, c_s), satisfy the following system

$$V_a(a_s,b_s,c_s) = 0,\ V_b(a_s,b_s,c_s) = 0,\ \text{and } V_c(a_s,b_s,c_s) = 0, \tag{3.3.23}$$

and in particular they are linearly stable when all the eigenvalues of the Hessian matrix, $H(V(a_s,b_s,c_s))$, are positive. To see how this is the case, consider a small perturbation around a steady state , i.e. $\mathbf{v} = \mathbf{v}_s + \delta\mathbf{v}$, where $\mathbf{v}_s = (a_s, b_s, c_s)$ and $\delta\mathbf{v} = (\delta a, \delta b, \delta c)$ with $|\delta\mathbf{v}(0)| \ll 1$. Taylor expanding (3.3.22) around this solution leads to

$$\begin{aligned} \dot{\mathbf{v}}_s + \delta\dot{\mathbf{v}} &= -J(V(\mathbf{v}_s + \delta\mathbf{v})) \\ &= -J(V(\mathbf{v}_s)) - H(V(\mathbf{v}_s)) \cdot \delta\mathbf{v} + \mathcal{O}(\delta\mathbf{v}^2), \end{aligned}$$

and thus it follows that

$$\delta\dot{\mathbf{v}} \sim -H(V(\mathbf{v}_s)) \cdot \delta\mathbf{v},$$

to leading order. Hence, the perturbation $\delta\mathbf{v}$ exponentially decays to 0 if all eigenvalues of the Hessian matrix are positive.

We identify five fixed points of the system (3.3.23) with the help of Maple. These are

1. $a = 0$, $b = 0$, $c = 0 \rightarrow$ *disorder;*
2. $a = \pm\sqrt{2(1 - B^2)}$, $b = 0$, $c = 0 \rightarrow$ *lamellae;*
3. $a = b = \pm\sqrt{\frac{2(1-B^2)}{3}}$, $c = 0 \rightarrow$ *Cartesian spots;*
4. $a = \bar{a}$, $b = c = \pm\bar{a}$, where $\bar{a} = -\frac{\sqrt{2}}{5}\left[B \pm \sqrt{5 - 4B^2}\right] \rightarrow$ *hexagonally packed circular;*
5. $a = b = \pm\bar{a}$, $c = -\bar{c}$, or $a = -b = \pm\bar{a}$, $c = \bar{c}$, where $\bar{a} = \sqrt{\frac{2(1-5B^2)}{3}}$ and $\bar{c} = 2\sqrt{2}B$ $\rightarrow |a| = b \neq c$ *case.*

Note that the form of the fixed points reflects the fact that the system (3.3.20) is invariant under the change of variables $(a, b, c) \rightarrow (a, -b, -c)$. Recalling that we could have derived these fixed points by solving (3.3.12), we check that we would indeed get the same results. Evaluating (3.3.12) at u given by the three-term sum, we find that fixed points (a, b, c) must satisfy

$$-2(1 - B^2)(a^2 + b^2 + c^2) + 6B\sqrt{2}abc + 4(a^2b^2 + b^2c^2 + a^2c^2) + (a^4 + b^4 + c^4) = 0. \quad (3.3.24)$$

Recalling the amplitude ODE system (3.3.20), we find that the above expression is equivalent to

$$\frac{1}{3}(\dot{a}a + \dot{b}b + \dot{c}c) = 0,$$

and so the fixed points of the amplitude ODE system are zeros of (3.3.24), as expected.

Figure 3.4 depicts the patterns arising from the lamellar, Cartesian spots, and hexagonally packed circular (HPC) steady states. Note that the wave vector of the lamellar state is the 1^{st} root of unity rotated by $\pi/4$. This is a viable solution since rotations of the three sets of wave vectors identified by the $n = 1, 4$, and 3 cases satisfy the condition (3.3.18).

Figure 3.5 depicts the representative patterns arising from the $|a| = b \neq c$ state. Note that this solution is the hexagonally packed circular state when $B = \frac{\sqrt{17}}{17}$, and lamellar state when $B = \frac{1}{\sqrt{5}}$.

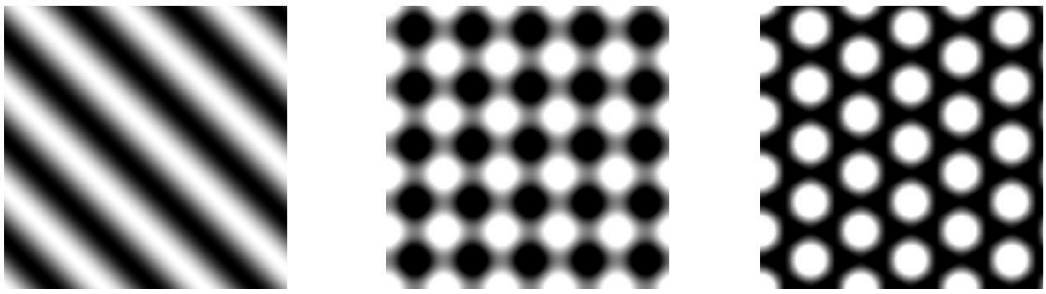

Figure 3.4: Left: lamellar state defined by $u = \cos(\frac{\sqrt{2}}{2}x + \frac{\sqrt{2}}{2}y)$. Center: Cartesian spots defined by $u = \phi_1 + \phi_2$. Right: hexagonally packed circular state defined by $u = \phi_1 + \phi_2 + \phi_3$. The color scheme used is gray scale, i.e. gray shades from black to white are represented by the values from 0 to 1.

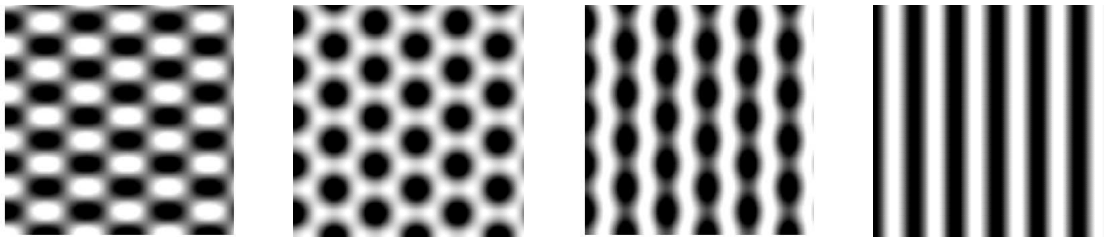

Figure 3.5: Patterns arising from the $|a| = b \neq c$ steady state. From left to right: $B = 0$, $B = \frac{\sqrt{17}}{17}$, $B = 0.4$, and $B = \frac{1}{\sqrt{5}}$.

We now proceed to examine the linear stability of the five fixed points. The Hessian of $V(a, b, c)$ is

$$H = \begin{pmatrix} 6(b^2 + c^2 + B^2 - 1) + 9a^2 & 6\sqrt{2}Bc + 12ab & 6\sqrt{2}Bb + 12ac \\ 6\sqrt{2}Bc + 12ab & 6(a^2 + c^2 + B^2 - 1) + 9b^2 & 6\sqrt{2}Ba + 12cb \\ 6\sqrt{2}Bb + 12ac & 6\sqrt{2}Ba + 12bc & 6(a^2 + c^2 + B^2 - 1) + 9c^2 \end{pmatrix},$$

and evaluation of its eigenvalues at the steady states determines the following four regions of linear stability:

1. $|B| < \frac{1}{\sqrt{5}}$: *lamellae*;
2. $\frac{\sqrt{17}}{17} < |B| < \frac{\sqrt{5}}{2}$: *hexagonally packed circular*;
3. $\frac{1}{\sqrt{5}} < |B| < \frac{5}{\sqrt{101}}$: $|a| = b \neq c$ *case*;
4. $|B| > 1$: *disorder*.

We thus find that Cartesian spots are never linearly stable since the eigenvalues of the Hessian matrix, evaluated at this steady state, are never all positive. We also find that the $|a| = b \neq c$ state is linearly stable for a small range of $|B|$ values, but it is precisely in this range that the amplitudes a and b become complex-valued, and thus no longer lead to a valid representation of the solution u. So, the only relevant linearly stable states are the lamellar, hexagonally packed circular, and constant states. Figure 3.6 shows graphically the linear stability regions for these three steady states.

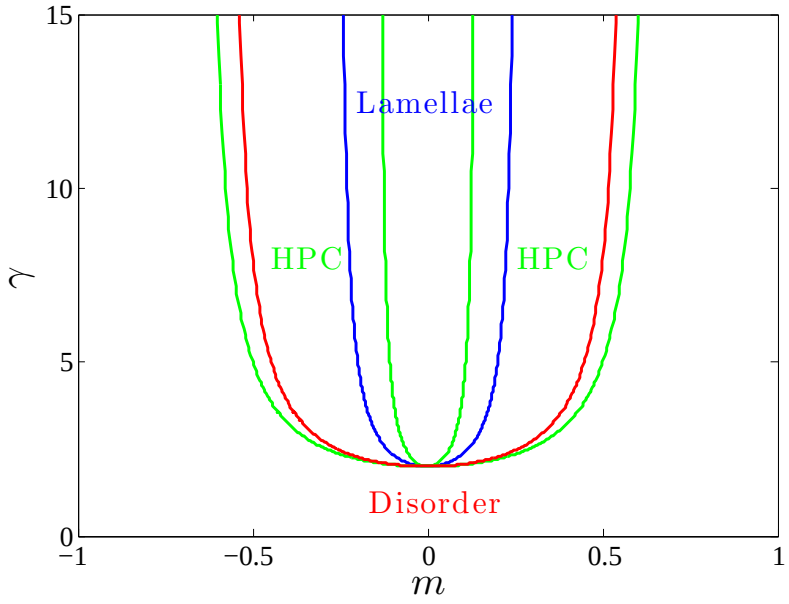

Figure 3.6: Linear stability regions for the three steady states, valid for the neighbourhood of $(m, \gamma) = (0, 2)$. These regions determine when lamellar, hexagonally packed circular, and constant states are local minimizers.

We now wish to determine the global stability of the linearly stable steady states by considering their Lyapunov energies. The following functions of B represent the evaluations of the Lyapunov functional at the constant, lamellar, and hexagonally packed circular steady states, respectively,

$$\begin{aligned} V_1 &= 0, \\ V_2 &= -3(1-B^2)^2, \\ V_3 &= -\frac{69}{125}B^4 \pm \frac{24}{25}B\sqrt{5-4B^2}\left(1-\frac{4}{5}B^2\right) + \frac{54}{25}B^2 - \frac{9}{5}. \end{aligned}$$

Figure 3.7 shows these three Lyapunov energies.

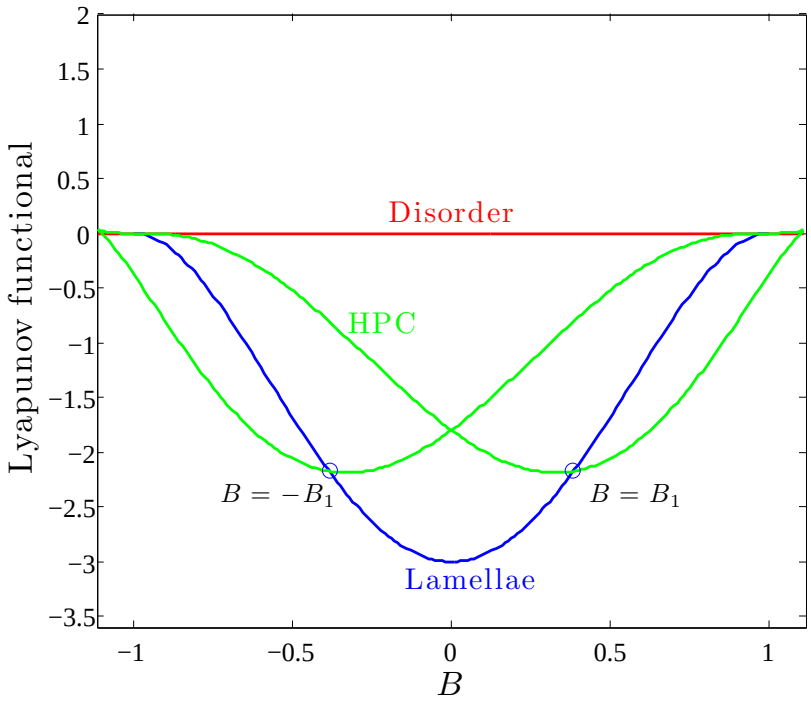

Figure 3.7: Lyapunov functional evaluated at the three linearly stable steady states.

A state which has the lowest Lyapunov energy for a particular value of B is the one which is globally stable there. Thus, we see that there is an exchange of global stability between the lamellar and hexagonal states at $|B| = B_1$, and between the hexagonal and constant states at $|B| = 1$. The value of B_1 can be found easily by equating the lamellar and hexagonal Lyapunov energies, that is, solving $V_2 = V_3$. In this way we find that $B_1 = \frac{1}{29}\sqrt{551 - 174\sqrt{6}}$, which is approximately equal to 0.39. Thus, the lamellar state is optimal for $|B| < B_1$, the hexagonally packed circular state when $B_1 < |B| < 1$, and disorder when $|B| > 1$. Figure 3.8 summarizes these results.

Recalling that B measures the distance from the ODT curve along the m axis, we summarize the linear and global stability results in terms of the function f, defined as follows,

$$f(B, m) = \frac{2}{1 - 3(\frac{m}{B})^2}.$$

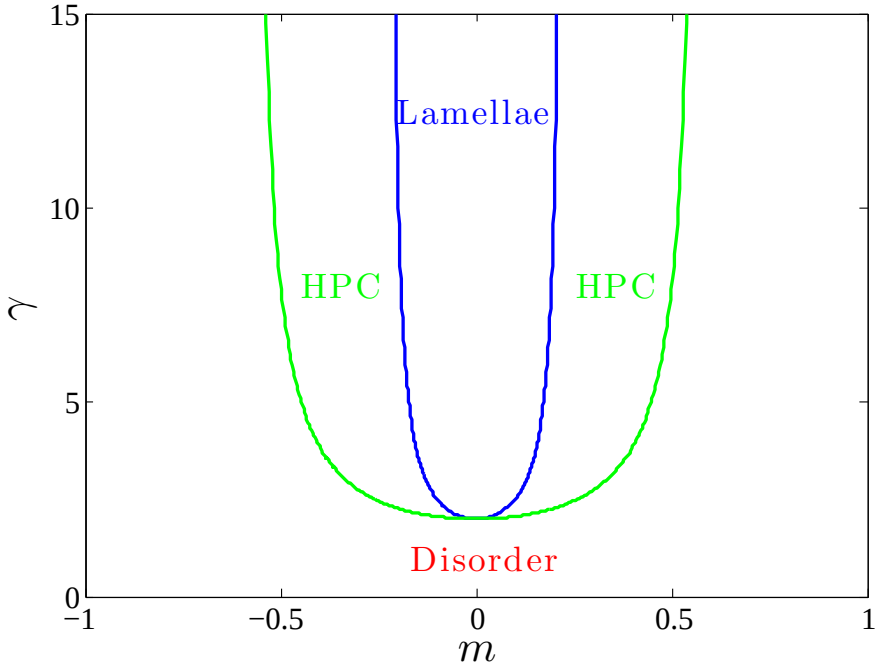

Figure 3.8: Global stability regions: the lamellar state is globally stable for $|B| < B_1$, the hexagonal state when $B_1 < |B| < 1$, and disorder when $|B| > 1$. These regions are valid in the neighbourhood of $(m, \gamma) = (0, 2)$ and determine when lamellar, hexagonally packed circular, and constant states are global minimizers.

Thus, we find the following linear stability regions

1. $|\gamma| > f\left(\frac{1}{\sqrt{5}}, m\right)$: *lamellae*;
2. $f\left(\frac{\sqrt{5}}{2}, m\right) < |\gamma| < f\left(\frac{\sqrt{17}}{17}, m\right)$: *hexagonally packed circular*;
3. $|\gamma| < f(1, m)$: *disorder*.

Likewise, the global stability regions can be written as follows

1. $|\gamma| > f\left(\frac{1}{29}\sqrt{551 - 174\sqrt{6}}, m\right)$: *lamellae*;
2. $f(1, m) < |\gamma| < f\left(\frac{1}{29}\sqrt{551 - 174\sqrt{6}}, m\right)$: *hexagonally packed circular*;
3. $|\gamma| < f(1, m)$: *disorder*.

These global stability regions determine the 2D phase diagram for the self-assembly of diblock copolymers in a small region of the (m, γ) plane, close to the point $(m, \gamma) = (0, 2)$. Figure 3.8 is thus the preliminary phase diagram, which we wish to extend to the full (m, γ) plane via numerical simulations of the model PDE. We expect the numerical phase diagram to agree with the analytical one in the neighbourhood of the point $(m, \gamma) = (0, 2)$, but our asymptotic calculations give us no guidance outside of this neighbourhood, due to their local nature.

3.4 Metastability of the Model PDE

Before we proceed to the computation of the numerical phase diagram we note that numerical simulations of the model PDE may prove to be difficult due to metastable behaviour, known to be exhibited by the Cahn-Hilliard equation. The Cahn-Hilliard equation, which differs from our model PDE only in the lack of the nonlocal term, is known to evolve over two stages characterized by different time scales. The first stage is defined by an evolution from the high energy homogeneous mixture to a pattern of internal layers, which occurs over a $\mathcal{O}(1)$ time interval [29]. This is followed by an exponentially slow, or metastable, coarsening stage during which internal layers move exponentially slowly in time until they collapse in pairs or against the end-points, eventually leading to a steady state solution. This means that a steady state can be observed only after an exponentially long in $\frac{1}{\varepsilon}$ time interval, and thus in practical computations we may not only have to wait for a very long time in order to obtain the steady state, but we may not even be able to distinguish it from metastable solutions, i.e. the solutions which change exponentially slowly in time. Figure 3.9 showcases this behaviour for the 1D Cahn-Hilliard equation.

An analytical stationary solution of the 1D Cahn-Hilliard equation

$$u_t = -\varepsilon^2 u_{xxxx} - u_{xx} + (u^3)_{xx}$$

is known to be

$$u = \tanh\left(x/\sqrt{2}\varepsilon\right).$$

Minimizers of the standard Cahn-Hilliard energy contain one period of the tanh profile, as extra periods increase the interfacial energy. However, we do not observe this steady state in practical computations due to the very slow evolution after the initial relatively quick formation of internal layers.

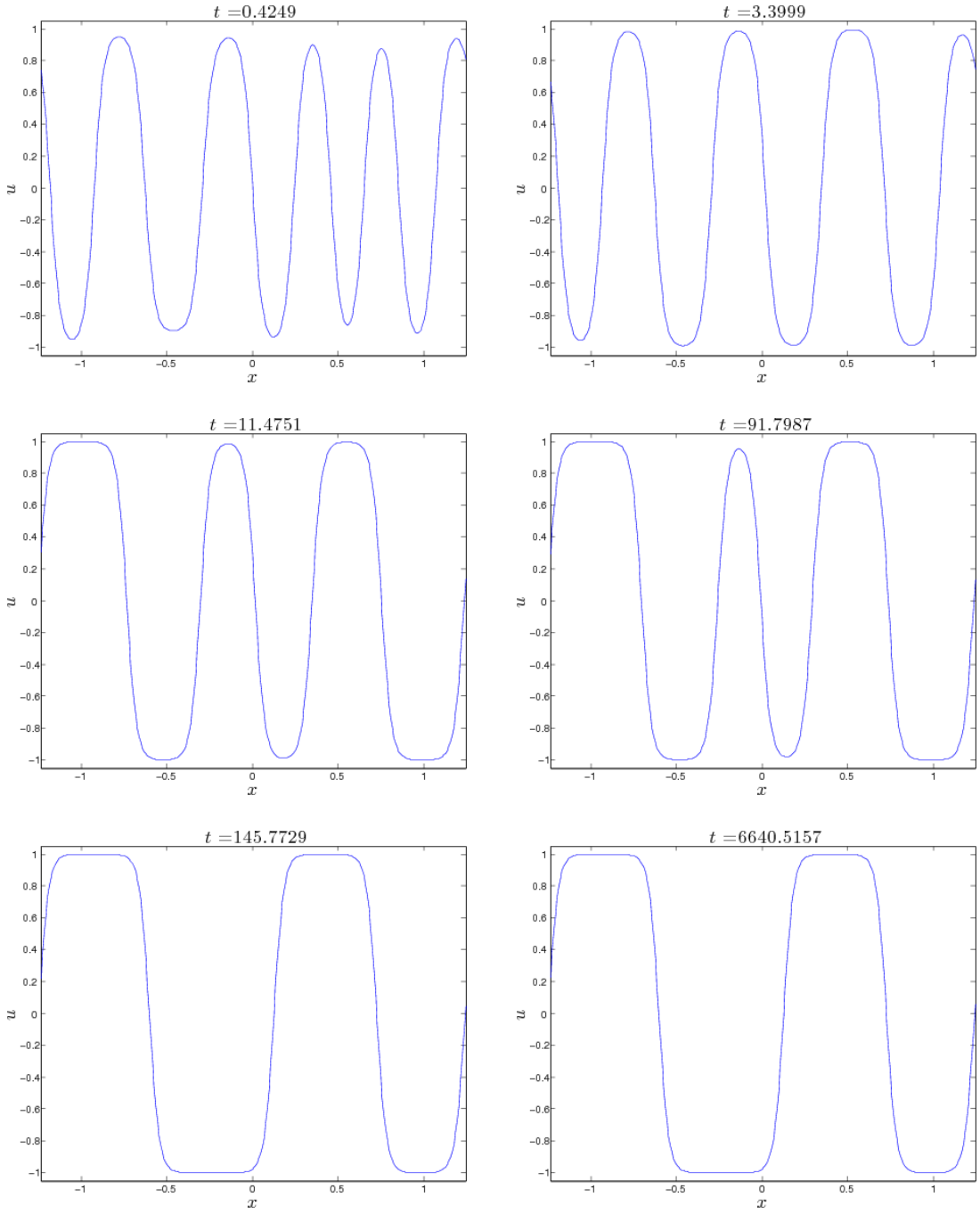

Figure 3.9: Evolution of the 1D Cahn-Hilliard equation ($\varepsilon = 0.04$, $m = 0$). The steady state is $u = \tanh(x/\sqrt{2}\varepsilon)$, but it takes an exponentially long amount of time for it to be attained. Thus, in practice we do not observe one of the two final peaks collapsing.

In addition to the well-known metastability problem associated with the Cahn-Hilliard equation, the SCFT numerical simulations were found to lead to metastable solutions [12]. Thus, it is very likely that our model PDE will poses the same undesirable behaviour.

Chapter 4

Numerical Implementation

Full description of the 2D phase diagram requires numerical simulations of the model PDE. To this end, several discretization schemes will be considered in order to find the one which approximates the steady states throughout the (m, γ) plane most accurately and efficiently. We will consider pseudospectral spatial discretizations of the exponential time differencing schemes and the unconditionally stable Eyre's scheme. These methods are known to perform well when applied to nonlinear stiff PDEs, and are thus appropriate, given that our model PDE contains both a cubic nonlinearity and a stiff bilaplacian term.

4.1 Pseudospectral Spatial Discretization

Periodic boundary conditions provide a natural setting for a Fourier pseudospectral discretization of space. This is our method of choice since computation of the Laplacian introduces no additional error if done in Fourier space, due to the fact that its eigenfunctions on a rectangular domain are the Fourier modes themselves. Furthermore, the necessary two-dimensional discrete Fourier transforms can be done in $\mathcal{O}(N^2 \log_2(N))$ operations, using the Fast Fourier Transform (FFT) algorithm, thus allowing for a fast numerical implementation.

We outline the basic idea of pseudospectral spatial discretization through a 1D example. To this end, we consider a spatial interval $[0, L]$, which has been divided into N equal sub-intervals of width $\triangle x = \frac{L}{N}$, where N is chosen to be a power of 2 in order to maximize the speed of the FFT algorithm. The spatial grid points are given by $x_j = \frac{jL}{N}$, and approximations of the solution $u(x_j, t)$ by $U_j(t)$, for $j = 0, 1, 2, ..., N-1$. The discrete Fourier

transform of $U = \{U_1, \ldots, U_N\}$, for fixed time, is defined as

$$\hat{U}_k = \mathcal{F}_k[U] = \frac{1}{N} \sum_{j=0}^{N-1} U_j \, e^{-2\pi i k x_j / L},$$

for $k = -\frac{N}{2}, ..., 0, ..., \frac{N}{2} - 1$. The inverse discrete Fourier transform can be used to recover U from $\hat{U} = \{\hat{U}_{-\frac{N}{2}}, \ldots, \hat{U}_{\frac{N}{2}-1}\}$ as follows,

$$U_j = \mathcal{F}^{-1}[\hat{U}] = \sum_{k=-\frac{N}{2}}^{\frac{N}{2}-1} \hat{U}_k \, e^{2\pi i k x_j / L},$$

for $j = 0, ..., N-1$. In the limit $N \to \infty$, this becomes the Fourier series representation of u, for fixed time t. In the finite version, it is the truncated Fourier series representation of U, given the orthonormal set of Fourier modes $\{e^{2\pi i k x_j / L}\}_{j=0}^{N-1}$. In this light, terms $\hat{U}_k$ are also referred to as the Fourier coefficients of U.

The equivalent statements in a 2D domain $[0, L]^2$ are

$$\hat{U}_{k,l} = \mathcal{F}_{k,l}[U] = \frac{1}{N^2} \sum_{j=0}^{N-1} \sum_{m=0}^{N-1} U_{j,m} \, e^{-2\pi i (k x_j + l y_m)/L}, \tag{4.1.1}$$

for $k, l = -\frac{N}{2}, ..., 0, ..., \frac{N}{2} - 1$, and

$$U_{j,m} = \mathcal{F}^{-1}[\hat{U}] = \sum_{k=-\frac{N}{2}}^{\frac{N}{2}-1} \sum_{l=-\frac{N}{2}}^{\frac{N}{2}-1} \hat{U}_{k,l} \, e^{2\pi i (k x_j + l y_m)/L}, \tag{4.1.2}$$

for $j, m = 0, ..., N-1$.

We now recall a very useful result relating a spatial derivative in real space to multiplication by a scalar in Fourier space,

$$\mathcal{F}_k \left[\frac{\partial^p U}{\partial x^p} \right] = \left(\frac{2\pi i k}{L} \right)^p \hat{U}_k.$$

Redefining $k = \frac{2\pi}{L} \left(-\frac{N}{2}, ..., 0, ..., \frac{N}{2} - 1\right)$, the above simplifies to

$$\mathcal{F}_k \left[\frac{\partial^p U}{\partial x^p} \right] \sim (ik)^p \hat{U}_k. \tag{4.1.3}$$

Having outlined the concept of the discrete Fourier transform, we are now ready to transform the model PDE into the discrete Fourier space, leading to a pseudospectral spatial

discretization. To this end we consider a particular rescaling of the version (2.2.10) of the model PDE. This version is expressed in terms of the parameters ε, σ, and m, and we additionally introduce the rescaled variable, $\tilde{u} = u - m$, so that $\fint_\Omega \tilde{u} = 0$. Dropping the tilde symbol for convenience, the PDE form of interest becomes:

$$\frac{\partial u}{\partial t} = -\varepsilon^2 \triangle^2 u - \triangle u - \sigma u + \triangle (u+m)^3. \tag{4.1.4}$$

We make this particular choice for ease of numerical implementation, as (4.1.4) contains fewer terms than the fully rescaled (2.3.17) version of the PDE. The resulting solutions u are characterized by different domain periodicities from those obtained by solving (2.3.17), but the morphology of the solution is unaffected. Thus, the particular choice of the rescaling is irrelevant to the computation of the phase diagram, and we have the freedom to choose the one which makes the numerical implementation most convenient. With this rescaling, we always consider the value of ε to be fixed, so that variations in γ translate directly into variations of σ. This results in parameters m and γ fully determining all parameters in (4.1.4).

The energy corresponding to (4.1.4) is a rescaling of the nonlocal Cahn-Hilliard functional (2.1.1):

$$E_{\varepsilon,\sigma}(u) \;=\; \frac{\varepsilon^2}{2} \int_\Omega |\nabla u|^2 \, dx \;+\; \int_\Omega \frac{1}{4}(1-u^2)^2 \, dx \;+\; \frac{\sigma}{2} \int_\Omega |\nabla v|^2 \; dx, \tag{4.1.5}$$

with $\fint_\Omega u = 0$, and v satisfying $-\triangle v = u$ with periodic boundary conditions on $\partial\Omega$.

Using (4.1.1) and (4.1.3), we transform the model PDE (4.1.4) into the discrete Fourier space and obtain the following set of N ODEs for the Fourier coefficients $\hat{U}_{\mathbf{k}}(t)$,

$$\frac{\partial \hat{U}_{\mathbf{k}}}{\partial t} = \left(-\varepsilon^2 |\mathbf{k}|^4 + |\mathbf{k}|^2 - \sigma\right) \hat{U}_{\mathbf{k}} - |\mathbf{k}|^2 \mathcal{F}_{\mathbf{k}} \left[(U+m)^3\right]. \tag{4.1.6}$$

Here, the wavevector is defined as $\mathbf{k} = (k, l)$, for $k, l = \frac{2\pi}{L}\left(-\frac{N}{2}, ..., 0, ..., \frac{N}{2} - 1\right)$. The system (4.1.6) defines a pseudospectral method, rather than a spectral one, as the nonlinearity, $(U+m)^3$, needs to be evaluated in real space and then transformed back into the discrete Fourier space at each time step. Pseudospectral methods benefit from spectral accuracy in space, whereby convergence at the rate of $\mathcal{O}(N^{-m})$ for all $m \geq 0$ is achieved for smooth functions u. More information on the properties of these methods is available in [32] and [10].

Having discretized space pseudospectrally, all we now need for a full discretization of the model PDE is a scheme for the time-dependent ODEs (4.1.6). To this end, we consider three

different time discretization methods, namely two exponential time differencing schemes and the Eyre unconditionally stable scheme.

4.2 ETDRK4 Scheme

We begin the description of the exponential time differencing Runge-Kutta order 4 (ETDRK4) discretization scheme by writing the system (4.1.6) in the following form

$$\frac{\partial \hat{U}_{\mathbf{k}}}{\partial t} = \mathbf{L}\hat{U}_{\mathbf{k}} + \mathbf{N}_{\mathbf{k}}\left(U\right). \tag{4.2.7}$$

Here, $\mathbf{L}$ and $\mathbf{N}_{\mathbf{k}}$ are the discretized linear and nonlinear operators, respectively. That is,

$$\mathbf{L} = -\varepsilon^2|\mathbf{k}|^4 + |\mathbf{k}|^2 - \sigma,$$

and

$$\mathbf{N}_{\mathbf{k}}\left(U\right) = -|\mathbf{k}|^2\mathcal{F}_{\mathbf{k}}\left[(U+m)^3\right].$$

For the higher Fourier modes, $\mathbf{L}$ is large, so a suitable time discretization scheme should be able to deal with the resulting stiffness without restricting the time steps to be of the order $1/(\varepsilon^2|\mathbf{k}|^4)$. This requirement suggests implicit implementation of the linear part, since implicit methods generally have larger stability regions and would not be computationally costly due to the diagonal nature of $\mathbf{L}$. The nonlinear part on the other hand should be implemented explicitly, as an implicit implementation would require the highly costly inversions of large non-sparse matrices at each time step.

Exponential time differencing methods fit this description and can be derived as follows. We begin by multiplying (4.2.7) by the integrating factor $e^{-\mathbf{L}t}$, and then integrate the equation over a single time step from $t = t_n$ to $t = t_{n+1} = t_n + h$, to obtain

$$\hat{U}_{\mathbf{k}}(t_{n+1}) = \hat{U}_{\mathbf{k}}(t_n)e^{\mathbf{L}h} + e^{\mathbf{L}h}\int_0^h e^{-\mathbf{L}\tau}\mathbf{N}_{\mathbf{k}}\left(U(t_n+\tau)\right)\,d\tau. \tag{4.2.8}$$

This formula is exact in time, and all variations of ETD methods stem from different approximations of the integral. In particular, the ETDRK4 method uses a 4th order Runge-Kutta formula to derive a very accurate approximation to the integral.

We denote the numerical approximations to $\hat{U}_{\mathbf{k}}(t_n)$ and $U(t_n)$ by $\hat{U}^n_{\mathbf{k}}$ and U^n, respectively, and present the ETDRK4 formulae, as derived by Cox and Matthews [7], in what

follows

$$\begin{aligned} a_{\mathbf{k}}^n &= e^{\mathbf{L}h/2}\hat{U}_{\mathbf{k}}^n + \mathbf{L}^{-1}\left(e^{\mathbf{L}h/2} - \mathbf{I}\right)\mathbf{N}_{\mathbf{k}}(U^n), \\ b_{\mathbf{k}}^n &= e^{\mathbf{L}h/2}\hat{U}_{\mathbf{k}}^n + \mathbf{L}^{-1}\left(e^{\mathbf{L}h/2} - \mathbf{I}\right)\mathbf{N}_{\mathbf{k}}(a_{\mathbf{k}}^n), \\ c_{\mathbf{k}}^n &= e^{\mathbf{L}h/2}a_{\mathbf{k}}^n + \mathbf{L}^{-1}\left(e^{\mathbf{L}h/2} - \mathbf{I}\right)\left(2\mathbf{N}_{\mathbf{k}}(b_{\mathbf{k}}^n) - \mathbf{N}_{\mathbf{k}}(U^n)\right), \\ \hat{U}_{\mathbf{k}}^{n+1} &= e^{\mathbf{L}h}\hat{U}_{\mathbf{k}}^n + \alpha_1\mathbf{N}_{\mathbf{k}}(U^n) + \alpha_2\left(\mathbf{N}_{\mathbf{k}}(a_{\mathbf{k}}^n) + \mathbf{N}_{\mathbf{k}}(b_{\mathbf{k}}^n)\right) + \alpha_3\mathbf{N}_{\mathbf{k}}(c_{\mathbf{k}}^n), \end{aligned} \tag{4.2.9}$$

where

$$\begin{aligned} \alpha_1 &= h^{-2}\mathbf{L}^{-3}\left[-4 - \mathbf{L}h + e^{\mathbf{L}h}(4 - 3\mathbf{L}h + (\mathbf{L}h)^2)\right], \\ \alpha_2 &= h^{-2}\mathbf{L}^{-3}2\left[2 + \mathbf{L}h + e^{\mathbf{L}h}(-2 + \mathbf{L}h)\right], \\ \alpha_3 &= h^{-2}\mathbf{L}^{-3}\left[-4 - 3\mathbf{L}h - (\mathbf{L}h)^2 + e\mathbf{L}h(4 - \mathbf{L}h)\right]. \end{aligned} \tag{4.2.10}$$

This is a less general form of the Cox-Matthews formulae, applicable to nonlinear operators which have no explicit dependence on time, as is the case with $\mathbf{N}_{\mathbf{k}}$.

Unfortunately, the ETDRK4 method in this form suffers from numerical instability when $\mathbf{L}$ has eigenvalues close to 0, as the exact formulae for α_1, α_2, and α_3 are inaccurate due to cancellation error. Cox and Matthews noticed this problem and resolved it by using the exact update formula for large eigenvalues, and Taylor series approximations for small eigenvalues. This resolution works for diagonal problems only, so Kassam and Trefethen [17] suggest a more generic modification of the formulae via complex contour integrals, and derive an ETDRK4 scheme which works for non-diagonal problems too. In this paper, they present a Matlab code implementing this particular variation of the ETDRK4 scheme for the Allen-Cahn equation. We modified their code to write one for the modified Cahn-Hilliard equation. In particular, we opted for the fixed time-step implementation, so that quantities $e^{\mathbf{L}h}$, $e^{\mathbf{L}h/2}$, $\mathbf{L}^{-1}\left(e^{\mathbf{L}h/2} - \mathbf{I}\right)$, α_1, α_2, and α_3 are computed once only, thus minimizing their large memory allocation cost.

4.3 ETD2 Scheme

The highly accurate Runge-Kutta order 4 method is known to generally have very good numerical stability properties, thus allowing for reasonably large stable time steps. However, this method requires four costly evaluations of a nonlinear function at each time step, thus potentially undoing the benefits of a large time step. This motivates our consideration of

a 2nd order accurate exponential time differencing scheme (ETD2), as a potentially more efficient method. The ETD2 scheme, unlike the ETDRK4, is a multi-step method, and uses the following formula to update $\hat{U}_{\mathbf{k}}$,

$$\hat{U}_{\mathbf{k}}^{n+1} = e^{\mathbf{L}h}\hat{U}_{\mathbf{k}}^{n} + \alpha_1 \mathbf{N}_{\mathbf{k}}(\hat{U}_{\mathbf{k}}^{n}) + \alpha_2 \mathbf{N}_{\mathbf{k}}(\hat{U}_{\mathbf{k}}^{n-1}), \tag{4.3.11}$$

where

$$\alpha_1 = \mathbf{L}^{-2}((1+\mathbf{L}h)e^{\mathbf{L}h} - \mathbf{I} - 2\mathbf{L}h)/h \qquad \text{and} \qquad \alpha_2 = \mathbf{L}^{-2}(-e^{\mathbf{L}h} + \mathbf{I} + \mathbf{L}h)/h. \tag{4.3.12}$$

This scheme was derived in [7] by approximating $\mathbf{N}_{\mathbf{k}}$ in the integral in (4.2.8) with its two-term Taylor expansion around $\tau = 0$. One may be skeptical that the scheme diverges when eigenvalues of $\mathbf{L}$ approach 0, but in fact the ETD2 scheme becomes the 2nd order Adams-Bashforth method in this limit. We note that the implementation of the scheme requires the evaluation of $\hat{U}_{\mathbf{k}}^{1}$ via a single-step scheme, such as the ETDRK4 for example.

The advantage of the ETD2 scheme lies in the fact that it requires only two nonlinear function evaluations per time step, and thus may be found to be faster than the ETDRK4 scheme. However, it may have more restrictive stability requirements, so numerical tests are required to determine which method is more efficient.

4.4 Eyre's Scheme

The final time discretization scheme that we consider is the unconditionally gradient stable Eyre scheme [8]. Its advantage lies in the fact that its time step is not in any way limited by stability requirements, as in the case of the exponential time differencing schemes described above. Rather, it is the desired accuracy of the temporal solution that dictates the size of the time step.

Eyre's scheme is applicable to gradient flows and thus can be used to solve the N ODEs (4.1.6). We begin the derivation of the scheme by formulating the ODE system as the following gradient flow

$$\frac{d\hat{U}_{\mathbf{k}}}{dt} = -\mathcal{F}_{\mathbf{k}}[\text{grad}\, E_{\varepsilon,\sigma}(U)], \tag{4.4.13}$$

where the continuous energy $E_{\varepsilon,\sigma}(u)$ is given by (4.1.5). The gradient is taken in the H^{-1} space, and sampled at the discrete approximation U of the solution u.

We note that the energy functional has the following three properties:

$$\begin{cases} E_{\varepsilon,\sigma}(u) \geq 0 & \forall\, u \in H^1(\mathbb{R}^2) \\ E_{\varepsilon,\sigma}(u) \to \infty & \text{as } ||u|| \to \infty \\ \langle J(\operatorname{grad} E_{\varepsilon,\sigma})(u)u, u\rangle \geq \lambda & \forall\, u \in H^1(\mathbb{R}^2). \end{cases} \tag{4.4.14}$$

Here, $J(\operatorname{grad} E_{\varepsilon,\sigma})(u)$ is the Jacobian of $\operatorname{grad} E_{\varepsilon,\sigma}(u)$, $\lambda \in \mathbb{R}$, and $< \cdot, \cdot >$ denotes the H^{-1} inner product. We note that if the functional is convex, i.e. $\lambda \geq 0$, then (4.4.13) has a unique solution and the flow is contractive. There are many unconditionally stable and uniquely solvable numerical schemes for problems of this kind. On the other hand, if $\lambda < 0$, then $E_{\varepsilon,\sigma}$ is not convex, and multiple equilibria of (4.4.13) may exist, as is the case for the nonlocal Cahn-Hilliard functional. Eyre's scheme pertains to this particular case, and its essence lies in the splitting of the functional into the difference of a contractive and an expansive functional,

$$E_{\varepsilon,\sigma}(u) = E^c_{\varepsilon,\sigma}(u) - E^e_{\varepsilon,\sigma}(u), \tag{4.4.15}$$

where $E^c_{\varepsilon,\sigma}(u)$ and $E^e_{\varepsilon,\sigma}(u)$ are strictly convex for all $u \in \mathbb{R}^2$. Note that given an appropriate splitting of the functional, the flow of the equation $\frac{d\hat{U}_{\mathbf{k}}}{dt} = -\mathcal{F}_{\mathbf{k}}[\operatorname{grad} E^c_{\varepsilon,\sigma}(U)]$ is contractive, while the flow of $\frac{d\hat{U}_{\mathbf{k}}}{dt} = \mathcal{F}_{\mathbf{k}}[\operatorname{grad} E^e_{\varepsilon,\sigma}(U)]$ is expansive.

Using the energy splitting, Eyre's scheme for (4.4.13) reads,

$$\hat{U}^{n+1}_{\mathbf{k}} = \hat{U}^n_{\mathbf{k}} + h\left(\mathcal{F}_{\mathbf{k}}[\operatorname{grad} E^e_{\varepsilon,\sigma}(U^n)] - \mathcal{F}_{\mathbf{k}}[\operatorname{grad} E^c_{\varepsilon,\sigma}(U^{n+1})]\right), \tag{4.4.16}$$

where $\hat{U}^n_{\mathbf{k}}$ approximates $\hat{U}_{\mathbf{k}}(nh)$ at time $t_n = nh$, with h being the time step as before. Thus, the expansive part of the energy is treated explicitly, and the contractive part implicitly.

If the following condition is met:

$$\left\langle J(\operatorname{grad} E^e_{\varepsilon,\sigma})(u)u, u\right\rangle \geq -\lambda, \tag{4.4.17}$$

when $\lambda < 0$, then Eyre's theorem presented in [8] asserts that for any initial condition, the numerical scheme (4.4.16) is consistent, gradient stable for all $h > 0$, and possesses a unique solution for each time step.

We note that a one-step numerical integration scheme for (4.4.13) is unconditionally gradient stable ([8]) if there exists a function $\mathcal{G}(\cdot) : \mathbb{R}^p \to \mathbb{R}$ such that, for all $h > 0$ and for all initial data:

1. $\mathcal{G}(\hat{U}_{\mathbf{k}}) \geq 0$ for all $\hat{U}_{\mathbf{k}} \in \mathbb{R}^p$,

2. $\mathcal{G}(\hat{U}_{\mathbf{k}}) \to \infty$ as $||\hat{U}_{\mathbf{k}}|| \to \infty$,

3. $\mathcal{G}(\hat{U}_{\mathbf{k}}^{n+1}) \leq \mathcal{G}(\hat{U}_{\mathbf{k}}^{n})$ for all $\hat{U}_{\mathbf{k}} \in \mathbb{R}^p$,

4. If $\mathcal{G}(\hat{U}_{\mathbf{k}}^{n}) = \mathcal{G}(\hat{U}_{\mathbf{k}}^{0})$ for all $n \geq 0$, then $\hat{U}_{\mathbf{k}}^{0}$ is a zero of $\mathcal{F}_{\mathbf{k}}[\operatorname{grad} E_{\varepsilon,\sigma}(U)]$.

Conveniently, $\mathcal{G}(\hat{U}_{\mathbf{k}}) = E_{\varepsilon,\sigma}(\hat{U}_{\mathbf{k}})$ for the Eyre scheme (4.4.16).

The Eyre scheme is at best first order accurate. Its local truncation error has the same form as the local truncation error for the forward Euler's method when $E_{\varepsilon,\sigma} = E^e_{\varepsilon,\sigma}$, and the backwards Euler's method when $E_{\varepsilon,\sigma} = E^c_{\varepsilon,\sigma}$. If $E_{\varepsilon,\sigma}$ is split into nonzero contractive and expansive parts, then the local truncation error of the Eyre scheme is larger than the local truncation errors of both Euler's methods. Consequently, the order of convergence of the local truncation error is worse than $\mathcal{O}(h)$ in this case.

We now proceed to find an appropriate splitting of $E_{\varepsilon,\sigma}$. This is generally considered to be a weakness of Eyre's method, since the splitting is not unique and depends heavily on the particular problem. It always exists, however, and in our case an appropriate splitting can be chosen to be

$$E^c_{\varepsilon,\sigma}(u) = \int_\Omega \left[\frac{\varepsilon^2}{2}|\nabla u|^2 + u^2 + \frac{1}{4} + \frac{\sigma}{2}|\nabla v|^2 \right] dx \tag{4.4.18}$$

$$E^e_{\varepsilon,\sigma}(u) = \int_\Omega \left[\frac{u^4}{4} - \frac{3u^2}{2} \right] dx. \tag{4.4.19}$$

The splitting is chosen so that a part of the bulk energy is added to the interfacial energy to create the contractive term, and the remaining part is added to the nonlocal interaction energy, to create the expansive term.

The H^{-1} gradients of the expansive and contractive parts of the energy functional can be derived using the method outlined in section 2.2.2. Discretizing the gradients in space, and then transforming into the discrete Fourier space, we obtain

$$\begin{aligned} \mathcal{F}_{\mathbf{k}}[\operatorname{grad} E^c_{\varepsilon,\sigma}(U)] &= \left(\varepsilon^2|\mathbf{k}|^4 + 2|\mathbf{k}|^2 + \sigma\right)\hat{U}_{\mathbf{k}}, \\ \mathcal{F}_{\mathbf{k}}[\operatorname{grad} E^e_{\varepsilon,\sigma}(U)] &= 3|\mathbf{k}|^2\hat{U}_{\mathbf{k}} - |\mathbf{k}|^2\mathcal{F}_{\mathbf{k}}\left[(U+m)^3\right]. \end{aligned}$$

An unconditionally gradient stable scheme for the ODE system (4.1.6) can then be chosen to be a particular implementation of Eyre's scheme (4.4.16), referred to as the linearly

stabilized splitting scheme,

$$\begin{aligned}\hat{U}_{\mathbf{k}}^{n+1} = \hat{U}_{\mathbf{k}}^{n} &+ h\left(-\varepsilon^2|\mathbf{k}|^4 - 2|\mathbf{k}|^2 - \sigma\right)\hat{U}_{\mathbf{k}}^{n+1} \\ &+ h\left(3|\mathbf{k}|^2\hat{U}_{\mathbf{k}}^{n} - |\mathbf{k}|^2\mathcal{F}_{\mathbf{k}}\left[(U^n+m)^3\right]\right). \end{aligned} \tag{4.4.20}$$

This scheme can take arbitrarily large time steps, and thus may be able to perform a fast evolution of the solution during the coarsening phase, when the solution evolves exponentially slowly.

4.5 Comparison of the Numerical Schemes

Having introduced the three schemes, we now consider their accuracy, stability, and efficiency properties, with the end goal of choosing the most suitable one for the implementation of the model PDE (4.1.4).

All three schemes are characterized by spectral accuracy in space and are differentiated by the accuracy of their time discretizations. The ETDRK4 scheme is the most accurate one of the three, with its fourth order error convergence. It is followed by the ETD2 scheme, which is a second-order scheme, and the Eyre scheme, which error convergence is worse than first order for our model PDE.

Examinations of numerical stability and efficiency are presented in the following two subsections.

4.5.1 Numerical Stability

In order to assess the performance of the three discretization schemes, when applied to the model PDE, we need to consider how restrictive their stability regions are. We define the schemes to be stable for those values of the time step h for which the solution remains bounded up to some final time T. In practice, we consider 1D Matlab implementations of the schemes and values of h going from 0.0001 in increments of 0.0001 up to the first value of h for which the solution becomes unbounded ($|U_{i,j}| > 5$ for some $1 \leq i, j \leq N$) before reaching $T = 20$. The value of h preceding this one is recorded as the largest value of h for which the solution remains bounded. We note that it suffices to consider the 1D case since stability issues are mostly influenced by the level of accuracy with which the $\mathcal{O}(\varepsilon)$ internal layers are tracked in time. These layers characterize the 1D solutions in the same way that they characterize the 2D solutions. Lamellae are simply a tanh profile in one dimension and

no variation in the other one, while the hexagonally packed circular state can be formed as a sum of 1D tanh profiles aligned along three directions, angled $\frac{2\pi}{3}$ to each other. The 1D initial conditions are chosen to be

$$U_j^0 = \sum_{n=1}^{16} a_n \cos\left(\frac{2n\pi x_j}{L}\right) + b_n \sin\left(\frac{2n\pi x_j}{L}\right), \tag{4.5.21}$$

where $j = 0, \ldots, N-1$, and the amplitudes a_n and b_n are randomly selected from the $[-1, 1]$ interval and normalized so that $|a_n + b_n| \leq 1$. These conditions model an initially well-mixed homogeneous system, which evolves into an ordered structure during quenching. A more faithful model for a homogeneous mixture would be given by truly random initial conditions, defined by a $1 \times N$ vector of values selected randomly from the $[-1, 1]$ interval. However, we do not choose these conditions for the stability study, as its Fourier transform would sometimes contain large coefficients associated with high Fourier modes, and sometimes not. That is, with the same time step h, we would sometimes observe the final solution to be bounded, and sometimes unbounded. This would make it necessary to repeat the experiment many times for the same time step in order to get meaningful results, so we opt instead for initial conditions (4.5.21), which exclude the possibility of high energy at Fourier modes greater than the 16th mode.

Figure 4.1 shows the largest h for which the one-dimensional ETDRK4 solutions with $N = 128$ remain bounded up to $T = 20$, for a selection of m and γ values. We observe that stability depends on m and γ, but a closer look at some of these results, presented in Figure 4.2, shows no simple relationship between the largest stable h and m and γ. We also notice that stability depends on the number of spatial discretization points N. Figure 4.3 shows the largest values of h for which the $N = 32$ implementation of the ETDRK4 scheme is stable. Most of the stable h values are larger than those in Figure 4.1, indicating that the scheme has a larger stability region when fewer modes are used to represent the solution. This can be justified by the fact that the linear stability of exponential time differencing schemes depends on the size of $e^{\mathbf{L}h}$ in (4.2.8). Linear stability is ensured when $|\mathbf{L}h| < 1$, that is, when $|-\varepsilon^2|\mathbf{k}|^4 + |\mathbf{k}|^2 - \sigma|h < 1$. Thus, the larger the considered modes $\mathbf{k}$, the smaller the respective time step h which ensures linear stability. However, the problem we are considering is a nonlinear one and a more careful examination of the causes behind the onset of instability would be required in order to determine their true nature.

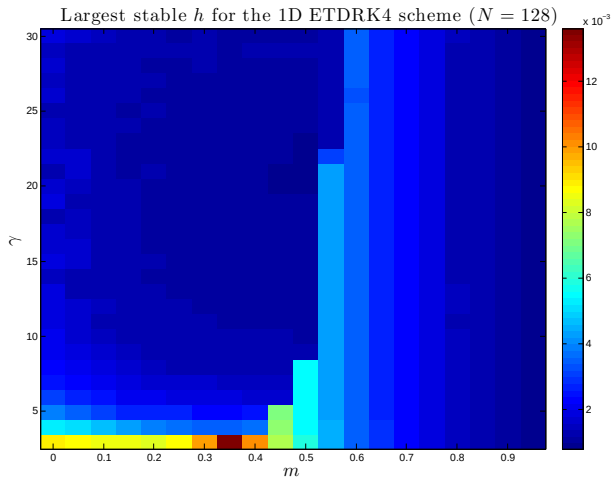

Figure 4.1: Stability region of the ETDRK4 method applied to the 1D modified Cahn-Hilliard equation with $N = 128$.

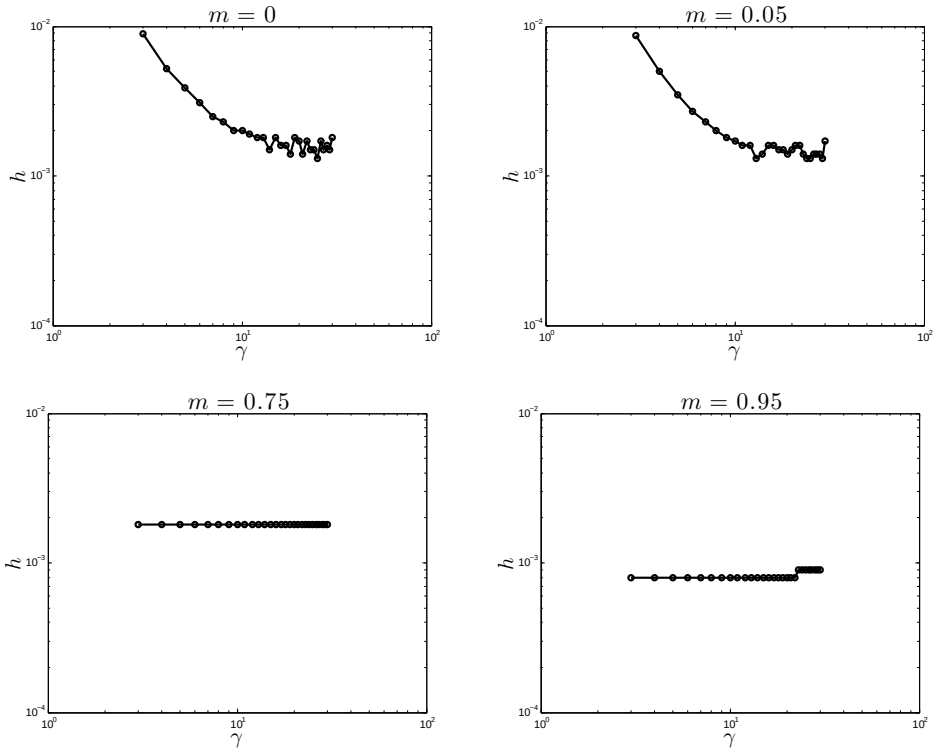

Figure 4.2: Closer look at the stability results for the 1D ETDRK4 scheme with $N = 128$. The log plots for fixed sample values of m show no simple relationships between the largest h for which the solution remains bounded and γ.

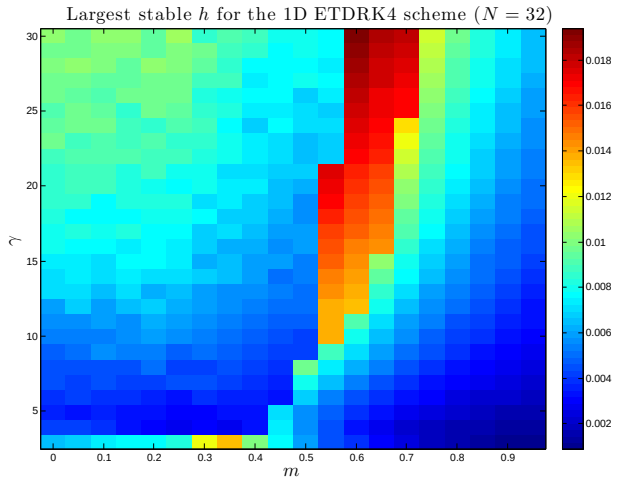

Figure 4.3: Stability region of the ETDRK4 method applied to the 1D modified Cahn-Hilliard equation with $N = 32$.

We also check that one-dimensional stability results indeed match the two-dimensional ones, by redoing the two stability diagrams presented in Figures 4.1 and 4.3, in two dimensions. These results are presented in Figure 4.4, and are found to agree well with the one-dimensional results, as expected.

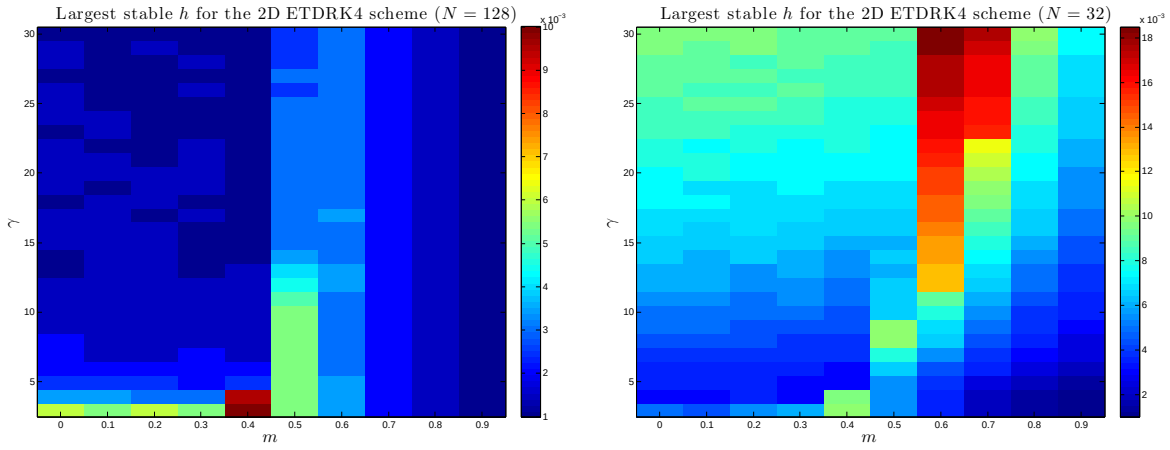

Figure 4.4: Stability region of the ETDRK4 method applied to the 2D modified Cahn-Hilliard equation. Left: $N = 128$. Right: $N = 32$.

We perform the same numerical experiments for the ETD2 scheme in 1D, and present

the results in Figures 4.5 and 4.6.

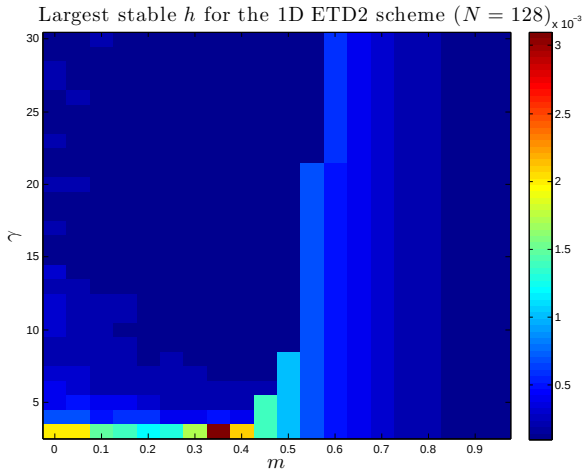

Figure 4.5: Stability region of the ETD2 method applied to the 1D modified Cahn-Hilliard equation with $N = 128$.

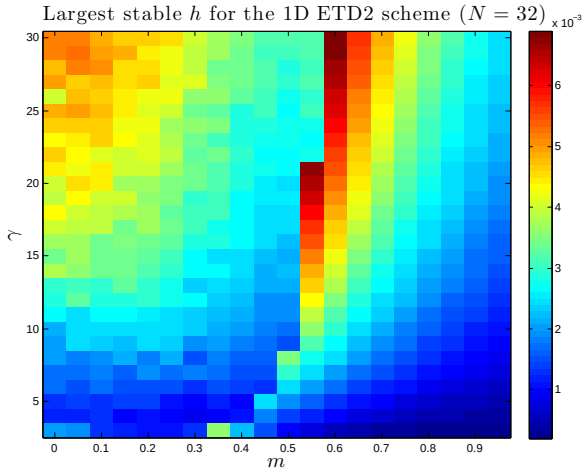

Figure 4.6: Stability region of the ETD2 method applied to the 1D modified Cahn-Hilliard equation with $N = 32$.

Yet again we observe a greater stability region when fewer modes are used to represent the solution. Furthermore, a comparison of the ETDRK4 stability results in Figure 4.1 with the ETD2 results in Figure 4.5, indicates that the ETDRK4 scheme is less restrictive. This was expected, as the Runge-Kutta order 4 scheme is known to possess a larger stability

region than the second order Adams-Bashforth scheme, which is equivalent to the ETD2 method in a certain limit. In particular, the largest stable time step for the ETDRK4 scheme is about four times larger than that corresponding to the ETD2 scheme.

Lastly, Eyre's method is found to be unconditionally stable as expected, and thus, when applied to the modified Cahn-Hilliard equation, it has the least restrictive stability properties, followed by the ETDRK4 and ETD2 methods.

4.5.2 Numerical Efficiency

Another very important aspect that needs to be considered when choosing an appropriate discretization scheme is efficiency. To this end, we conduct two numerical experiments.

The goal of the first experiment is to compare the efficiency of the three schemes by computing their execution times per iteration. The three schemes are run with $h = 0.001$ for a range of m and γ values for 3000 iterations starting from random initial conditions, i.e. an $N \times N$ matrix, which values are randomly selected from the $[-1, 1]$ interval. The time taken per iteration step is then calculated as the total time taken divided by the number of steps. The results of the study are presented in Table 4.1 and indicate that the ETD2 and Eyre schemes have comparable run times per iteration, while the run time of the ETDRK4 scheme is about 1.6 times longer. Thus, in terms of run times per iteration, Eyre's scheme is the fastest, closely followed by the ETD2, with the ETDRK4 scheme being the slowest due to the four function evaluations that it requires at each time step.

Run Time Per Iteration (s)					
ETDRK4		ETD2		Eyre	
μ	σ	μ	σ	μ	σ
0.0254	0.0177	0.0153	0.0004	0.0147	0.0071

Table 4.1: Run times per iteration. The ETDRK4, ETD2, and Eyre's schemes are run with $h = 0.001$, $m = \{0, 0.1, \ldots, 0.9\}$, $\gamma = \{3, 5, \ldots, 21\}$, and $\varepsilon = 0.04$, for 3000 iterations starting with random initial conditions. μ represents the average of all recorded run times per iteration, and σ the standard deviation.

Choosing the most efficient scheme is still premature at this point, as the three schemes have different accuracies and end up reaching a steady state at different times T. Thus, even though Eyre's scheme has the shortest run time per iteration step, it may require more steps to reach a steady state than the two ETD schemes.

To this end we conduct another experiment, with the goal of determining the final time T and the number of iteration steps n that the three schemes take to reach a stable state. The same set of lamellar initial conditions with the wrong periodicity, that is periodicity different from that of the stable state, is used to initialize the evolution of u with $(m, \gamma) = (0, 2.5)$. The time step is chosen to be $h = 2 \times 10^{-5}$ for the first set of runs, and then doubled for each consecutive run. The execution is stopped when the relative change in the solution u between two consecutive steps becomes smaller than some tolerance level, chosen to be 10^{-7}, which is small enough to indicate convergence to the lamellar steady state.

Final Time T and Number of Steps n						
	ETDRK4		ETD2		Eyre	
h	T	n	T	n	T	n
$2^1 \times 10^{-5}$	0.3943	20189	0.6264	32070	0.3393	17372
$2^2 \times 10^{-5}$	0.4092	10475	0.6264	16035	0.3514	8996
$2^3 \times 10^{-5}$	0.4241	5428	0.6264	8018	0.3683	47140
$2^4 \times 10^{-5}$	0.4389	2809	0.6264	4009	0.3947	2526
$2^5 \times 10^{-5}$	0.4541	1453	0.6266	2005	0.4409	1411
$2^6 \times 10^{-5}$	0.4694	751	0.6262	1002	0.5275	844
$2^7 \times 10^{-5}$	0.4850	388	0.6262	501	0.6962	557
$2^8 \times 10^{-5}$	0.5000	200			1.030	412
$2^9 \times 10^{-5}$	0.5200	104			1.700	340
$2^{10} \times 10^{-5}$					3.050	305
$2^{11} \times 10^{-5}$					5.740	287
$2^{12} \times 10^{-5}$					11.16	279
$2^{13} \times 10^{-5}$					21.92	274
$2^{14} \times 10^{-5}$					43.52	272
$2^{15} \times 10^{-5}$					86.72	271
$2^{16} \times 10^{-5}$					172.8	270
$2^{17} \times 10^{-5}$					345.6	270
$2^{18} \times 10^{-5}$					691.2	270

Table 4.2: Final time T and number of iterations n taken to reach a steady state given a time step h, $(m, \gamma) = (0, 2.5)$, and lamellar initial conditions with wrong periodicity. Empty fields correspond to unstable values of h for the two ETD schemes.

Table 4.2 summarizes our results. We notice that the two exponential time differencing schemes have final times T of the same order, and in particular that T varies very slowly with the increasing time step h. Eyre's scheme, on the other hand, exhibits a peculiar behaviour for larger time steps as it seems to grow linearly with h. Figure 4.7 shows the plot of $\log(T)$ vs. $\log(h)$ for Eyre's scheme, and calculation of the slope of the two relevant best fit lines indicates that $T = \mathcal{O}(h^{0.07})$ for $h \leq 2^4 \times 10^{-5}$, while $T = \mathcal{O}(h^{0.97})$ for $h \geq 2^9 \times 10^{-5}$. Thus, for a large enough time step, Eyre's scheme rescales time so that it always takes the same number of steps to reach the steady state. We conclude that this scheme would not help us march faster through time once the dynamics of the coarsening process slow down.

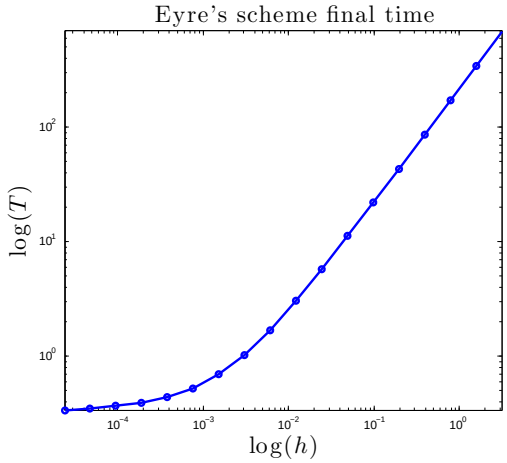

Figure 4.7: Loglog plot of the final time T that Eyre's scheme takes to converge to a steady state given a time step h. Parameter values used are $(m, \gamma) = (0, 2.5)$, and the solution u is initialized with lamellar initial conditions with the wrong periodicity. Calculation of the slope of relevant best fit lines indicates that $T = \mathcal{O}(h^{0.07})$ for $h \leq 2^4 \times 10^{-5}$, and $T = \mathcal{O}(h^{0.97})$ for $h \geq 2^9 \times 10^{-5}$.

We also notice that the three schemes seem to be converging to different final times T as the size of the time step decreases. This can be explained by the fact that they have different truncation errors, and so a single tolerance level cannot be used to decide whether all three schemes have converged. Had we appropriately chosen the stopping tolerance levels to reflect the individual truncation errors, we would have expected to observe convergence of the final times to the same value.

We now combine the results obtained from the two experiments with the goal of finding

the most efficient scheme. Choosing the smallest number of steps needed to reach a steady state from Table 4.2 and the mean run time per iteration from Table 4.1, we find that the average least amount of time taken by the three schemes to converge is: 2.64 seconds for the ETDRK4, 7.67 seconds for the ETD2, and 3.97 seconds for Eyre's scheme. Thus we find that the ETDRK4 converges the fastest, followed by the Eyre's and ETD2 schemes. These results pertain to the particular choice of $(m, \gamma) = (0.2.5)$ and the initial conditions considered in the two experiments, but there is no reason to expect that the relative order of execution times would vary significantly for other choices.

Considering the accuracy, stability, and numerical efficiency results for the three schemes, we find that the ETDRK4 scheme is the most accurate and fastest scheme, in spite of its stability region being smaller than that of Eyre's scheme. We conclude that the ETDRK4 scheme is the most appropriate scheme for the numerical implementation of the model PDE.

Chapter 5

Numerical Results

Computation of the 2D phase diagram necessitates numerical simulations of the model PDE via the ETDRK4 scheme, which was found to be the most appropriate discretization method. To this end, we compute numerical solutions throughout the (m, γ) phase space and categorize them into lamellar, hexagonally packed circular, and disordered steady states. Transition curves for both the linear and global stability exchanges are determined, thus enabling a comparison with asymptotic results close to the order-disorder transition. A numerical 2D phase diagram is proposed for the weak and intermediate segregation regimes.

5.1 Numerical Simulation Set-Up

We wish to compute the solutions of the model PDE for an extensive set of (m, γ) values, with the final goal of deriving the numerical phase diagram. Guided by the conclusions drawn in Chapter 4, we choose the ETDRK4 scheme as the most appropriate numerical approach, and implement the version (4.1.4) of the model PDE in Matlab 7.5.0 (R2007b). The domain considered is $\Omega = \left[-\frac{L}{2}, \frac{L}{2}\right]^2$, where the domain size is chosen to be

$$L = c\gamma^{2/3}, \tag{5.1.1}$$

for some fixed $c \in \mathbb{R}^+$. The γ dependent form of L is chosen so that Ω contains an approximately constant number of periods of the minimizing structure. As noted in section 2.3, the inherent period is proportional to $\left(\frac{\varepsilon}{\sigma}\right)^{1/3}$. Keeping ε constant, so that changes in $\gamma = \frac{1}{\varepsilon\sqrt{\sigma}}$ are explained purely by changes in σ, the period is found to be proportional to $\gamma^{2/3}$. Apart from ensuring that Ω contains a comparable number of periods for all γ,

(5.1.1) can be used to ensure that L is much larger than the largest scale appearing in the problem (the domain period). This is required for the validity of the assumption that L is not a bifurcation parameter, and can be achieved by appropriately choosing the value of c. The two-dimensional spatial domain Ω is described by two spatial variables, x and y, which are discretized with $N = 128$ uniformly spaced points, and the time step h is chosen small enough so that the ETDRK4 scheme is stable.

Four qualitatively different sets of initial conditions are considered. When searching for the global minimizer for a particular choice of (m, γ) values, we initialize the solution u with random initial conditions, representing the high-temperature homogeneous mixture of monomers A and B. This condition is implemented with an $N \times N$ matrix, which elements satisfy the uniform distribution on the $[-1, 1]$ interval. On the other hand, when wishing to determine the linear stability of a particular steady state, we initiate the solution u with a perturbation of the particular steady state. So for example, when checking whether the lamellar steady state is linearly stable for a particular set of (m, γ) values, we define the initial conditions as the sum of a lamellar profile, with the correct periodicity set by γ, and a uniformly distributed random matrix with elements of the order $\mathcal{O}(10^{-3})$. The correct periodicity can be ensured by using an evolved lamellar steady state for the γ value of interest. Examples of these initial conditions are presented in Figure (5.1). Note, the color scheme chosen to represent the solution is gray scale, so $u \in [-1, 1]$ is represented by gray shades from black to white.

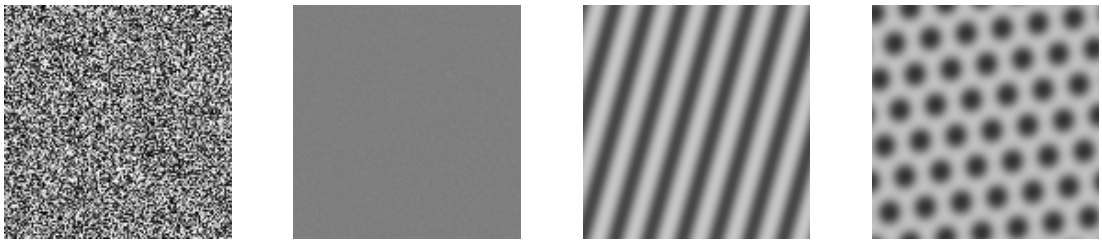

Figure 5.1: Random, perturbed constant, perturbed lamellar, and perturbed hexagonally packed circular initial conditions for $\gamma = 2.5$ and $L = \frac{\pi}{2}\gamma^{2/3}$.

The solution u is generally evolved to the final time $T = 400$. Based on experience, this final time is large enough for the solution u to converge to a steady state, as long as the particular (m, γ) point does not suffer from long term metastability. We could also choose

to stop the execution of the ETDRK4 algorithm when the relative change in u between two consecutive time steps becomes smaller than some tolerance level. However, we choose the large fixed time stopping condition instead, as this minimizes the possibility of ending the evolution prematurely at a metastable state. About 100 updates of the solution u are recorded until the final time T, and their nonlocal Cahn-Hilliard energies per unit area are computed.

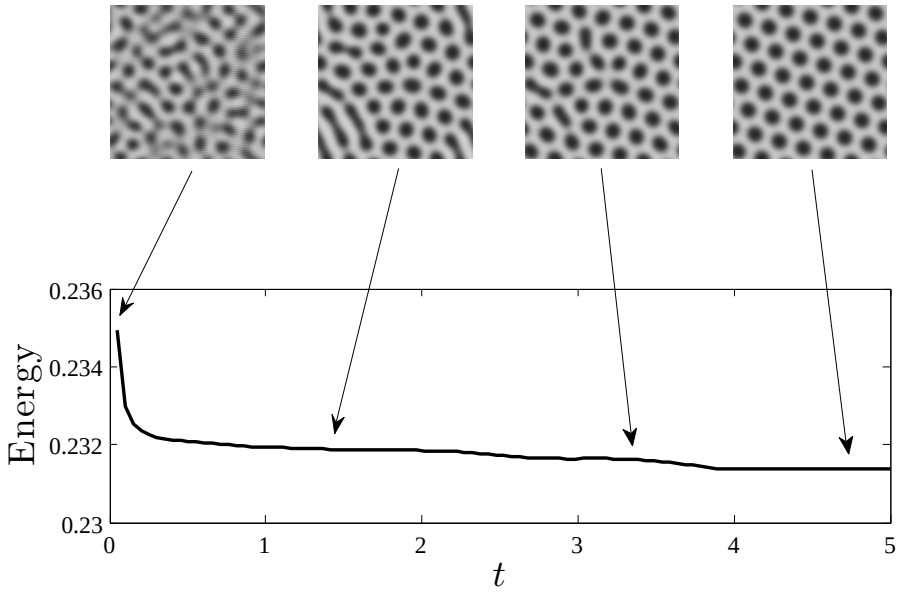

Figure 5.2: Evolution of the solution u from random initial conditions at $t = 0$ to hexagonally packed spots at $t = 5$, for $(m, \gamma) = (0.12, 2.7)$. The initial energy was $\mathcal{O}(1)$, precisely 3.2, so we show the energy decay only after $t = 0.1$ for better scale.

Figure 5.2 gives an example of the evolution of the solution u from random initial conditions to a hexagonally packed circular steady state, which is the global minimizer when $(m, \gamma) = (0.12, 2.7)$. We show the energy decay only after $t = 0.1$, as the initial energy dynamics is characterized by higher order quantities, which would skew the scale of the later dynamics. For the same choice of (m, γ) values we present in Figure 5.3 the evolution of the solution from initial lamellar conditions, with the wrong periodicity, to a lamellar steady state with the right periodicity. We note that for this particular choice of (m, γ) values we observe the hexagonally packed circular state as the global minimizer, and the lamellar state as a local minimizer, thus indicating the non-convex nature of the nonlocal Cahn-Hilliard

functional.

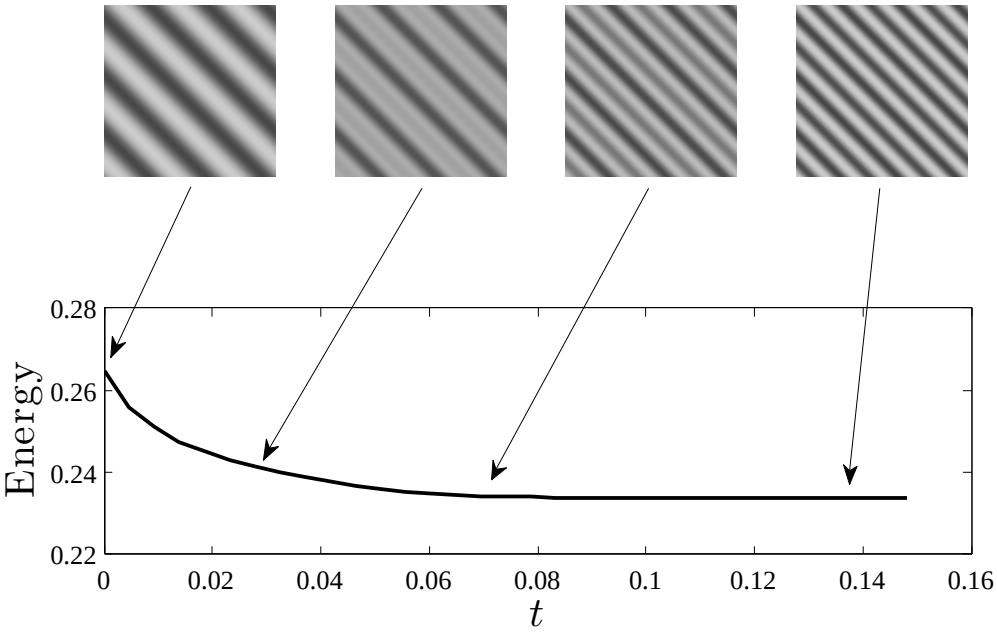

Figure 5.3: Evolution of the solution u from perturbed lamellar initial conditions with the wrong periodicity at $t = 0$ to the lamellar steady state with the right periodicity at $t = 0.15$, for $(m, \gamma) = (0.12, 2.7)$.

The nonlocal Cahn-Hilliard energy (4.1.5) per unit area of the numerical solution is calculated by computing the interfacial and nonlocal terms in Fourier space, justified by Parseval's identity

$$\frac{1}{|\Omega|}\int_\Omega |f|^2\,dx = \sum_{|\mathbf{k}|=-\infty}^{\infty} |\hat{f}_{\mathbf{k}}|^2,$$

which holds for functions $f \in L^2(\Omega)$, with Fourier coefficients

$$\hat{f}_{\mathbf{k}} = \frac{1}{|\Omega|}\int_\Omega f(x)e^{-i\mathbf{k}\cdot x}\,dx.$$

Setting $f = \nabla u$ leads to

$$\frac{\varepsilon^2}{2|\Omega|}\int_\Omega |\nabla u|^2\,dx \approx \frac{\varepsilon^2}{2}\sum_{k,l=-\pi N/L}^{\frac{2\pi}{L}(N/2-1)} \Big\{|ik\hat{U}_{\mathbf{k}}|^2 + |il\hat{U}_{\mathbf{k}}|^2\Big\},$$

as the discrete interfacial energy per unit area. Similarly, setting $f = \nabla v$ and recalling that $-\triangle v = u$, leads to

$$\frac{\sigma}{2|\Omega|}\int_\Omega |\nabla v|^2\,dx \approx \frac{\sigma}{2}\sum_{k,l=-\pi N/L}^{\frac{2\pi}{L}(N/2-1)}\left\{\left|ik\frac{\hat{U}_{\mathbf{k}}}{k^2+l^2}\right|^2+\left|il\frac{\hat{U}_{\mathbf{k}}}{k^2+l^2}\right|^2\right\},$$

as the discrete nonlocal interaction energy per unit area. We ensure no divisions by zero in the above calculation by setting the zero-th mode Fourier coefficient $\hat{U}_{\mathbf{0}}$ to 0, and setting the $(k,l) = (0,0)$ mode in the denominator to $(k,l) = (1,1)$. Note that $\hat{U}_{\mathbf{0}}$ is always supposed to equal the average of u, that is 0, so by setting $\hat{U}_{\mathbf{0}} = 0$, we also ensure that this coefficient is free of numerical error.

The bulk energy per unit area, $\frac{1}{|\Omega|}\int_\Omega \frac{1}{4}(1-u^2)^2\,dx$, is computed in real space by approximating the integral with the first order accurate trapezoidal rule.

The model PDE is a gradient flow, so we expect the discrete energy of the computed solution to be a decreasing function of time. Indeed, this is the case in our numerical simulations. In particular, in Figure 5.2 we observe an initial sharp drop in the energy from 3.2 at $t = 0$ to 0.235 at $t = 0.1$. This sharp initial decay is caused by the minimization of the large bulk energy term, and is followed by a relatively slower decrease in the energy, until a steady state is reached. On the other hand, in Figure 5.3 we observe no sharp initial drop in the energy, as the bulk energy of the initial lamellar state is not large like in the case of random initial conditions previously. The evolution to the lamellar state with the right periodicity is instead characterized by a gradual decrease of the energy.

5.2 Numerical Observations

We observe that the numerical steady states exhibit increasingly larger structures for increasing values of γ. This comes as no surprise, as the domain length of patterns scales like $\left(\frac{\varepsilon}{\sigma}\right)^{1/3}$, which is equivalent to $\gamma^{2/3}$ if we regard ε to be a fixed quantity. In particular, given for example $\gamma_1 = 2.1$, we can determine the value of γ, let's call it γ_2, for which the domain length of the patterns should be double of that corresponding to γ_1. Recalling (5.1.1), we easily find that γ_2 must satisfy $\gamma_2 = \gamma_1 2^{3/2}$, which for $\gamma_1 = 2.1$ yields $\gamma_2 = 5.9397$. Figures 5.4 and 5.5 portray solutions for these two values of γ, starting with initial perturbed lamellar and hexagonally packed circular conditions, respectively.

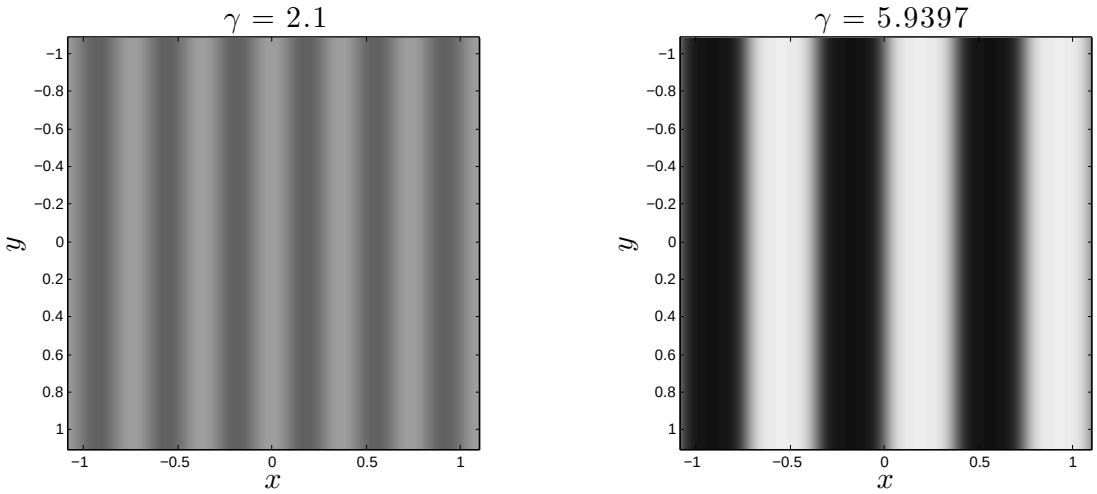

Figure 5.4: Starting with initial perturbed lamellar conditions, with $m = 0$ and fixed L, we observe the periodicity decreasing by a factor of 2 in going from the $\gamma = 2.1$ steady state, to the $\gamma = 5.9397$ steady state. The picture on the left contains six periods, while the one on the right contains three.

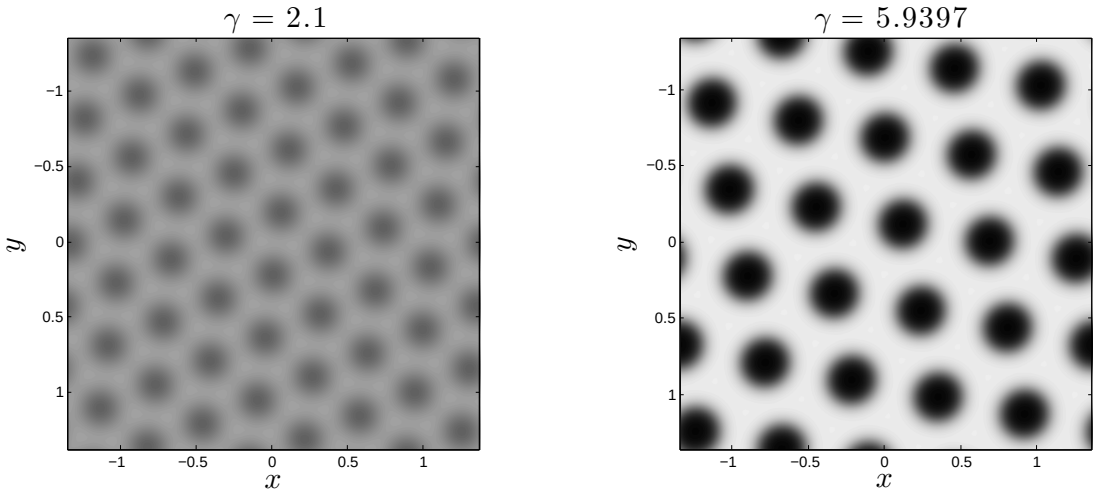

Figure 5.5: Starting with initial perturbed hexagonally packed circular conditions, with $m = 0.1$ (left), $m = 0.35$ (right), and fixed L, we observe the periodicity decreasing by a factor of 2 in going from the $\gamma = 2.1$ steady state, to the $\gamma = 5.9397$ steady state. The picture on the left contains about four periods, while the one on the right contains two.

5.2.1 Metastability

For values of γ smaller than about 3, we always observe the lamellar, hexagonally packed circular, and constant states as the final solutions. The lamellar state, obtained from random initial conditions, sometimes has little defects in the form of its profile not being straight. However, this can often be remedied by running the algorithm for a longer time, or initializing it with a different set of random initial conditions.

As γ increases above the value of 3 we start to observe states which look irregular, and in particular cannot be classified as either of the three above-mentioned phases. We refer to them as metastable states, that is states which change exponentially slowly in time. Numerically, one cannot distinguish a metastable state from a stable one, since they are both identified as solutions for which the relative change in u is smaller than some tolerance level. Furthermore, irregular long lasting states are common in diblock copolymer experiments ([12]), so it is unclear whether they may actually be steady states, rather than just intermediate profiles.

Analytical considerations can provide insight into the classification of observed profiles into the metastable and stable steady states. In the context of the mathematical model, which we use to describe the equilibrium behaviour of diblock copolymers, very irregular profiles are not expected to be the global minimizers. The nature of the nonlocal Cahn-Hilliard functional indicates that its minimizers are periodic profiles with nearly constant mean curvature surfaces separating the A- and B-rich domains. The irregular states that we observe do not match this description, and thus we term them as metastable states. One can think of these as solutions evolving from inflexion points of the functional in directions along which the first variational derivative of the functional is small. This undesired behaviour was anticipated due to the analytically proven metastability of the Cahn-Hilliard equation, as noted in section 3.4, and the metastability observed in the SCFT numerical calculations, as mentioned in section 2.2. Given that our model PDE differs from the Cahn-Hilliard equation only in the extra nonlocal term, and was directly derived from the SCFT theory, there is little reason to believe that it can escape the issue of metastability.

We find that metastability arises only when we choose random initial conditions or hexagonally packed circular conditions with the wrong periodicity. Furthermore, we find that it is most pronounced in the region of the (m, γ) plane where the lamellar state is expected to be the global minimizer. The problem worsens as γ increases as we observe increasingly

irregular metastable states. Figure 5.6 gives examples of some of these metastable patterns.

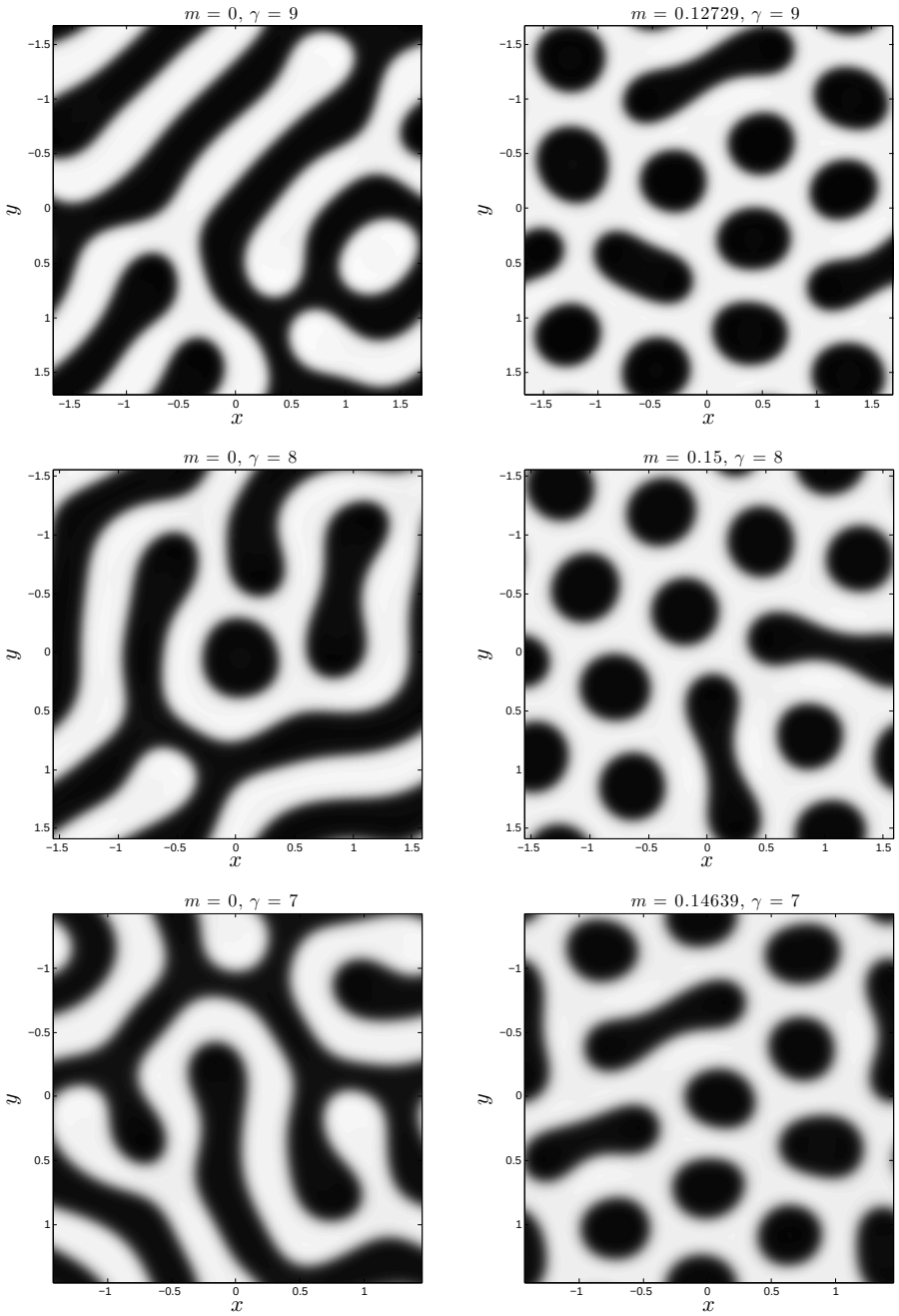

Figure 5.6: Metastable states for increasing γ values.

It is expected that the global minimizer of the nonlocal Cahn-Hilliard energy for $m = 0$ is the lamellar state above the order-disorder transition, though no proof exists as of yet. However, the three profiles presented in the left column of Figure 5.6 cannot be classified as the lamellar state, in spite of the fact that they are the evolved states of symmetric diblock copolymers for $\gamma = 7, 8$ and 9. In the right column, we observe three steady states obtained for nonzero values of m and the same values of γ. They look like intermediate states between the lamellar and hexagonally packed circular phases, and can be interpreted as indicators of the diffused transition between these two steady states.

A few different techniques were tested with the aim of ameliorating metastability and evolving the numerical solution to a steady state. The first technique consists in decreasing the value of γ once a metastable state is reached, evolving the solution for some time, and then setting γ back to its original value. Decreasing the value of γ mimics an increase in temperature, which causes metastable patterns to break up as the characteristic domain length decreases. Setting the value of γ back to the original one, may then lead to an evolution of the solution to a global minimizer of the energy, or a different local minimizer. This technique was found to sometimes decrease the amount of defects in the final state, but does not present a reliable way of ameliorating metastability.

A more systematic approach may instead be provided by gradually increasing γ from a low value, corresponding to a high-energy well mixed state, to the particular value at which we expect to observe an ordered steady state. This technique mimics the annealing process, which is used in experiments in order to synthesize diblock copolymers with regular self-assembly structures. It has been applied in SCFT numerical experiments and found to significantly reduce defects ([12]). However, it is not clear to us whether these SCFT experiments use this technique in combination with random initial conditions, or conditions with an imposed symmetry, as is almost always the case in their calculations. A more exhaustive examination of this technique applied to our model PDE is required before we can make any conclusive remarks about how well it performs.

We note that the above-mentioned technique belongs to the broad class of statistical methods, called simulated annealing, which were created with the particular purpose of navigating through a complex energy landscape in search of the global minimizer. A very simple form of simulated annealing can be achieved by adding unbiased noise to the evolved metastable state. This may force the solution out of the local minimizer that it is stuck in and make it continue its evolution through the energy landscape. However, this approach

does not provide a systematic way of addressing metastability, as too much noise leads to the divergence of the solution, and even when the solution remains bounded, there is no way of ensuring that it will not revisit the local minimizers that it was stuck in before.

A different approach to the removal of defects is provided by the technique of spectral filtering. The essence of this method lies in the removal of insignificant spectral components from an evolved state. That is, we let the self-assembling process evolve from random initial conditions until a structure is formed, compute the Fourier coefficients of the solution, and keep only the modes which correspond to the coefficients above a certain threshold. The evolution is then continued and the process of spectral filtering repeated. This approach was suggested in [12], and applied to our model PDE. It was found to remove defects in some cases, but it is not considered to be a systematic approach in this particular form. The choice of the threshold value may lead to the removal of significant information, and bias the final steady state towards a solution that may not even be a global minimizer. So this approach cannot be used for the derivation of the phase diagram, which relies on the absence of any bias towards a state that is not the global energy minimizer.

Given that we found no systematic way of resolving the problem of metastability, all of the numerical results that we present here are obtained without the use of the above-described techniques.

5.3 Classification of Steady States

In order to derive the numerical linear and global stability diagrams for the phase separation of diblock copolymers, we need to identify the phase of every computed solution. Since the only observed numerical steady states are the lamellar, hexagonally packed circular, and the constant state, this amounts to automatically assigning one of these three states to the evolved solutions.

The constant state is easily identified by calculating the difference between the maximum and minimum values of the computed solution u. When this difference is smaller than some tolerance level, chosen to be 10^{-3}, then the solution is classified as the constant state.

The remaining solutions are classified into the lamellar and hexagonally packed circular states as follows. The Fourier decomposition of the solution is computed, and the six coefficients with greatest absolute value identified. The angles between the closest pairs of corresponding wavenumbers are then calculated. Figure 5.7 shows a sketch of the typical

orientation of these wavenumbers for the lamellar phase on the left and hexagonally packed circular phase on the right. Since the lamellar state is a superposition of modes with the wavenumbers aligned in the same direction, we expect the angle between each closest pair to be approximately either 180° or 0° if the solution is a lamellar phase. The hexagonally packed circular state, on the other hand, is a sum of modes which wavenumbers are angled 60° to each other, and so the angle between closest pairs should be approximately 60° if the solution is a hexagonally packed circular state. The mean value of all six angles can be calculated (this is 60° of course), and the standard deviation determined. The standard deviation for 'perfect' lamellar and hexagonally packed circular states would be $\sim 93°$ and 0°, respectively. This motivates a classification method, which assigns the lamellar phase to a solution for which the standard deviation is greater than 45°, and the hexagonally packed circular state when the standard deviation is smaller than 35°. The states with standard deviations between these two values remain unclassified, indicating a metastable state. This classification method was found to categorize solutions into appropriate steady states very well.

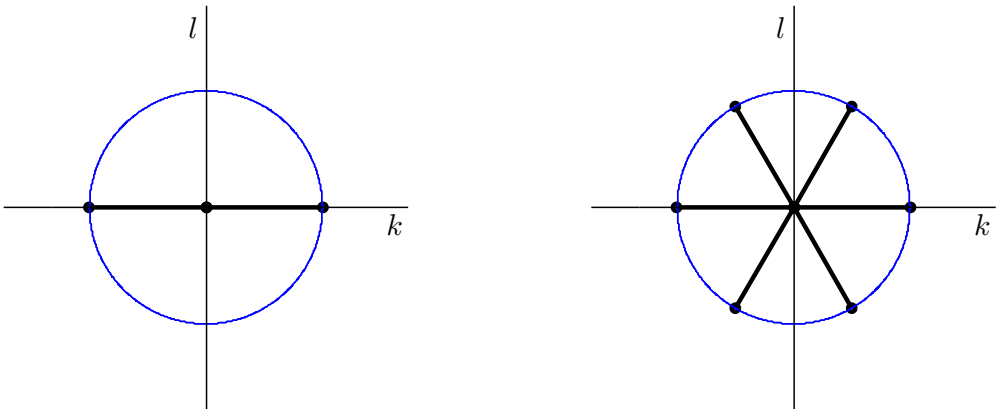

Figure 5.7: Sketch of the direction of wavevectors corresponding to the greatest Fourier coefficients of the lamellar phase on the left, and hexagonally packed circular phase on the right.

5.4 Numerical Linear Stability Results

In Chapter 3 we used asymptotic analysis to determine linear stability regions for the three steady states close to the order-disorder transition. Here, we present the corresponding results obtained via numerical simulations of the model PDE.

Three sets of solutions are computed with perturbed constant, lamellar, and hexagonally packed initial conditions with the right periodicity. The final solutions are classified into the three categories, and points (m, γ) in the phase plane are marked as belonging to the linear stability region of a particular state if the perturbed initial conditions converge to the initial conditions themselves. Figures 5.8, 5.9, and 5.10 summarize our findings. The lamellar state is marked blue, the hexagonally packed circular state (HPC) green, and the constant state is marked red. Linear stability regions for the steady states are determined by fitting a second or fourth order polynomial through the critical (m, γ) points, in the least squares sense. The critical phase points are determined by $m = (m_1 + m_2)/2$, where (m_1, γ) is categorized as a linearly stable point, and (m_2, γ) as a linearly unstable point.

The boundary of the numerical linear stability region for the lamellar steady state is found to be

$$\gamma(m) \approx -671m^4 + 113m^3 + 29m^2 - m + 2. \tag{5.4.2}$$

It contains an inflexion point, which is an artifact of the approximation of the numerical transition curve with a fourth order polynomial. Likewise, the hexagonally packed circular steady state is found to be linearly stable in the region approximately outlined by

$$\gamma(m) \approx 139m^2 + 2, \tag{5.4.3}$$

and

$$\gamma(m) \approx 27m^4 - 12m^3 + 7m^2 + 2. \tag{5.4.4}$$

Lastly, the boundary of the linear stability region for the constant phase is approximated by

$$\gamma(m) \approx 56m^4 - 16m^3 + 8m^2 + 2. \tag{5.4.5}$$

The coefficients in the best fit polynomials are rounded up, so they do not contain decimal digits. We find that the best fit polynomials approximate the numerically observed linear stability regions well, with the exception of the numerical transition between the linearly stable hexagonally packed circular state turning into lamellae for decreasing m in

Figure 5.9. Here, a higher order polynomial would seem to be more appropriate, but the ones that were fitted contained too many sharp turns, and were discarded as better than the fourth order polynomial.

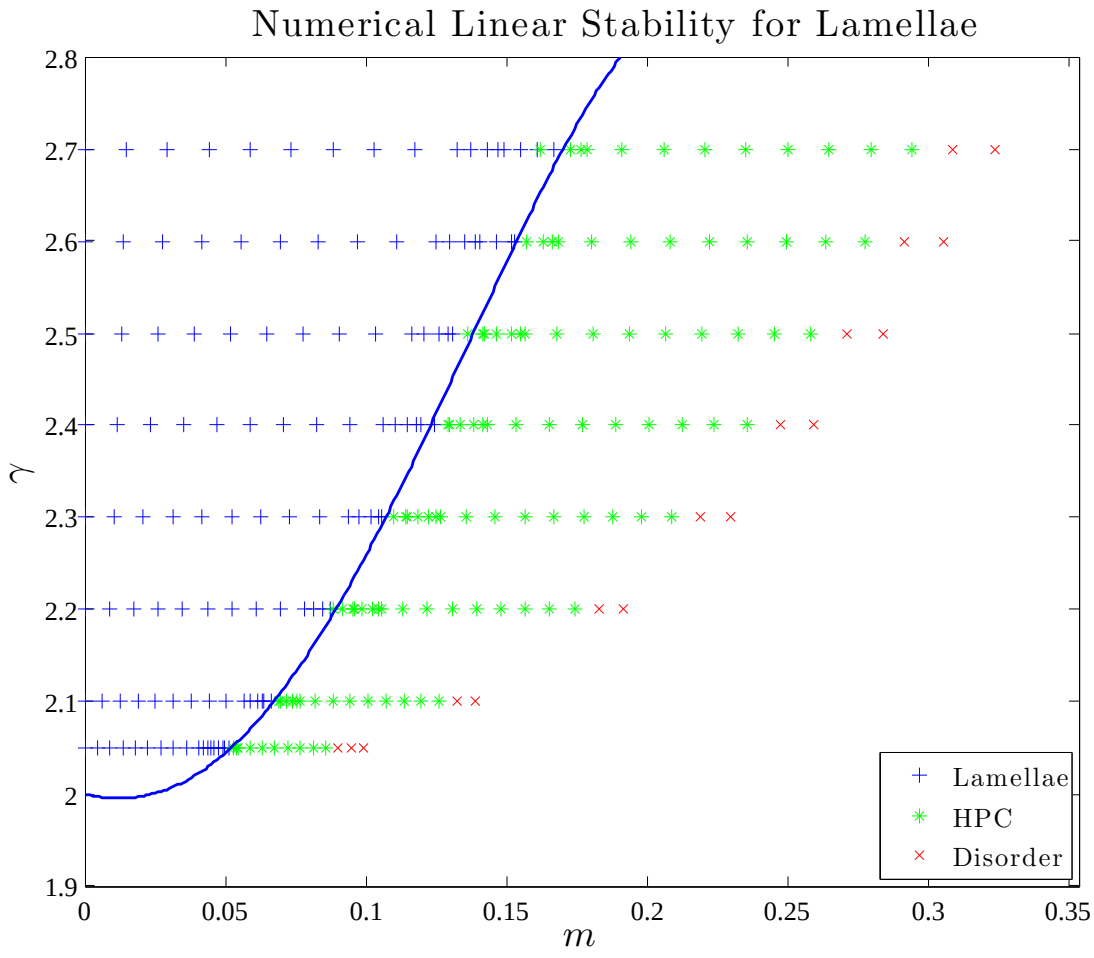

Figure 5.8: Numerical linear stability diagram for the lamellar state. The blue line defines the boundary of the linearly stable region, and is computed as the following best fit 4th order polynomial: $\gamma(m) \approx -671m^4 + 113m^3 + 29m^2 - m + 2$.

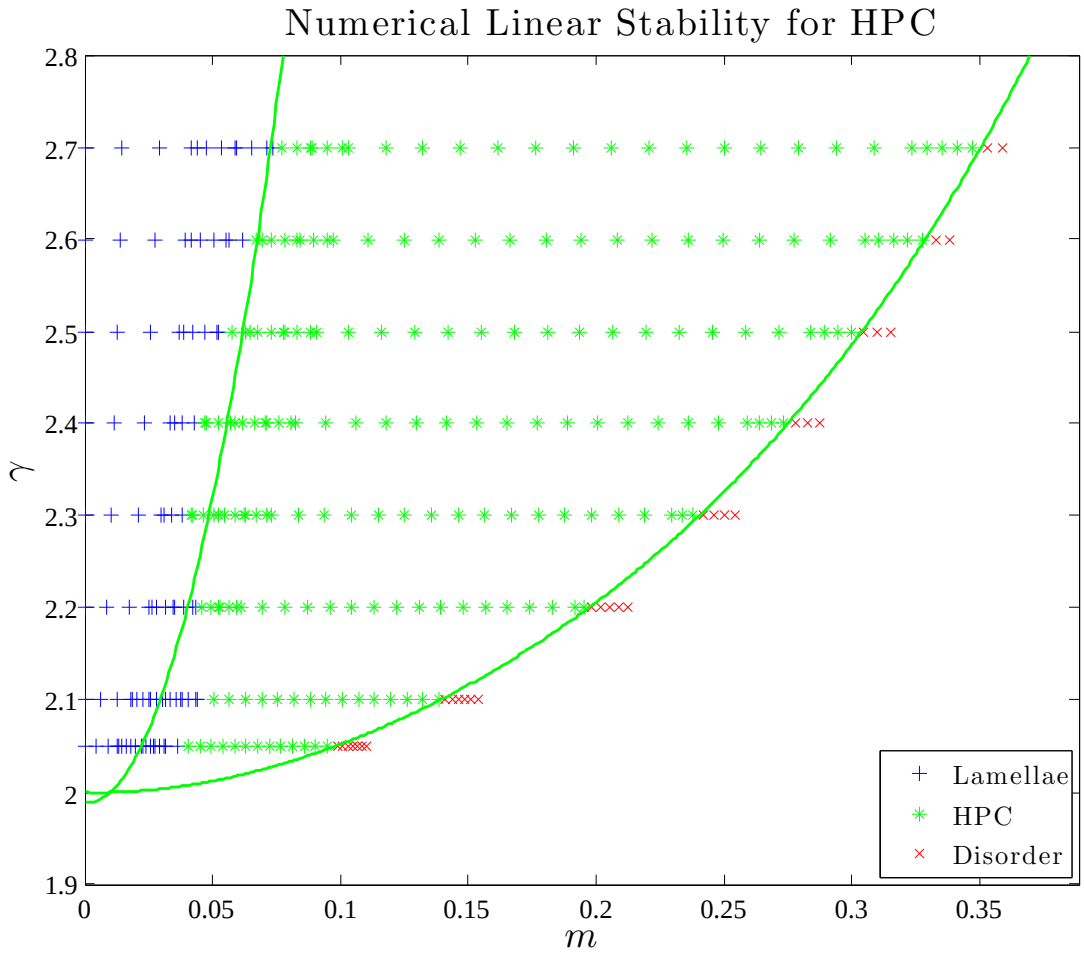

Figure 5.9: Numerical linear stability diagram for the hexagonally packed circular state. The green lines define the boundaries of the linearly stable region, and are computed as the following best fit 2nd order polynomial: $\gamma(m) \approx 139m^2 + 2$ as the linear transition between the HPC state and lamellae, and the best fit 4th order polynomial: $\gamma(m) \approx 27m^4 - 12m^3 + 7m^2 + 2$ as the linear transition between the HPC state and disorder.

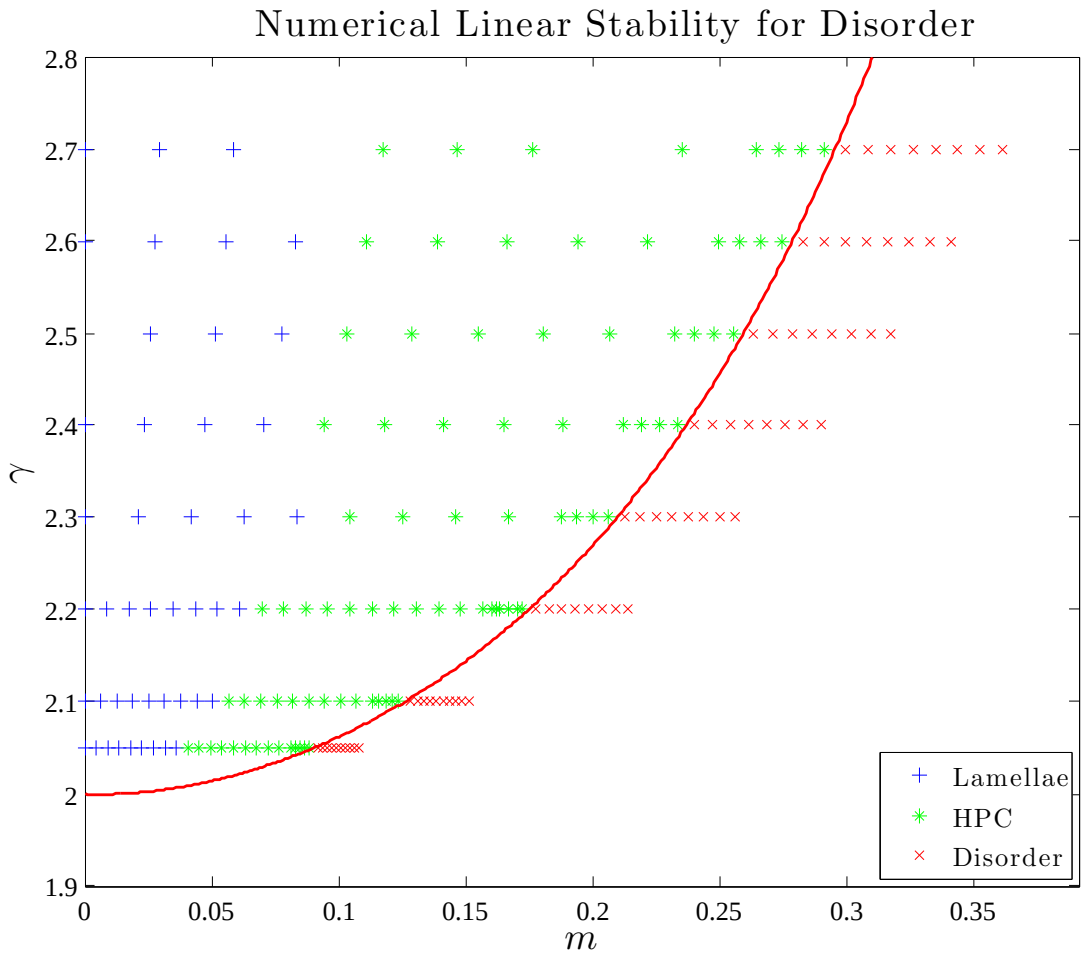

Figure 5.10: Numerical linear stability diagram for the constant steady state. It is linearly stable to the right of the red line, which is approximated as the following best fit 4th order polynomial: $\gamma(m) \approx 56m^4 - 16m^3 + 8m^2 + 2$.

5.5 Numerical Phase Diagram

We are now ready to compute the two-dimensional numerical phase diagram for the self-assembly of diblock copolymers. Random initial conditions are evolved via the ETDRK4 scheme implementing the (4.1.4) version of the model PDE. Figure 5.11 presents some of the resulting numerical solutions for a range of m and γ values.

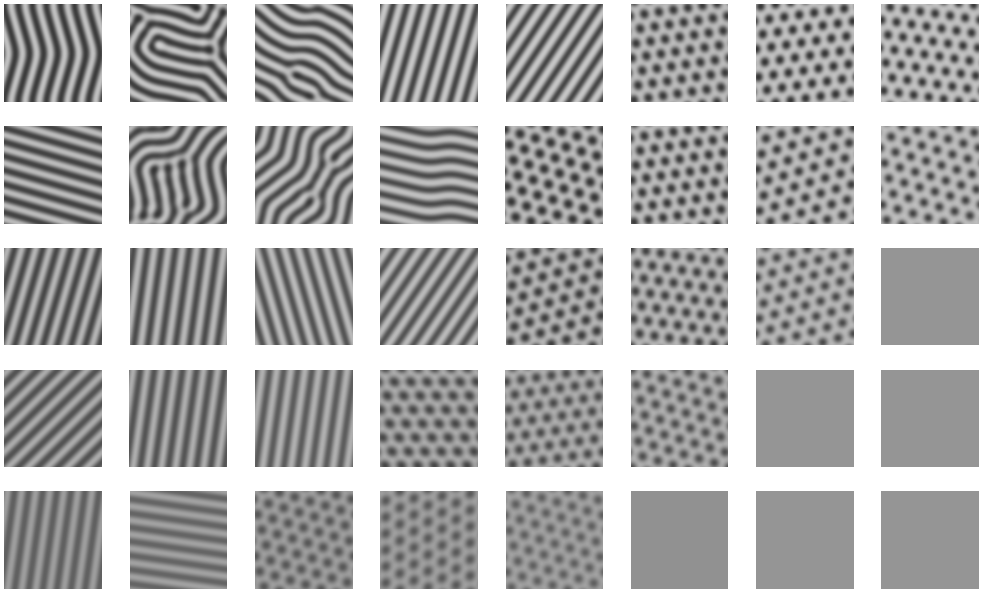

Figure 5.11: Globally stable steady states u in a domain of length $L = \frac{\pi}{2}\gamma^{2/3}$. Rows from bottom to top correspond to $\gamma = 2.1, 2.2, 2.3, 2.4, 2.5$, while the columns from left to right correspond to $m = 0.0, 0.04, 0.06, 0.08, 0.10, 0.13, 0.18, 0.21$.

Following the same methodology as the one used to derive the linear stability diagrams, we derive the two-dimensional numerical phase diagram, and present it in Figure 5.12.

The phase transition curve between the lamellar and hexagonally packed circular state is approximated by:

$$\gamma(m) \approx 50m^2 - m + 2, \tag{5.5.6}$$

for $\gamma < 2.2$, and

$$\gamma(m) \approx 60m^2 - 2m + 1.7, \tag{5.5.7}$$

for $\gamma > 2.2$, as this leads to a closer fit than when using a single second order polynomial

approximation.

The phase transition between the hexagonally packed circular state and the constant state is approximated by:

$$\gamma(m) \approx -93m^4 + 68m^3 - 8m^2 + m + 2. \tag{5.5.8}$$

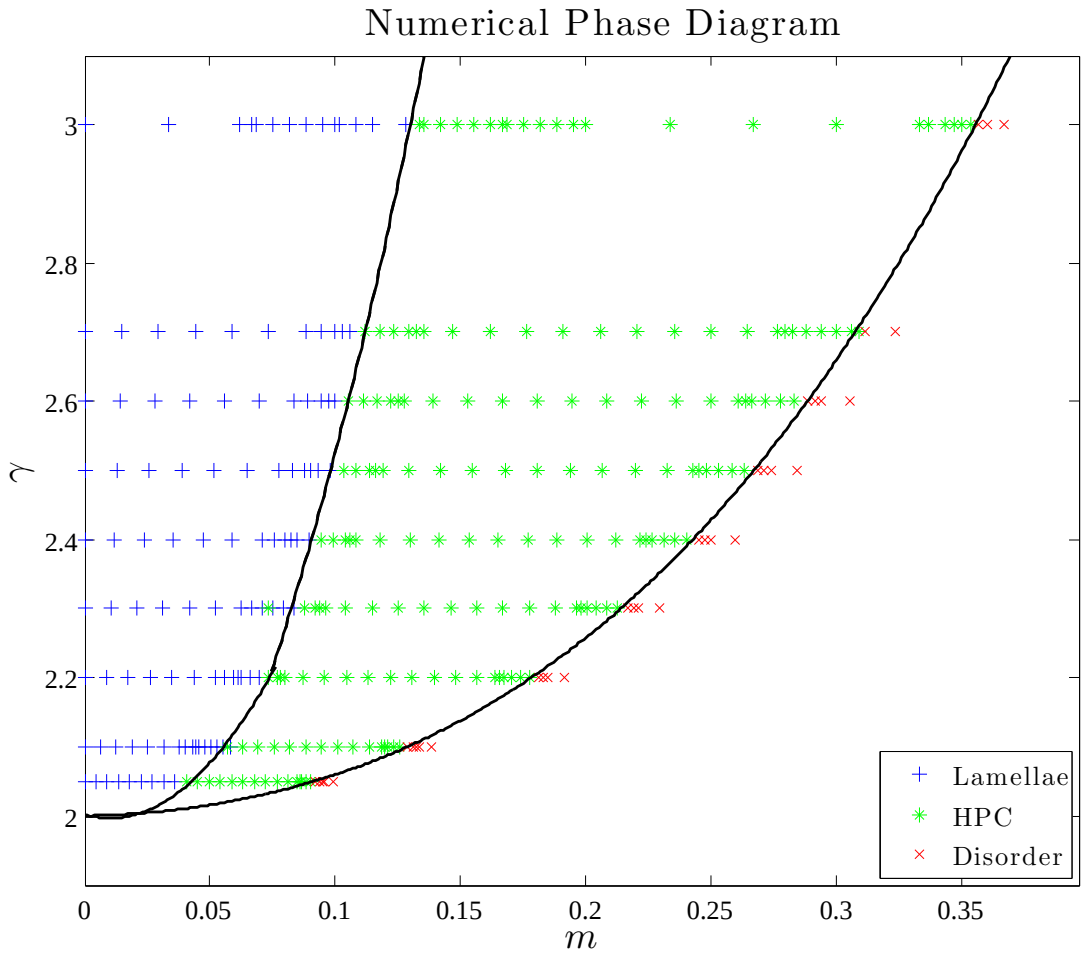

Figure 5.12: Numerical phase diagram for $\gamma \leq 3$. The phase transition between the lamellar and hexagonally packed circular state is approximated by: $\gamma(m) \approx 50m^2 - m + 2$ for $\gamma < 2.2$, and $\gamma(m) \approx 60m^2 - 2m + 1.7$ for $\gamma > 2.2$. The phase transition between the hexagonally packed circular state and the constant state is approximated by $\gamma(m) \approx -93m^4 + 68m^3 - 8m^2 + m + 2$.

Our numerical phase diagram indicates that the transition between the lamellar and hexagonally packed circular states is not sharp. In the diffuse transition region, we observe either one of the two states as the final one, due to their similar energies and random initial conditions. We also note that our numerical phase diagram mostly describes the weak segregation regime, and cannot be presently extended to include the intermediate and strong segregation regimes. The reason for this is the increasing metastable behaviour of simulations in the $\gamma > 3$ region. Already for $\gamma \geq 2.4$, we observe moderately deformed final lamellar states in Figure 5.11. As γ increases these deformities become more severe, as showcased in Figure 5.6, and cannot be categorized without the application of simulated annealing techniques, which may ameliorate the metastability problem.

Chapter 6

Conclusion

In this thesis we described the two-dimensional equilibrium phase behaviour of diblock copolymers via the gradient approach to the Ohta-Kawasaki density functional theory. In particular, we derived the modified Cahn-Hilliard equation as the H^{-1} gradient flow of the nonlocal Cahn-Hilliard energy, and identified two bifurcation parameters, m and γ, as the ones driving the phase behaviour of diblock copolymers. We applied both asymptotic and numerical analysis to the model PDE, with the goal of determining its steady states and their linear and global stability properties. Asymptotic analysis was performed via the center manifold theory, and its results were valid in the order-disorder transition region of the (m, γ) plane, while the numerical results were obtained globally via the pseudospectral implementation of the exponential time differencing Runge-Kutta order 4 scheme. Both methods identified the lamellar, hexagonally packed circular, and constant steady states as the only three attainable two-dimensional morphologies of diblock copolymers. Figures 6.1, 6.2, and 6.3, summarize the asymptotic and numerical linear stability results for these three states. We expect that these results may agree near the order-disorder transition. However, the discrepancy between the asymptotic and numerical linear transition curves for lamellae in Figure 6.1, and hexagonally packed circular state transitioning to lamellae in Figure 6.2, indicate that this is not generally the case. This is not surprising since the true region of validity of asymptotic results is unknown due to their local nature. Furthermore, numerical linear stability results may be affected by a possibly stabilizing influence of the neglected nonlinear term, causing a larger linear stability region for lamellae for example. On the other hand, asymptotic and numerical predictions show a very good agreement in the characterization of the linear stability transition between the hexagonally packed circular state

and the constant state near the order-disorder transition. The best agreement between the results of the two methods is observable in Figure 6.3, where the asymptotic and numerical linear stability transition curves for the constant state are almost indistinguishable.

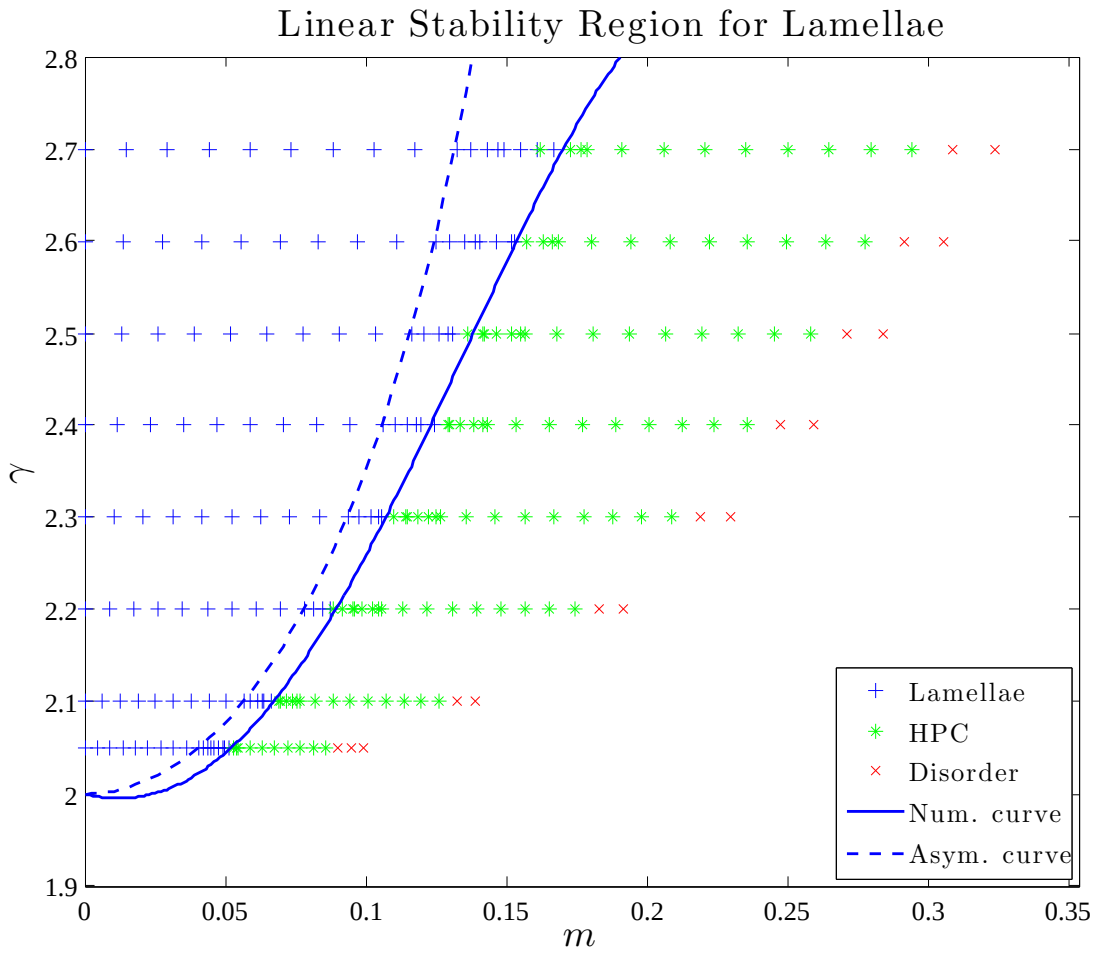

Figure 6.1: Comparison of the asymptotic and numerical linear stability regions for the lamellar steady state.

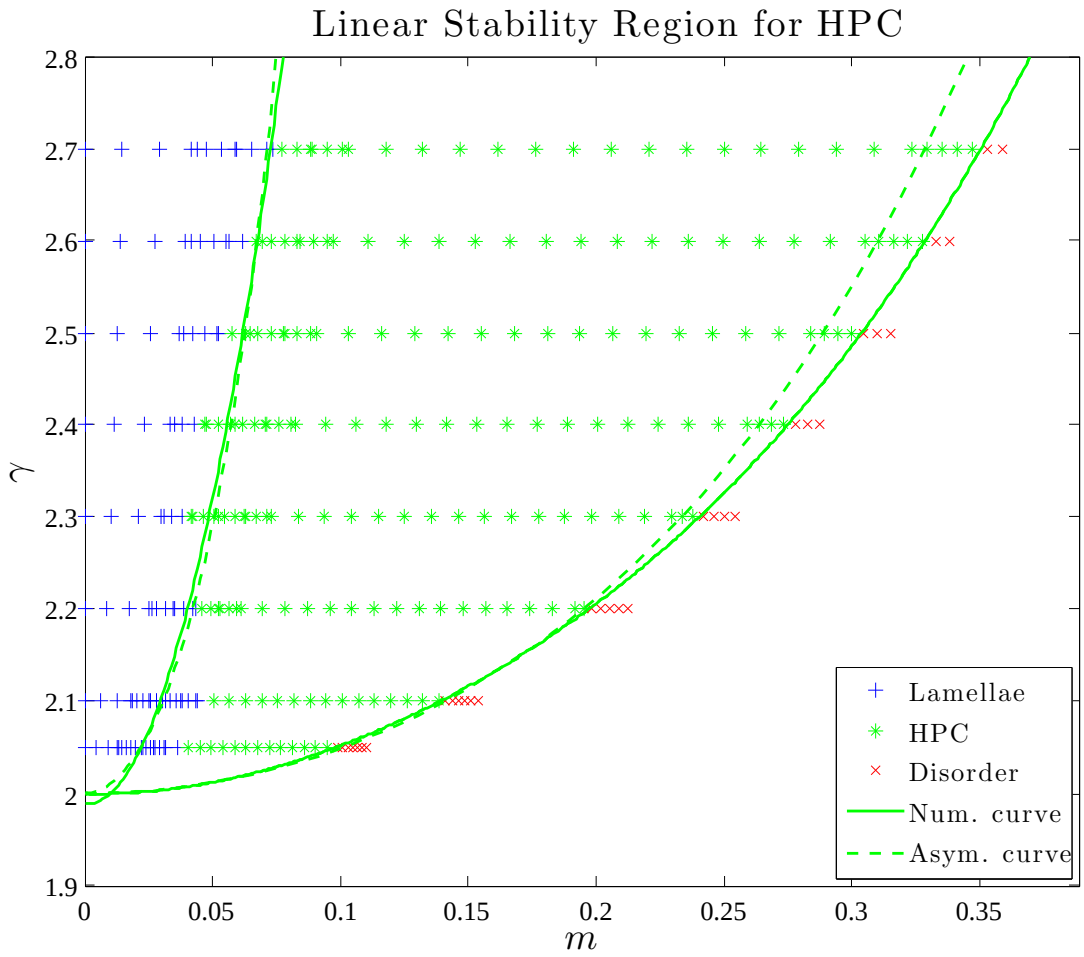

Figure 6.2: Comparison of the asymptotic and numerical linear stability regions for the hexagonally packed circular steady state.

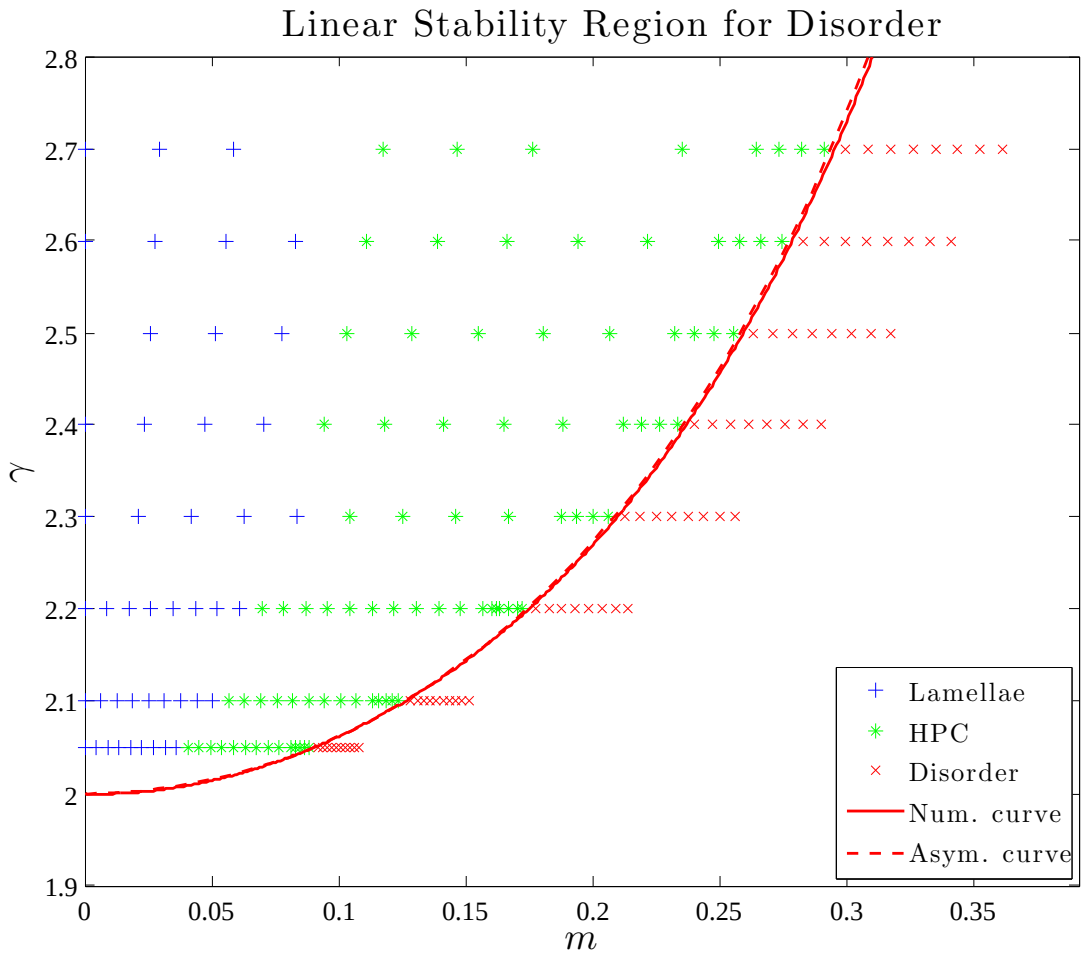

Figure 6.3: Comparison of the asymptotic and numerical linear stability regions for the constant steady state.

Figure 6.4 presents the asymptotic and numerical phase diagrams, which identify regions of global stability of the three steady states. The phase curves predicted by the asymptotic and numerical methods are in good agreement with each other.

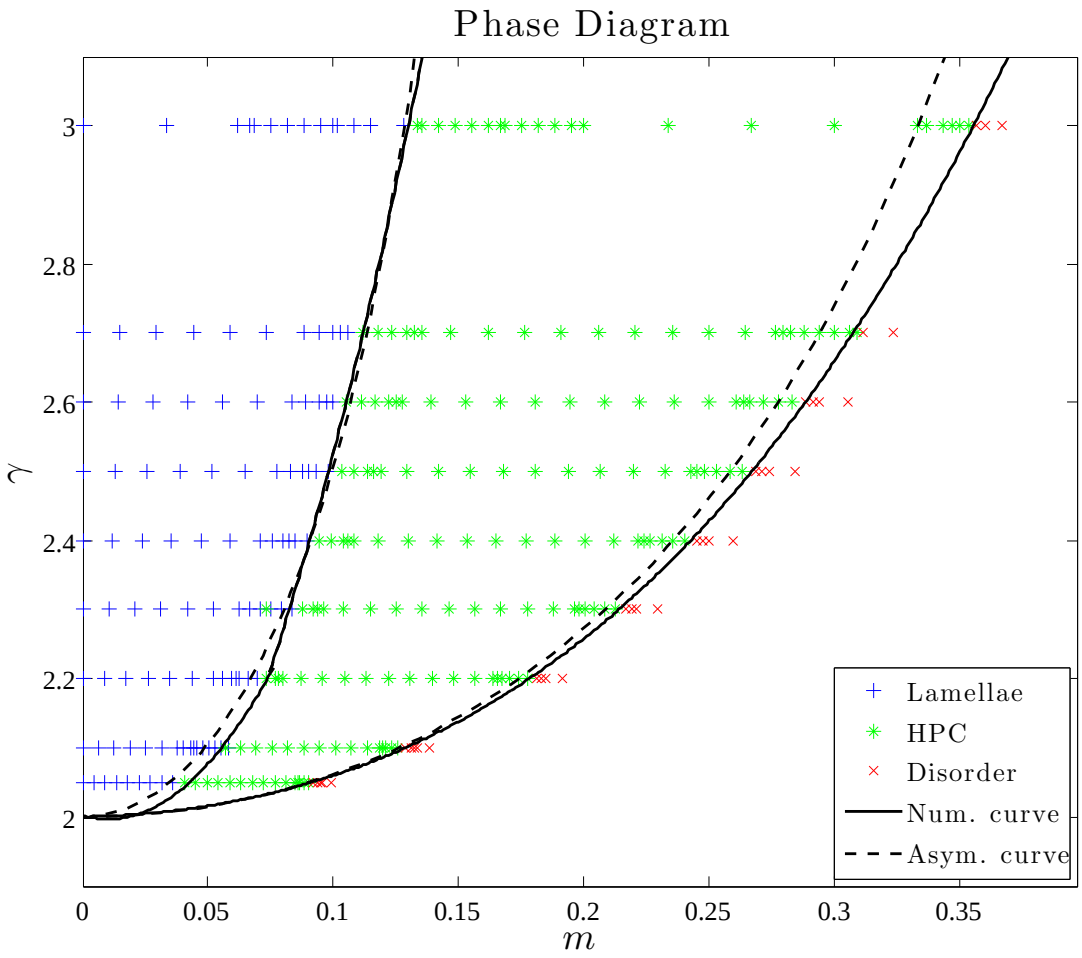

Figure 6.4: Comparison of the asymptotic and numerical phase diagrams, indicating global stability regions of the three steady states.

Ideally, we would have extended the numerical diagram into the $\gamma > 3$ region of the phase plane, but increasing metastable behaviour of the model PDE made the evolution to final steady states unachievable. Simulated annealing techniques, which are used both in experimental synthesis of diblock copolymers and SCFT numerical calculations, may be able to tackle this issue. This is something that can be done in the future, as it is crucial for an

eventual successful derivation of a three-dimensional phase diagram. In three dimensions, the number of steady states increases, and metastability poses an arguably even greater problem, so the two-dimensional test case can be used to find possible systematic ways of ameliorating the metastability problem.

Comparison of our two-dimensional phase diagram with experimental and SCFT diagrams, presented in Figure 1.4, shows qualitative agreement. The hexagonally packed circular steady state is the two-dimensional version of the hexagonally packed cylindrical phase, while the lamellar and constant steady states correspond directly to their three-dimensional versions in the SCFT and experimental diagrams. The phase transition curves between these states in our phase diagram qualitatively match those in Figure 1.4 and converge to the critical point $(m, \gamma) = (0, 2)$, corresponding to $(f_A, \chi N) = (0.5, 10.495)$ in the SCFT diagram.

Results presented in this thesis indicate that the gradient approach to the Ohta-Kawasaki density functional theory leads to qualitatively credible predictions of the equilibrium phase behaviour of diblock copolymers in two dimensions. However, derivation of the three-dimensional phase diagram would be necessary to examine whether the Ohta-Kawasaki theory truly preserves enough of the essential physics at least for qualitative agreement with the experimental and SCFT predictions.

Bibliography

[1] G. Alberti, R. Choksi, and F. Otto. Uniform energy distribution for an isoperimetric problem with long-range interactions. *Journal of the American Mathematical Society*, 22(2):569–605, 2009.

[2] F.S. Bates and G.H. Fredrickson. Block copolymers - designer soft materials. *Physics Today*, 52(2):32–34, 1999.

[3] R. Choksi. Scaling laws in microphase separation of diblock copolymers. *Journal of Nonlinear Science*, 11:223–236, 2001.

[4] R. Choksi, M. Peletier, and J.F. Williams. On the phase diagram for microphase separation of diblock copolymers: an approach via a nonlocal Cahn-Hilliard functional. *SIAM Journal on Applied Mathematics*, 69(6):1712–1738, 2009.

[5] R. Choksi and X. Ren. On a derivation of a density functional theory for microphase separation of diblock copolymers. *Journal of Statistical Physics*, 113:151–176, 2003.

[6] C. Cowan. The Cahn-Hilliard equation as a gradient flow. Master's thesis, Simon Fraser University, 2005.

[7] S.M. Cox and P.C. Matthews. Exponential time differencing for stiff systems. *Journal of Computational Physics*, 176:430–455, 2002.

[8] D. Eyre. An unconditionally stable one-step scheme for gradient systems, 1998.

[9] P. Fife. Models for phase separation and their mathematics. *Electronic Journal of Differential Equations*, 2000(48):1–26, 2000.

[10] B. Fornberg. *A Practical Guide to Pseudospectral Methods*. Cambridge University Press, 1996.

[11] G. Fredrickson and E. Helfand. Fluctuation effects in the theory of microphase separation in block copolymers. *Journal of Chemical Physics*, 87(1):697–706, 1987.

[12] G.H. Fredrickson. *The Equilibrium Theory of Inhomogeneous Polymers*. Oxford Science Publications, Clarendon Press, 2006.

[13] D.A. Hajduk, H. Takenouchi, M.A. Hillmyer, and F.S. Bates. Stability of the perforated layer (PL) phase in diblock copolymer melts. *Macromolecules*, 30:3788–3795, 1997.

[14] I. Hamley. *The Physics of Block Copolymers.* Oxford University Press, 1998.

[15] D.A. Hoffman. Website: http://www.msri.org/about/sgp/jim/geom/index.html. The Scientific Graphics Project, 1998.

[16] M.H. Holmes. *Introduction to Perturbation Methods.* Springer-Verlag, 1995.

[17] A. Kassam and L.N. Trefethen. Fourth-order time-stepping for stiff PDEs. *SIAM Journal on Scientific Computing*, 26(4):1214–1233, 2005.

[18] A.K. Khandpur, S. Foerster, F.S. Bates, I.W. Hamley, A.J. Ryan, W. Bras, K. Almdal, and K. Mortensen. Polyisoprene-polystyrene diblock copolymer phase diagram near the order-disorder transition. *Macromolecules*, 28:8796–8806, 1995.

[19] L. Leibler. Fluctuation effects in the theory of microphase separation in block copolymers. *Macromolecules*, 13:1602–1617, 1980.

[20] M.W. Matsen and F.S. Bates. Unifying weak- and strong-segregation block copolymer theories. *Macromolecules*, 29:1091–1098, 1996.

[21] M.W. Matsen and M. Schick. Stable and unstable phases of a diblock copolymer melt. *Physics Review Letters*, 72:2660–2663, 1994.

[22] C.B. Muratov. Theory of domain patterns in systems with long-range interactions of Coulomb type. *Physical Rewiev E*, 66(6):066108(1–25), 2002.

[23] T. Ohta and K. Kawasaki. Equilibrium morphology of block copolymer melts. *Macromolecules*, 19:2621–2632, 1986.

[24] L.A. Peletier and J.F. Williams. Some canonical bifurcations in the Swift-Hohenberg equation. *SIAM Journal on Applied Dynamical Systems*, 6(1):208–235, 2005.

[25] X. Ren and J. Wei. Stability of spot and ring solutions of the diblock copolymer equation. *Journal of Mathematical Physics*, 45(11):4106–4133, 2004.

[26] X. Ren and J. Wei. Wriggled lamellar solutions and their stability in the diblock copolymer problem. *SIAM Journal on Mathematical Analysis*, 37(2):455–489, 2005.

[27] X. Ren and J. Wei. Droplet solutions in the diblock copolymer problem with skewed monomer composition. *Calculus of Variations and Partial Differential Equations*, 25(3):333–359, 2006.

[28] M.F. Schulz, A.K. Khandpur, and F.S. Bates. Phase behavior of polystyrene-poly(2-vinylpyridine) diblock copolymers. *Macromolecules*, 29:2857–2867, 1996.

[29] X. Sun and M.J. Ward. Dynamics and coarsening of interfaces for the viscous Cahn-Hilliard equation in one spatial dimension. *Studies in Applied Mathematics*, 105(3):203–234, 2000.

[30] T. Teramoto and Y. Nishiura. Double gyroid morphology in a gradient system with nonlocal effects. *Journal of the Physical Society of Japan*, 71(7):1611–1614, 2002.

[31] E. Thomas, D.M. Anderson, C.S. Henkee, and D. Hoffman. Periodic area-minimizing surfaces in block copolymers. *Nature*, 334:598–601, 1988.

[32] L.N. Trefethen. *Spectral Methods in Matlab*. SIAM, 2000.